universität wien

MASTERARBEIT / MASTER'S THESIS

Titel der Masterarbeit / Title of the Master's Thesis

Exploiting Spin Orbit Torque for magnetic field sensing / Concepts of multiturn sensors

verfasst von / submitted by

Marcel Gasser, BSc

angestrebter akademischer Grad / in partial fulfilment of the requirements for the degree of

Master of Science (MSc)

Wien, 2023 / Vienna, 2023

Studienkennzahl lt. Studienblatt / degree programme code as it appears on the student record sheet:	UA 066 876
Studienrichtung lt. Studienblatt / degree programme as it appears on the student record sheet:	Masterstudium Physik UG2002
Betreut von / Supervisor:	Univ.-Prof. Dipl.-Ing. Dr.techn. Dieter Süss, Privatdoz.

Acknowledgement

I want to thank the entire group *Physics of Functional Materials* for the support when setting up and performing magnetic simulations. It is of ultimate advantage to do the work in the group, where the simulations codes are developed and where the people are experts in performing micromagnetic simulations. Especially, I want to thank my supervisor Dieter Süss for supporting me and always giving me input for new concepts. Even though many new ideas did not work out well, it is interesting to investigate recent and partly fresh sensor designs. Moreover, Sabri Koraltan is another person to be mentioned, since he is an expert in setting up simulations and he supported me many times with code parts. It was very helpful to have the mastermind of one of the used simulation codes in the group. Joshua Salazar-Mejía, Amil Ducevic and Peter Flauger are other group members, who were part of the ambient scientific project. However, my thanks go also to the rest of the group, especially to my office neighbors Markus Gattringer, Robert Kraft and David Zehner and to the numerical simulation expert Claas Abert.

In addition, I want to thank the people at the industrial partner Infineon Technologies Austria AG. The thesis emerges from a scientific project with this partner and many interesting experimental results encouraged examinations performed in this thesis. Armin Satz and Johannes Güttinger were the managing people at Infineon for this project. Particularly, I want to thank Sebastian Zeilinger for his tireless efforts at doing experimental investigations about Spin Orbit Torque sensor concepts and his support at examining physical backgrounds. It is beneficial to have experimental data available to back up simulation data. Even though she entered the project at the end of my work for the thesis, my thanks also go to Verena Wutte, who often looked at my results and judged them from an outside point of view.

Abstract

Magnetic field sensing plays a crucial role in our everyday life. Whether for safety aims in the automotive sector, for electronical devices used on a daily basis or for industrial purposes, a huge variety of potential applications exists for magnetic field sensors. In all these application fields, a high sensing accuracy and a good response to small field changes in the presence of realistic disturbances is of major importance. To sense the strength of magnetic fields, the simple Hall sensor exploiting the Hall effect is the most widely used sensor type. This is mostly due to its simplicity, both in the theoretical description and in the practical application, and due to its high sensor accuracy. However, the Hall sensor based on the typical Hall effect with the Lorentz force controlling it is not always applicable, especially for the measurement of small magnetic fields. Fortunately, there are many different Hall effects with more complicated physical backgrounds, that enable magnetic field sensing of small fields. A very promising approach is to take the spins of electrons into account. Spintronics has a large variety of potential applications and also in the present case, the Spin Hall effect might help in the improvement of magnetic field sensors. This effect is one of the main contributors to the recently described Spin Orbit Torque (SOT) effect.

Another interesting application of a sensor in a magnetic field is the multiturn counter. The aim of such a sensor device is to count the number of rotations of a magnetic field without the help of current enabling the field sensing at any time. Hence, the sensor is initialized and afterwards, no power supply takes place when counting the rotations. When determining the final number of rotations, power must be supplied for readout. The application fields for such a sensor device are very diverse, ranging from industrial realizations to safety facilities. Actually, a multiturn counter is applicable where a robust positioning with a finite number of positions is needed.

This thesis is divided into two parts. The first part focuses on the inspection of the SOT effect as potential magnetic field sensing principle. Some sensor concepts are discussed and examined in terms of accuracy and resilience against disturbing fields. Since the topic is relatively new and there is ongoing research on this topic, the present report aims to give basic insights into some concepts under examination.

The second part of the thesis is dedicated to concepts of multiturn sensors. Some concepts are working with moving magnetic domain walls in certain soft magnetic structures. Others are working by moving magnetic bubbles due to a certain guiding structure. The later principle is already known from bubble memory realized in the 1970s. (Nielsen, 1979) (Gowland, 1977) However, applying this concept to implement a multiturn sensor with thin layers in the nanometer regime requires further investigation, where this report should only encourage examinations beyond the outcome presented here.

Kurzfassung

Magnetfeldsensoren spielen eine immer größere Rolle in den verschiedensten alltäglichen Anwendungsbereichen. Ob für Sicherheitsanwendungen im Mobilitätssektor, für Sensoren in mobilen Geräten oder für Positionsmessungen in der Industrie, das Potenzial von solchen Sensoren zur Detektierung der Magnetfeldstärke ist immens, besonders im Hinblick auf die jüngsten technologischen Fortschritte. Dabei dominieren Hall-Sensoren dieses Segment. Typische Hall-Sensoren basieren auf dem "normalen" Hall-Effekt, welcher durch die Lorentzkraft zustande kommt. Dieser Effekt bietet eine einfache Möglichkeit, um Magnetfeldstärken zu messen, wobei die Sensoren genau und verlässlich detektieren. Wenn jedoch sehr kleine Magnetfelder gemessen werden sollen, müssen andere Detektierungsmethoden gefunden werden. Praktischerweise gibt es weitere Hall-Effektarten, welche auf anderen physikalischen Grundlagen basieren und komplexere Realisierungen von Hall-Sensoren ermöglichen. Wenn die Spins von Elektronen in die Betrachtung miteinbezogen werden, so gibt es den Spin-Hall-Effekt, welcher maßgeblich zum kürzlich entdeckten Spin-Bahn-Drehmoment-Effekt (Spin Orbit Torque (SOT)) beiträgt. Dieser tritt auf, wenn ein Schwermetall wie Platin oder Tantal und ein ferromagnetisches Material übereinandergestapelt werden und Strom durch das Schwermetall fließt. Das Drehmoment auf die Magnetisierung im Ferromagneten kann zur Magnetfelddetektierung genutzt werden, wobei in dieser Masterarbeit verschiedene Realisierungskonzepte untersucht werden sollen. Die Magnetisierung des Ferromagneten wird dabei durch einen geeigneten Magnetowiderstand bestimmt.

Runde oder elliptische Sensorelemente bestehend aus einer dünnen Schwermetall-Ferromagnet-Stapelung bieten eine sehr einfache Struktur. Falls die Anfangsmagnetisierung aus der Ebene der Stapelung zeigt, handelt es sich um einen transversalen (out-of-plane) Sensor, der eine planare Magnetisierungskomponente detektieren kann. Dieser funktioniert trotz seiner Einfachheit überraschend zuverlässig. Falls die Anfangsmagnetisierung planar ausgerichtet ist, handelt es sich um einen planaren (in-plane) Sensor, der die auf die Stapelebene normal stehende Magnetisierungskomponente messen kann. Hier ergibt sich das Problem, dass sich bei vielen Störfeldausrichtungen ein Nullpunktversatz der Signalkurve ergibt. Dieser kann durch Kombination verschiedener Sensorelement kompensiert werden.

Durch eine geschickte Kombination solcher planaren Sensorelement in einer Wheatstone-Brücke ergibt sich ein Sensorkonzept, welches durch eine Forschungsgruppe um Yanjun Xu (Xu et al., 2018) präsentiert wurde. Dieser weist laut dem Forschungsbericht ausgezeichnete Eigenschaften auf, wie z.B. eine sehr hohe Detektierfähigkeit, vernachlässigbaren Nullpunktversatz und vernachlässigbare Hysterese. Allerdings muss betont werden, dass der Sensor nur zur Messung von sehr kleinen Feldstärken im Bereich bis 10 μT geeignet ist. Für größere Feldstärken ergeben sich gravierende Probleme, welche kaum behoben

werden können. Falls die Feldstärken auf bis zu 10 μT beschränkt sind, funktioniert dieses Sensorkonzept jedoch überraschend gut. Auch als Rotations- und Vibrationssensor bietet sich dieser Aufbau an, wobei die gegebene Feldstärkenschwelle auch hier zu beachten ist. Das setzt natürlich hohe Anforderungen an die Abschirmung störender Magnetfelder von außen voraus, da schon das Erdmagnetfeld einige μT ausmacht.

Der Spin-Bahn-Drehmoment-Effekt kann auch in einer typischen Hall-Kreuz-Geometrie zur Detektierung verwendet werden. Dabei bricht das Kreuz in einen Multidomänenzustand auf, wobei die Domänen eine Magnetisierung aus der Kreuzebene aufweisen. Durch den Stromfluss in einem Arm des Kreuzes wird die Magnetisierung abhängig vom wirkenden Magnetfeld beeinflusst, sodass eine Domäne bevorzugt wird und bei genügend großem Feld der gesamte Arm nur noch in eine Richtung magnetisiert ist. Dies ermöglicht die Feldstärkenbestimmung in Richtung des Stromflusses. Durch einen geschickten Schaltungsaufbau, bei dem beide Arme abwechselnd mit dem relevanten Strom angesteuert werden können, und durch Kombination der Signale kann ein dreidimensionaler Feldstärkensensor realisiert werden. Dieser weist eine gute Signalkurve mit einer hohen Empfindlichkeit auf, wobei der lineare Bereich zur Feldstärkenmessung recht klein ist.

Magnetische Rotationszähler haben ebenfalls verschiedene Anwendungsgebiete, ob im Automobilsektor oder bei der Positionsmessung in der Industrie. Dabei setzen die meisten Realisierungen eine ständige Stromzufuhr voraus. Falls es während der Messung jedoch zu einem Stromausfall kommt, kann die gemessene Rotationsanzahl bei neuerlicher Stromzufuhr nicht mehr wiedergewonnen werden, wodurch eine neuerliche Initialisierung und eine neuerliche Messung erforderlich sind. Ziel eines "unvergänglichen" Rotationszählers ist, dass dieser während des Zählvorgangs nicht auf eine ständige Stromzufuhr angewiesen ist, sondern nur während der Initialisierung und dem Auslesen der Rotationsanzahl. Dies hätte in sensiblen Anwendungsfällen im Automobil- und Industriesektor einige Vorteile, wobei die Realisierung entsprechender Konzepte einige Schwierigkeiten mit sich bringt.

Ein mögliches Konzept wäre die Bewegung einer magnetischen Domänenwand in einem weichmagnetischen Material, welche durch ein rotierendes Feld getrieben wird. Durch eine geeignete Geometrie können auf Basis der Position der Domänenwand mehrere Rotationen gezählt werden. Neben der intuitiven Spiralform wird in der Forschungsgruppe um Roland Mattheis (Mattheis et al., 2012) eine Höckerstruktur vorgeschlagen, wobei die Höcker die Bewegung der Domänenwände durch die Magnetfeldrotation verlangsamen. Diese Realisierung erweist sich als sehr zuverlässig und kann durch Aneinanderreihung vieler Höcker zur Zählung einiger Rotationen verwendet werden. Allerdings setzt dieses Konzept eine dünne Struktur voraus, welche in größerem Ausmaß industriell schwer zu produzieren ist.

Ein weiteres Konzept basiert auf dem Magnetblasenspeicher, welcher in den 1970ern und 1980ern intensiv untersucht wurde. Dabei wurden Skyrmionen in einer geeigneten Schicht durch ein rotierendes magnetisches Feld mit Hilfe einer weichmagnetischen Führungsstruktur an bestimmte Positionen bewegt. Skyrmion oder kein Skyrmion entsprach dabei den Bits 0 oder 1, wodurch Datenspeicherung ermöglicht wurde. Anstatt zur Datenspeicherung kann dieses Prinzip verwendet werden, um ein Skyrmion durch ein

rotierendes Feld zu bewegen und über die Position eben dieses die Anzahl an Rotationen zu messen. Obwohl Magnetblasenspeicher in der Vergangenheit realisiert wurden und die Bewegung der Skyrmionen entsprechend zuverlässig funktionerte, ergeben sich bei den Simulationen entsprechender Rotationszähler überraschend Probleme. Im Zuge dieser Arbeit werden einige Materialkombinationen für dieses Konzept untersucht, die in der Vergangenheit realisiert wurden, jedoch ermöglicht keine dieser Konstellationen eine Rotationszählung, da sich die Skyrmionen nicht durch die Führungsstruktur bewegen lassen, sondern nur eine unkontrollierte Beeinflussung zu beobachten ist. Dies ist insofern überraschend, als dass sich die Skyrmionen in Simulationen leichter bewegen lassen sollten als im Experiment, bei dem störende Einflüsse die Bewegung hemmen können. Aufgrund der praktischen Realisierung von Magnetblasenspeichern und der Kontrollierbarkeit der Skyrmionenbewegung in diesem Aufbau ist jedoch zu erwarten, dass dieses Konzept als Rotationszähler verwendet werden kann.

Abschließend kann gesagt werden, dass der Spin-Bahn-Drehmoment-Effekt viel Potential für neue Sensorkonzepte zur Detektierung von Magnetfeldern birgt. In der Arbeit wurden nur sehr einfache Realisierungen besprochen, welche in komplexeren Konstellationen verlässliche Sensoren ermöglichen können. Für magnetische Rotationszähler scheint der Höckersensor geeignet, wobei die Produktion im großen Maße ein Problem darstellt, welches durch Anpassung der Geometrie möglicherweise umgangen werden kann. Die Rotationszählung mit Skyrmionen wirkt in Simulationen unzuverlässig, sollte jedoch auch realisierbar sein. Alle Untersuchungen in dieser Arbeit sollen einen groben Überblick über Rotationszähler und Magnetfeldsensoren basierend auf dem Spin-Bahn-Drehmoment-Effekt liefern und weitere Forschungsbemühungen in diese Richtungen anregen.

Contents

Abbreviations

AC Alternating Current

AHE Anomalous Hall Effect

AMR Anisotropic Magnetoresistance

DC Direct Current

DW Domain Wall

DLT Dampinglike Torque

FD Finite Difference

FE Finite Element

FLT Fieldlike Torque

GMR Giant Magnetoresistance

GPU Graphics Processing Unit

LLG Landau-Lifshitz-Gilbert

LLGS Landau-Lifshitz-Gilbert-Slonczewski

MBM Magnetic Bubble Memory

MRAM Magnetoresistive Random Access Memory

MR Magnetoresistance

PHE Planar Hall Effect

SHE Spin Hall Effect

SMR Spin Hall Magnetoresistance

SOT Spin Orbit Torque

STT Spin Transfer Torque

TMR Tunneling Magnetoresistance

Chapter 1

Introduction

1.1 Landau-Lifshitz-Gilbert equation

The Landau-Lifshitz equation was first introduced by Lew Dawidowitsch Landau and Jewgeni Michailowitsch Lifschiz (Landau & Lifshitz, 1992) and an alternative formulation was presented by Thomas L. Gilbert. (Gilbert, 2004) The well-known Landau-Lifshitz-Gilbert (LLG) equation describes the magnetization dynamics in a ferromagnetic material. The implicit form is given by the equation (1.1), which can be easily transformed into the explicit form (1.2) by applying simple vector algebra and basic identities. The LLG equation characterizes the time evolution of the magnetization unit vector $\mathbf{m}$, which in contrast to the actual magnetization vector $\mathbf{M}$ is normalized with respect to the spontaneous magnetization M_s, that is the saturation magnetization in the case of zero temperature: $\mathbf{M} = M_s\mathbf{m}$. Since magnetic simulations assume zero temperature, M_s is referred to as saturation magnetization throughout the following thesis. $\gamma = \mu_0\gamma_e \approx 2.2128 \cdot 10^5$ m/As with μ_0 being the vacuum permeability and γ_e being the gyromagnetic ratio of an electron is the reduced gyromagnetic ratio and α is the Gilbert damping parameter. (Abert, 2019)

$$\frac{\partial \mathbf{m}}{\partial t} = -\gamma \mathbf{m} \times \mathbf{H}_{\mathbf{eff}} + \alpha \mathbf{m} \times \frac{\partial \mathbf{m}}{\partial t} \tag{1.1}$$

$$\frac{\partial \mathbf{m}}{\partial t} = -\frac{\gamma}{1+\alpha^2}\mathbf{m} \times \mathbf{H}_{\mathbf{eff}} - \frac{\alpha\gamma}{1+\alpha^2}\mathbf{m} \times (\mathbf{m} \times \mathbf{H}_{\mathbf{eff}}) \tag{1.2}$$

The effective field $\mathbf{H}_{\mathbf{eff}}$ combines all contributions of energy terms, that tend to be minimized during the dynamical evolution of the magnetic system. In the following sections the different energy terms according to (Abert, 2019) are described. The theoretical model, which these energy term formulations are based on, is the micromagnetic model described in Section 2.2. These energy terms translate into $\mathbf{H}_{\mathbf{eff}}$ by the relation (1.3), where $\delta E/\delta \mathbf{m}$ is the functional derivative of the energy E with respect to the magnetic moment $\mathbf{m}$. Note that the functional derivative with respect to a vector field means in this case the functional derivative for each component of the vector field, which gives the corresponding component of the resulting vector field.

$$\mathbf{H}_{\mathbf{eff}} = -\frac{1}{\mu_0 M_s}\frac{\delta E}{\delta \mathbf{m}} \tag{1.3}$$

1.1.1 Zeeman energy

The energy contribution of the external magnetic field to the ferromagnetic system is called Zeeman energy. The energy term is given by (1.4), which is indeed the equation leading to relation (1.3), since without any other energy contributions the effective field has to be equal to the external field $\mathbf{H_{zee}}$. The other energy contributions are therefore considered to act as additional external fields, which add up to the effective field $\mathbf{H_{eff}}$. The integration is performed over the magnetic region Ω_m.

$$E_{\text{zee}} = -\mu_0 \int_{\Omega_m} M_s \mathbf{m} \cdot \mathbf{H}_{\text{zee}} \mathrm{d}\mathbf{x} \tag{1.4}$$

1.1.2 Exchange energy

The exchange energy integrates the exchange interaction between the spins into the calculation. This interaction is described by the Heisenberg model. The exchange energy of two unit spins $\mathbf{s_{i/j}}$ is given in (1.5), where J is the coupling constant or exchange integral.

$$E_{ij} = -J \mathbf{s_i} \cdot \mathbf{s_j} \tag{1.5}$$

Embedding this model for the exchange energy into the framework of micromagnetics, performing some simplifications and assuming cubic and isotropic lattice structures leads to the expression for the total exchange energy (1.6) with A being the exchange constant and $(\nabla \mathbf{m})^2 = \sum_{i,j} (\partial m_i / \partial x_j)^2$ being like the Frobenius inner product.

$$E_{\text{ex}} = \int_{\Omega_m} A (\nabla \mathbf{m})^2 \mathrm{d}\mathbf{x} \tag{1.6}$$

1.1.3 Demagnetization energy

The demagnetization energy or stray-field energy takes into account, that magnetic systems tend to demagnetize themselves macroscopically. At this point the mathematical derivation of the demagnetization energy is omitted (for further details the reader is referred to (Abert, 2019)). The demagnetization field $\mathbf{H_{dem}}$, which depends on the position $\mathbf{x}$, is given by the expression (1.7), where $\mathbf{M} = M_s \mathbf{m}$ is the magnetization and $\tilde{\mathbf{N}}$ is the demagnetization tensor given by (1.8).

$$\mathbf{H_{dem}}(\mathbf{x}) = \int_{\Omega_m} \tilde{\mathbf{N}}(\mathbf{x} - \mathbf{x}') \mathbf{M}(\mathbf{x}') \mathrm{d}\mathbf{x}' \tag{1.7}$$

$$\tilde{\mathbf{N}}(\mathbf{x} - \mathbf{x}') = -\frac{1}{4\pi} \nabla \nabla' \frac{1}{|\mathbf{x} - \mathbf{x}'|} \tag{1.8}$$

The resulting energy contribution can be calculated by using the relation (1.9), where the integral is performed over the magnetic region Ω_m. The factor $1/2$ results from the quadratic dependency on $\mathbf{M}$. (Abert, 2019)

$$E_{\text{dem}} = -\frac{\mu_0}{2} \int_{\Omega_m} \mathbf{M} \cdot \mathbf{H_{dem}} \mathrm{d}\mathbf{x} \tag{1.9}$$

1.1.4 Uniaxial anisotropy energy

The anisotropy energy takes into account, that a magnetization alignment parallel to certain axes is favored. These axes are called easy axes. The reasons for this energy are either anisotropic crystal structures or lattice deformations at material interfaces. If there is only one easy axis present in a sample, the situation is called uniaxial anisotropy. The energy term of this anistropy is given in equation (1.10), where K_{u} is the uniaxial anistropy constant and $\mathbf{e_u}$ is the unit vector along the easy axis.

$$E_{\mathsf{aniso}} = -\int_{\Omega_m} [K_{\mathrm{u}}(\mathbf{m}\cdot\mathbf{e_u})^2 + \mathcal{O}(\mathbf{m}^4)])\mathrm{d}\mathbf{x} \tag{1.10}$$

A cubic lattice structure induces three easy axes pairwise orthogonal to each other. However, this cubic anisotropy will not be used in this thesis.

1.2 Spin Orbit Torque (SOT)

Besides of being charged particles, electrons also exhibit a spin. If there are no ferromagnetic samples present in a current circuit, the spins of electrons do not play a role there. Introducing ferromagnetic components in current circuits leads to some interesting effects. A very prominent example is the Spin Transfer Torque (STT), where the electrons flowing through a ferromagnetic layer become partially spin-polarized and can influence the magnetizations of other ferromagnetic components by exerting a torque on the magnetization vectors, hence it is called Spin Transfer Torque. (Ralph & Stiles, 2008)

The Spin Orbit Torque (SOT) is a phenomenologically described effect, which dates back to the early 2010s. A charge current flowing through a paramagnetic layer (typically a heavy metal like platinum or tantalum) induces a spin current or a spin accumulation normal to the charge current flow. This phenomenon can be explained by the Spin Hall Effect (SHE), which describes the spin current generated due to a charge current. This effect is illustrated in Figure 1.1(a), where a charge current J_e leads to a spin current J_s with σ being the polarization vector according to which the spins of the electrons (e) align. Things get more interesting, if a ferromagnetic (FM) layer is added adjacent to the heavy metal layer, because the spin flow can affect the magnetization $(\mathbf{M})$ in the ferromagnetic layer. Hence a torque is applied due to the charge current in the adjacent paramagnetic layer. The theory underlying this phenomenological SOT is not fully understood, but it is assumed that both the SHE as a bulk interaction and the Rashba-Edelstein effect as an interfacial interaction contribute to the SOT. (Nguyen & Pai, 2021)

There are two SOT effects, which have to be differentiated: the dampinglike and the fieldlike effect. They contribute to the SOT in the form of a Dampinglike Torque (DLT) and a Fieldlike Torque (FLT). These torques can both be induced by the SHE and by the Rashba-Edelstein effect, which makes the exact theoretical description burdensome. (Zhu & Zhao, 2020) The torque terms add up to the other contributing terms in the LLG equation (1.1), where the equations for DLT and FLT according to Slonczewski are given by (1.11) and (1.12), respectively. (Abert, 2019)

$$\mathsf{DLT} = \eta_{\mathsf{damp}}\frac{j_e\gamma\hbar}{2et\mu_0 M_s}\mathbf{m}\times(\mathbf{m}\times\mathbf{p}) \tag{1.11}$$

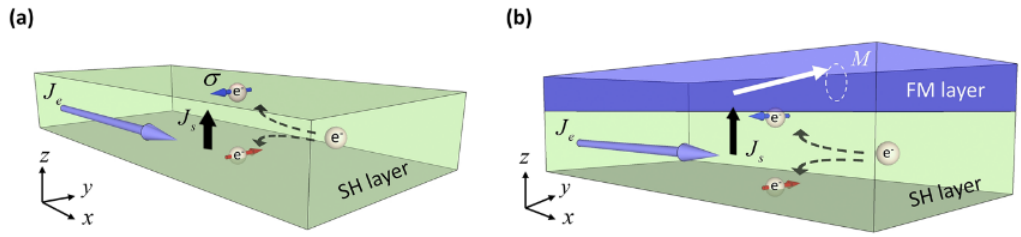

Figure 1.1: Illustration of the SHE in (a) a Spin-Hall (SH) layer (typically a heavy-metal layer) and (b) a heterostructure of a SH layer and a ferromagnetic (FM) layer. (taken from Nguyen & Pai, 2021, p. 2).

$$\text{FLT} = \eta_{\text{field}} \frac{j_e \gamma \hbar}{2et\mu_0 M_s} \mathbf{m} \times \mathbf{p} \tag{1.12}$$

The parameters η_{damp} and η_{field} characterize the strengths of the torques and are functions of the angle between the magnetization unit vector $\mathbf{m}$ and the polarization vector $\mathbf{p}$. j_e, t and M_s are the SOT current density, the thickness of the free layer and the saturation magnetization, respectively. The constants γ, $\hbar$, e and μ_0 are the reduced gyromagnetic ratio, the reduced Planck constant, the charge of an electron and the vacuum permeability. The torque terms can be expressed as effective field contribution. The incorporation of the torque contribution into the LLG equation leads to the Landau-Lifshitz-Gilbert-Slonczewski (LLGS) equation, which in the explicit form can be written as (1.13). (Abert, 2019) (Makarov, 2014) (Zhu & Zhao, 2020)

$$\begin{aligned} \frac{\partial \mathbf{m}}{\partial t} = &- \frac{\gamma}{1+\alpha^2} \mathbf{m} \times \left[\mathbf{H}_{\mathbf{eff}} + \frac{j_e \hbar}{2et\mu_0 M_s} (\alpha \eta_{\text{damp}} - \eta_{\text{field}}) \mathbf{p} \right] \\ &- \frac{\alpha\gamma}{1+\alpha^2} \mathbf{m} \times \left(\mathbf{m} \times \left[\mathbf{H}_{\mathbf{eff}} + \frac{j_e \hbar}{2et\mu_0 M_s} \left(-\frac{1}{\alpha} \eta_{\text{damp}} - \eta_{\text{field}} \right) \mathbf{p} \right] \right) \end{aligned} \tag{1.13}$$

1.3 Magnetoresistances

Magnetoresistance (MR) describes the influence of a magnetic field on the resistivity of a material. The MR-ratio is the amplitude of the effect and is given as $\Delta\rho/\rho_0$, where $\Delta\rho$ is the change in resistivity due to a magnetic field compared to a resistivity ρ_0 at zero field. There exist different effects in this phenomenon group. One of the first observed MR-effects was the Anisotropic Magnetoresistance (AMR)-effect, which appears in ferromagnetic materials. The MR-ratio amounts to 2% and the resistivity change depends on the direction of the magnetic field compared to the current flow, therefore being anistropic. The underlying physical mechanism is the Spin Orbit Coupling, which causes a deformation of the electron clouds around each nucleus, hence leading to a change in the scattering probability depending on whether the deformation is parallel or normal to the current direction. (Nickel, 1995)

The Giant Magnetoresistance (GMR)-effect was first observed in 1988 in the paper (Baibich et al., 1988) and appears, if two thin magnetic layers are separated by a non-magnetic conducting layer. Depending on how the magnetization configurations are oriented, the resistivity changes along the stack and the magnetic field contributes to

this configuration. The MR-ratio is up to 50%. (Nickel, 1995) Especially if one layer has a fixed magnetization configuration realized with a hard magnetic material, this effect can be exploited to determine the magnetization direction of the other ferromagnetic layer. The Tunneling Magnetoresistance (TMR)-effect is similar to the GMR-effect concerning the stack, but instead of separating the magnetic layers by a conducting layer, a non-magnetic insulator is used. This effect is based on spin-dependent electron tunneling through the insulator. Electrons tunnel more easily, if the magnetization orientation is equal in both magnetic layers, thus reducing the resistivity. This enables much higher MR-ratios of some hundreds of percent with a theoretically possible value of 1000% with crystalline magnesium oxide as tunnel barrier. (Yuasa, 2008) Magnetic tunnel junctions exploiting the TMR-effect are widely used to sense magnetization configurations.

The Spin Hall Magnetoresistance (SMR)-effect appears in bilayers of a ferromagnetic insulator (for example yttrium iron garnet) and a metal. Due to the SHE and current flowing through the metal, a torque is transferred to the ferromagnetic layer depending on the current direction and the magnetization configuration in the magnet, causing a resistance dependency on the magnetization configuration. (Chen et al., 2016)

Chapter 2

Methods

This thesis is based on theoretical considerations and magnetic simulations. Even though the assumptions taken in the different simulation models seem to be restrictive and far away from real settings, they are capable of predicting the behaviour of magnetic systems quite well within the limits of their applicability. Simulation and experiment will always exhibit some sort of discrepancy, since the simulation assumes zero temperature and large numbers of magnetic moments are combined to a few magnetic moments to reduce computational effort. Moreover, it is crucial to take all sorts of disturbances into account, which in experiment and in potential practical application occur, but which have to be added into the calculation in magnetic simulations. Nevertheless, simulations are very successful in predicting physical trends, which enables a first rough examination of a physical system. Combined with the respective experiments, magnetic simulations and in general simulations in all parts of physics are a very helpful tool to understand the behaviour of physical systems.

In this chapter, the used simulation methods are described. These methods are based on the theory given in Chapter 1 Introduction. The simulation scripts are written in the programming language Python and these scripts use other packages and simulation codes for the actual computation, which are written in more efficient programming languages for numerical computation. It is not the aim of this thesis to investigate the performance of simulation codes or to put some effort in the improvement of those. Throughout the thesis, applicable simulations are used to examine physical systems without being concerned about performance improvements of the available simulation codes, which are already proven to work fine within the limits of their applicability.

Reducing the number of magnetic moments in a system is necessary to enable feasible magnetic simulations. Since every atom in a physical system has its own magnetic moment, the number of magnetic moments is determined by the number of atoms n in a physical system. These n magnetic spins (the terms magnetic moments and magnetic spins are used synonymously) can interact with each other, which would lead to a computational effort of $\mathcal{O}(n^2)$, which can be reduced to an effort of $\mathcal{O}(n \cdot \log(n))$ by calculating interactions in the Fourier space and using clever transformation algorithms like the Fast Fourier Transform (FFT). (Abert, 2019) However, without further assumptions the computational effort would be enormous also for small magnetic systems in the micrometer regime. Therefore, further steps reducing the number of magnetic moments relevant for the calculation have to be taken. This leads to single spin simulations and the micromagnetic model, which are described in the following sections.

2.1 Single spin simulation

In single spin simulations, a system is assumed to have only one relevant magnetic moment, since all magnetic spins in the system are directed parallel to each other. This is a very rough assumption, but for a small magnetic sensor device this model might be able to predict the sensor outcome. The time evolution of a magnetic system is easy to be calculated, if this simulation model is applicable, since the LLGS equation (1.13) has to be solved only for one magnetization vector. Integration of this differential equation in explicit form can be done for example by using Runge-Kutta-algorithms. However, packages like Scipy (Virtanen et al., 2020) offer a large variety of different solvers, which exhibit better performances as simple Runge-Kutta-algorithms. In this thesis, single spin simulations are typically performed using the Scipy ordinary differential equation solver *vode* using Backward Differentiation Formulas (BDF), which is beneficial for stiff problems. A simple example script is presented in the Appendix A. This code performs a single spin simulation for an in-plane SOT-sensor device presented in Section 3.2, where the corresponding sensor signal for different external fields in z-direction is calculated by solving the LLGS equation for the different field strengths.

If different magnetization directions are present in the sample, this simulation model is not applicable anymore. For SOT-sensor designs with different magnetic domains the micromagnetic model has to be applied. Further, the working principles of multiturn sensors are based on different magnetization directions, which makes single spin simulations useless for those concepts.

2.2 Micromagnetics

Micromagnetic simulations are a very successful tool to examine the behaviour in magnetic structures. The review paper (Abert, 2019) gives a comprehensive overview over micromagnetics and the integration of spintronics into this theory. This section will mainly follow the information given in this report. The micromagnetic model is a deterministic model, which however takes quantum mechanical effects like the exchange interaction into account, that are necessary to ferromagnetism. The reduction of the total number of magnetic spins is based on the assumption, that the magnetization is kept parallel on a length scale λ well above the lattice constant a of the sample. Hence the condition (2.1) is required, where $\mathbf{S_{i/j}}$ are two distinct magnetic spins whose distance from each other is smaller than the characteristic length scale λ.

$$\mathbf{S_i} \approx \mathbf{S_j} \quad \text{for} \quad |\mathbf{x_i} - \mathbf{x_j}| < \lambda \gg a \tag{2.1}$$

This enables the approximation of the discrete spin distribution by a continuous magnetization vector density $\mathbf{M}(\mathbf{x})$. This magnetization can be normed by $\mathbf{M}(\mathbf{x}) = M_s \mathbf{m}(\mathbf{x})$ with the unit vector field $\mathbf{m}(\mathbf{x})$. (Abert, 2019, p. 1) This continuous model is not usable for numerical simulations. Therefore, the continuous magnetization field has to be discretized again. The trick is to discretize the volume with the magnetization field in much larger elements as the original atomistic lengths would do, such that the computational effort is kept feasible to handle. Depending on the new length scales of the discretization, this seems to be a very rough estimation, but if the magnetic spins are kept parallel in a large enough region, this model approximates magnetic systems quite well.

The discretization can be performed in different ways, where two types have been established in particular. The corresponding methods are the Finite Difference (FD) method and the Finite Element (FE) method and the different discretizations are schematically visualized in Figure 2.1. In the following, the main characteristics of the different methods and the used simulation codes should be mentioned without going further into detail. For further information please refer to the paper (Abert, 2019).

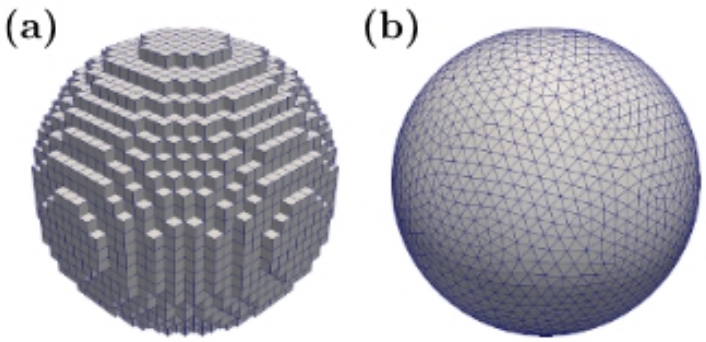

Figure 2.1: Discretization of a sphere. (a) Grid consisting of regular cubes for FD method. (b) Tetrahedral mesh for FE method. (taken from Abert, 2019, p. 22).

2.2.1 Finite Difference method

The FD method is based on the discretization in regular cubes. This grid of cuboids has the advantage, that the mathematical approximations/discretizations of derivatives and operations in general are easy to implement. By using accelerated implementations on Graphics Processing Units (GPUs), also small discretization lengths can be dealt with in acceptable simulation times. Therefore, the FD method is beneficial for easy geometries, since the simulation time can be kept small very well also for small cubes. However, the main disadvantage can be seen from Figure 2.1 as a sphere cannot be meshed appropriately. Of course, by choosing the cube lengths smaller and smaller, the spherical shape is approached, but the deviation from this shape stays noticeable at any cube length. Thus, the FD method has problems at simulating spherical shapes and other complex shapes in general.

In this thesis, the simulations for the SOT-sensor concept and the multiturn counter based on bubble memory are performed with the FD method, since the respective geometries are simple and can be meshed with regular cuboids appropriately. Also the out-of-plane device concept based on SOT is simulated with FD code, even though the shape is elliptical. However, the incorrect reconstruction of round edges does not influence the results in that case. Therefore, the FD method is appropriate with a fine grid. The used simulation packages are *Magnum.af* and *Magnum.np*. *Magnum.af* is a simulation package based on *ArrayFire*. (Yalamanchili et al., 2015) *Magnum.np* is a GPU enhanced simulation package (Bruckner et al., 2023) based on *PyTorch*. (Paszke et al., 2019) In the Appendix A, sample scripts are presented. For *Magnum.af*, a Hall Cross device exploiting SOT is simulated in the exemplary code. For *Magnum.np*, a simulation of an out-of-plane SOT-device is presented. Both sample simulations contribute to the results in this thesis.

2.2.2 Finite Element method

The FE method is more appropriate for complex structures due to the tetrahedral meshing, which enables the adequate discretization of complex geometries. This can be seen in Figure 2.1, where the sphere is reconstructed perfectly with the mesh. However, for this irregular meshing direct approximations of the differential equations are not possible. Therefore, the problem has to be solved differently by using the weak formulation of the original partial differentiation problem and undertaking some mathematical considerations. More details about this approach can be found in the paper (Abert, 2019). The advantage of this method is the ability to simulate any complex geometry. The drawback is the more complex implementation in numerical simulations.

In this thesis, the simulations of the multiturn counter based on the loop with obstacles are performed with the FE method. This is due to the more complex geometry, which could not be reconstructed perfectly with the FD method. The used simulation package is *Magnum.pi*, which is an FE simulation package based on *Firedrake*. (Ham et al., 2023) It is a further developed package of the simulation code *Magnum.fe* (Abert et al., 2013) based on *FEniCS*. (Alnaes et al., 2015) (Logg et al., 2012) In Appendix A an exemplary simulation script is shown, which simulates 4 obstacles in the form of cusps, which slow down the motion of a magnetic Domain Wall (DW) through the wire. The results of this simulation are presented in the thesis.

Chapter 3

Elliptically shaped sensor elements exploiting Spin Orbit Torque

3.1 Field sensing with out-of-plane device

A potential field sensor exploiting the SOT-effect is based on the SOT-induced magnetization switching in Magnetoresistive Random Access Memory (MRAM) elements explained in the paper by Zhu D. and Zhao W. (Zhu & Zhao, 2020). The sensor concept is presented in the paper by Koraltan S. et al. (Koraltan et al., 2023) and in the patent application by Süss D. et al. (Suess et al., 2021). This out-of-plane device is illustrated in Figure 3.1. The current J_{SOT} flowing in the heavy metal induces an SOT in the free magnetic layer. The initial magnetization of the free magnetic layer is pointing out of plane in z-direction $(0,0,1)^T$ and the polarization vector is pointing into negative y-direction $(0,-1,0)^T$, if the current flows in positive x-direction.

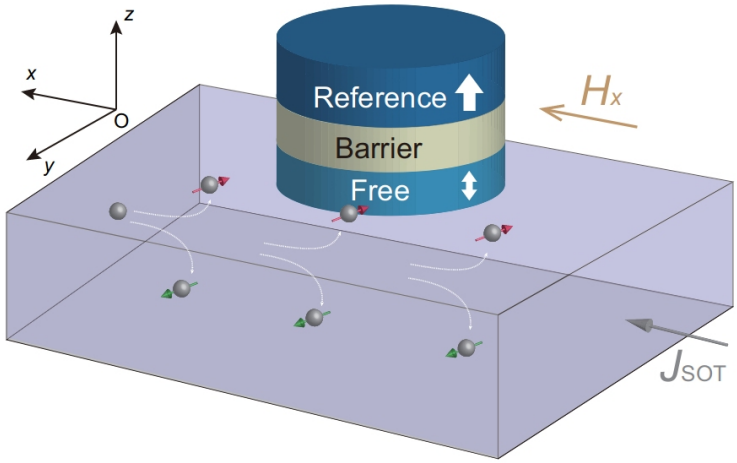

Figure 3.1: Illustration of out-of-plane device. (taken from Zhu & Zhao, 2020, p. 3).

The induced SOT leads to a deviation of the free layer magnetization from the z-axis. This deviation can be quantified by measuring the z-component of the magnetization in the free magnetic layer exploiting a type of magnetoresistance, for example TMR or GMR. Therefore, a reference layer magnetized in positive z-direction and a barrier, which is isolating in the case of TMR or conducting and non-magnetic in the case of GMR, are introduced above the free magnetic layer. By measuring the resistance in z-direction, the z-component of the magnetization of the free magnetic layer can be quantified.

If no external field in x-direction H_x is applied, reversing the current direction from +x to −x and therefore reversing the polarization vector leads exactly to the opposite deviation of the magnetization vector from the z-axis than current flowing in +x-direction. An external magnetic field changes this situation and introduces some sort of asymmetry in the system, which depends on the strength of the magnetic field. This can be used for field sensing. The according signal of the device is proportional to the difference between the z-components of the free magnetic layer for the SOT-current flowing either in +x ($m_{z,+J}$) or −x-direction ($m_{z,-J}$):

$$\text{Signal} \propto m_{z,+J} - m_{z,-J}$$

Further investigation of this sensor design focuses mainly on the impact of the magnetic parameters and other system parameters on the signal output and the according linear range as the potential working window of the sensor.

3.1.1 Variation of magnetic parameters in simulation

In the following section simulations are performed in the form of magnetic field sweeps in x-direction to examine how the system parameters influence the output of the system. Therefore the magnetic parameters uniaxial anisotropy K, saturation magnetization $\mu_0 M_s$ and exchange constant A of the free magnetic layer are varied. Furthermore, the impact of the current density J_e, the elliptical shape and an additional magnetic field in z-direction $\mu_0 H_z$ is investigated. For this purpose an elliptical out-of-plane sensor device is simulated using the finite-difference method. The simulated sensor element is illustrated with the standard elliptical shape in Figure 3.2. The parameters quantifying the SOT-efficiencies are chosen to be $\eta_{\text{damp}} = -0.09$ and $\eta_{\text{field}} = 0.17$, which are parameters that evolved during the scientific project this thesis belongs to. The main parameter values, that are varied one by another in the following paragraphs, are: $J_e = 2.4 \cdot 10^{11}$ A/m^2, $\mu_0 M_s = 0.75$ T, $K = 0.24$ MJ/m^3 and $A = 9$ pJ/m. The sensor principle works also for round sensor elements, but the standard elliptical shape for the following simulations is chosen such that the ratio between major and minor axis is 5:3. Regularly, no additional magnetic field in z-direction is applied. The Gilbert damping parameter is set to $\alpha = 0.1$.

Figure 3.2: Visualization of the magnetic part of the simulated sensor element.

Variation of the current density: First the impact of the SOT-current density should be investigated. Since higher current densities lead to stronger torques, they should increase the slope of the transfer curve and therefore decrease the linear range of the signal. This can be seen in the simulation data visualized in Figure 3.3. Here, the 3 different current densities $J_e = 1.2 \cdot 10^{11}$ A/m^2, $J_e = 2.4 \cdot 10^{11}$ A/m^2 and $J_e = 4.8 \cdot 10^{11}$ A/m^2 are exploited. The higher the current density, the higher is the slope of the transfer curve and the lower is the linear range, consequently, making it beneficial to use smaller currents.

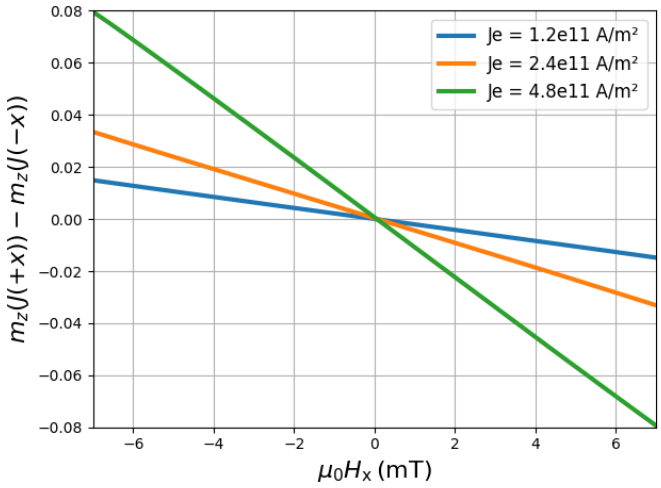

Figure 3.3: Impact of current density variation on transfer curve of out-of-plane device.

Variation of the uniaxial anisotropy: An uniaxial anisotropy in z-direction should hamper the tilting of the magnetization vector due to the SOT-effect. Thus, a higher uniaxial anisotropy in z-direction should lead to a flatter signal curve and to a higher linear range. This is visualized in the simulation data in Figure 3.4. In Figure 3.4a a small range of the field sweep is illustrated showing that the higher the uniaxial anisotropy, the lower is the slope of the transfer curve, which increases the potential working window of the sensor. Figure 3.4b visualizes a wider range of the field sweep and shows the exact same result. Methods of how to increase the uniaxial anisotropy in a material are presented at a later stage of the thesis.

Variation of the saturation magnetization: Figure 3.5 shows the signal curves for different values of the saturation magnetization $\mu_0 M_s$. The higher it is, the smaller is the linear range of the curve (the green curve has just a very small slope). This is a bit unintuitive, since by the expressions (1.11) and (1.12) M_s should have the opposite impact on the torque efficiency as J_e. However, M_s seems to have a more complex influence. Thus, choosing a material with an adequate saturation magnetization improves the potential working range of the sensor.

Variation of the exchange constant: A variation of the exchange constant should not have any significant impact on the slope of the transfer curve. This is confirmed by the simulation data in Figure 3.6, where the change due to different exchange constants is negligible.

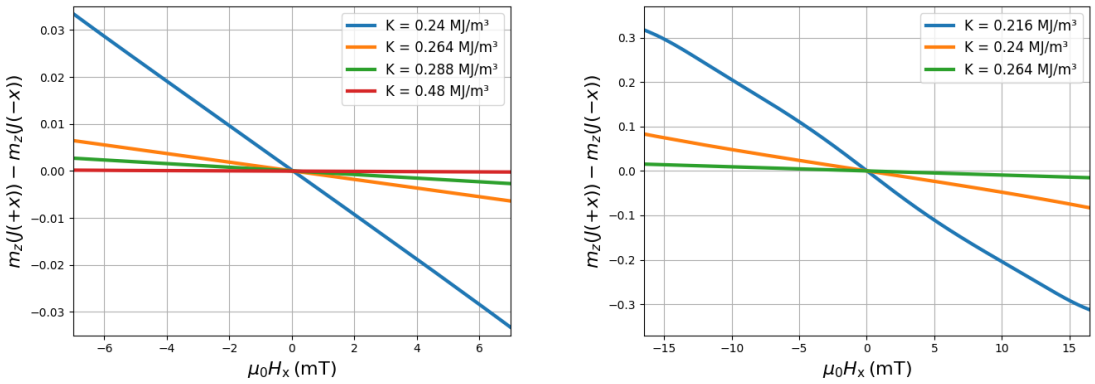

(a) Tighter range of the field sweep.

(b) Wider range of the field sweep.

Figure 3.4: Impact of uniaxial anisotropy variation on transfer curve of out-of-plane device.

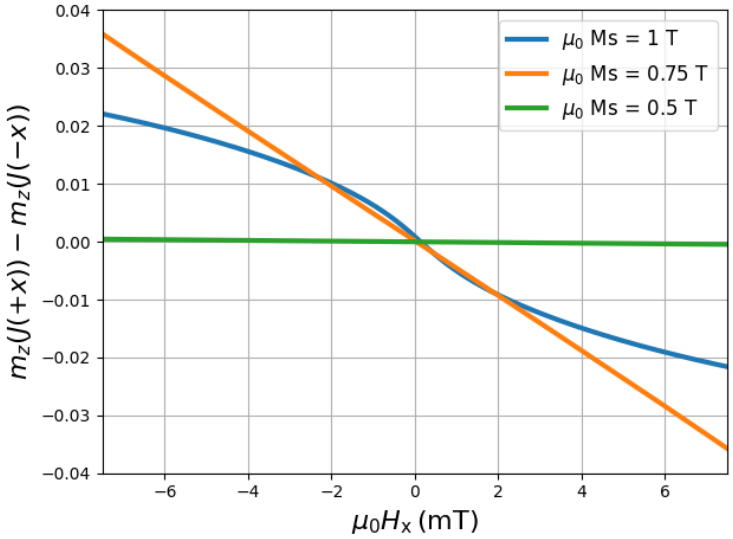

Figure 3.5: Impact of saturation magnetization variation on transfer curve of out-of-plane device.

Variation of the elliptical shape: Producing a more elliptical sensor element increases the shape anisotropy of the element making it favourable for the magnetization to point along the x-axis. This increases the efficiency of the tilting from the z-axis. Therefore, the longer the major axis is with respect to the minor axis of the sensor element, the higher should be the slope of the transfer curve and consequently the lower should be the linear range of the signal curve. This can be seen in the simulation result visualized in Figure 3.7. The higher the shape ratio of major axis to minor axis, the higher is the slope of the curve, making it favourable to use circular sensor elements.

Exertion of a magnetic field in z-direction: Applying an additional magnetic field in z-direction should have a similar impact than an uniaxial anisotropy in z-direction, since the tilting of the magnetization vector is hampered and the linear range of the signal curve should be increased. However, exerting a z-field shows an interesting behaviour. In Figure 3.8, the impact of this exertion is illustrated for different field strengths between 0 mT and 20 mT. Note that the range of the field sweep is chosen to be significantly higher to visualize the changing behaviour of the signal curve for different applied field strengths. Besides the signal curve, also the curves of the z-magnetization for the

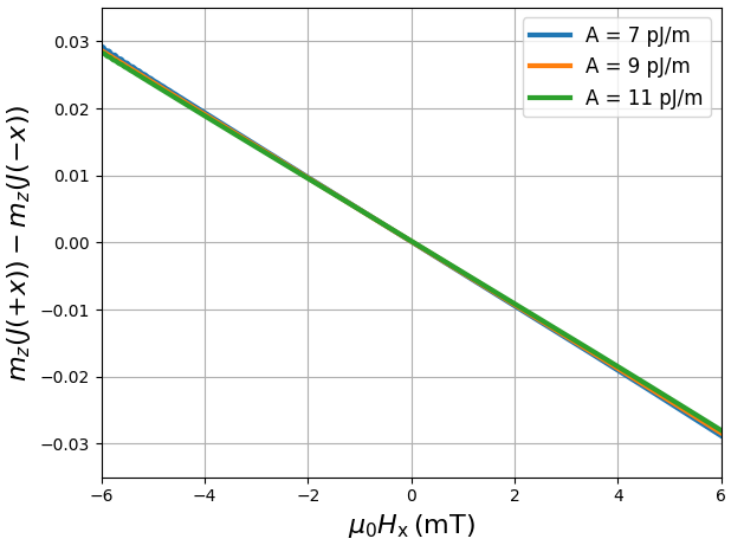

Figure 3.6: Impact of exchange constant variation on transfer curve of out-of-plane device.

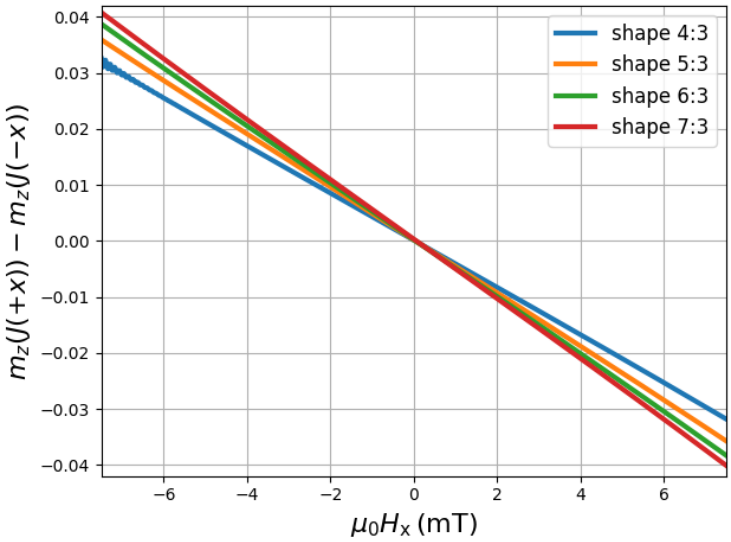

Figure 3.7: Impact of shape variation on transfer curve of out-of-plane device.

different current directions is illustrated. For zero field the sensor exhibits a very small linear range. For $\mu_0 H_z = 5$ mT, a small linear range in between appears. This is due to the hindered switching of the magnetization due to the SOT. So instead of switching at $\mu_0 H_x = 0$ mT the sign of the z-magnetization changes at approximately $\mu_0 H_x = \pm 8$ mT. For $\mu_0 H_z = 10$ mT this behaviour appears more significantly and the switching happens at approximately $\mu_0 H_x = \pm 20$ mT, leaving behind a linear range in between -20 mT and +20 mT (or slightly beyond it). For $\mu_0 H_z = 20$ mT the linear part expands even further and the boundaries are no more visible in the chosen range. Thus, applying an additional magnetic field in z-direction as a bias improves the linear range of the sensor element.

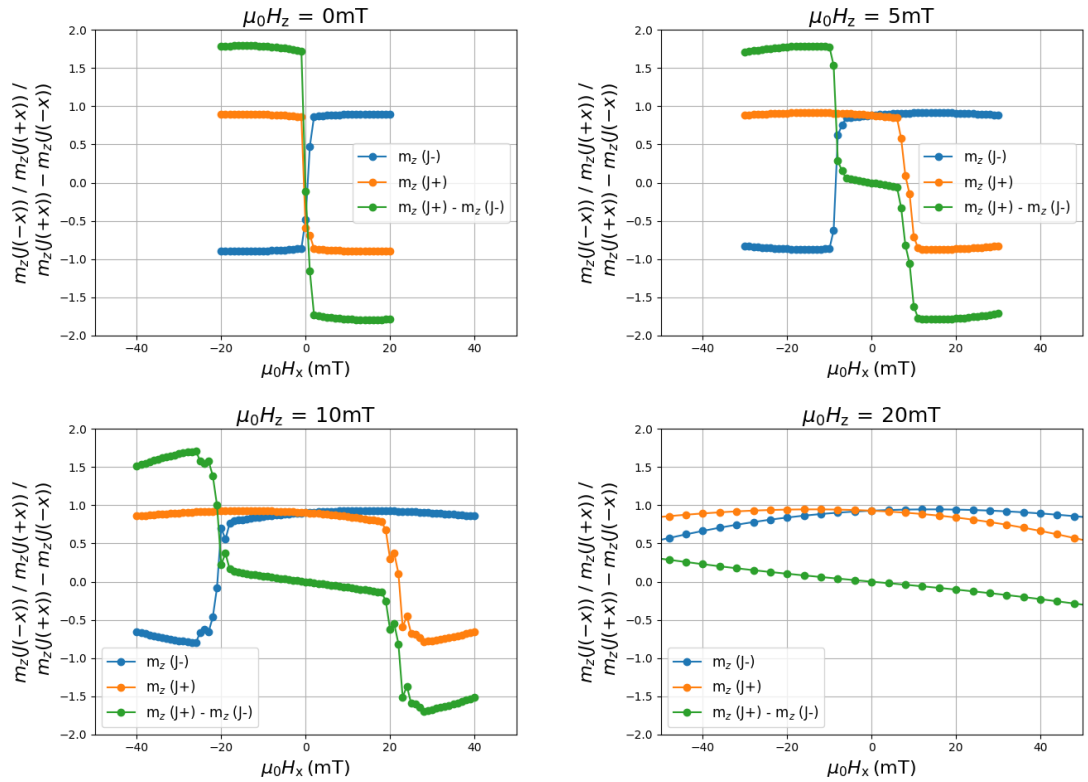

Figure 3.8: Impact of different additional magnetic fields in z-direction on transfer curve of out-of-plane device.

3.2 Field sensing with in-plane device

The in-plane device is similar to the out-of-plane device presented above. However, the initial magnetization of the free magnetic layer with flowing SOT-current is pointing in-plane in the y-direction, which is the reason for the device to be referred to as in-plane device. It is not sensitive to magnetic fields in x- or y-direction but to magnetic fields in z-direction. An illustration of this sensor design is given in Figure 3.9.

The current J_{SOT} in the heavy metal induces an SOT in the free magnetic layer, which leads to a magnetization $\mathbf{M}$ of the free magnetic layer pointing along the y-axis without external field. If no external field is applied, reversing the current direction from $+$x to $-$x leads to the opposite magnetization direction as if the current would flow in $+$x-direction. An external magnetic field in z-direction H_z leads to a tilting of the magnetization from the y-axis dependent on the current direction, which enables field sensing. The simple current circuit, which is used for this sensor element, is shown in Figure 3.10. The two current directions used to extract a signal out of the sensor are depicted and xMR stands for any magnetoresistance exploited to measure the x-magnetization of the free magnetic layer.

The signal of this in-plane device is proportional to the difference between the x-magnetizations of the free magnetic layer for the SOT-current flowing either in $+$x ($m_{x,+J}$) or $-$x-direction ($m_{x,-J}$):

$$\text{Signal} \propto m_{x,+J} - m_{x,-J}$$

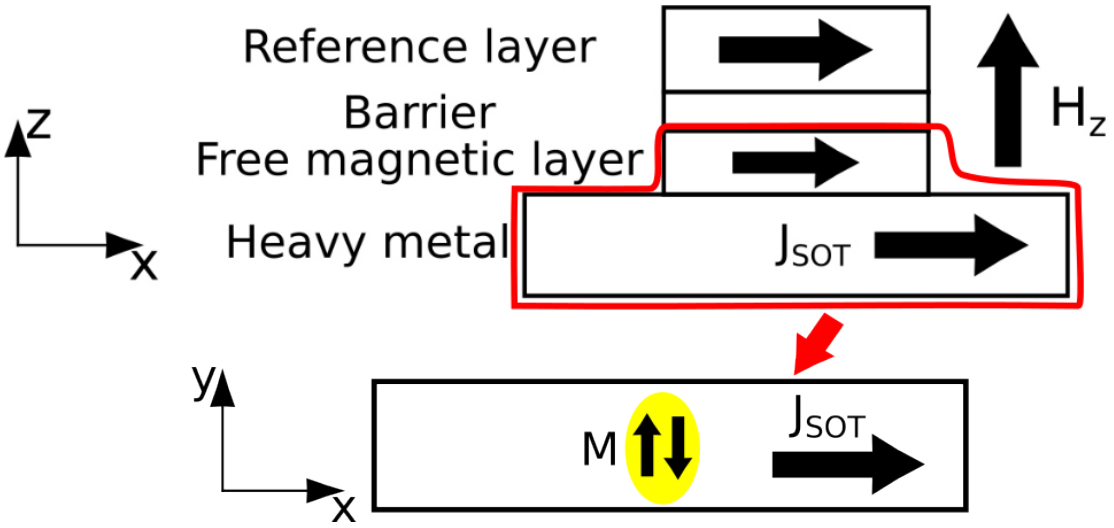

Figure 3.9: Illustration of the in-plane device.

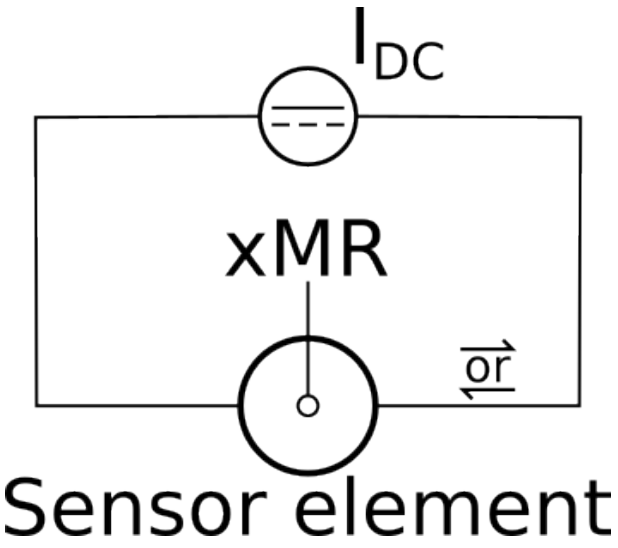

Figure 3.10: Illustration of potential current ciruit.

In magnetic simulations, the magnetization is computed directly and the practical need of a magnetoresistance to measure the magnetization is neglected. However, the simulations show trends that could be realized by well-designed read-out techniques. Therefore, the sensor design should be examined by means of single spin simulations. The shape of the free magnetic layer and the other layers on top of the heavy metal is round or elliptical with the long axis in y-direction according to the coordinate system introduced in Figure 3.9. The reason for the elliptical shape is the implementation of a shape anisotropy as additional anisotropy in y-direction, which is discussed below in Section 3.2.1. For the first examination of the system the following parameters are chosen: The saturation magnetization is set to $J_s = \mu_0 M_s = 0.5$ T, the thickness of the free magnetic layer is chosen to be $d = 2.5$ nm, the Gilbert damping parameter is set to 0.01, the uniaxial anisotropy constant for anisotropy in z-direction amounts to 10^5 J/m^3 and the current density is chosen to be $5 \cdot 10^{12}$ A/m^2, which would result in a current of less than 1 A for typical sensor dimensions. The anisotropy in z-direction seems to be high forcing the magnetization to point along the z-axis. However, DLT and FLT introduced by the

flowing SOT-current lead to a magnetization along the y-axis without external field in z-direction due to the polarization vector in y-direction. The shape is chosen to be round introducing no addtional anisotropy other than the anisotropy in z-direction. In Figure 3.11 the sensor transfer curve, which gives the connection between the signal and the entity to be measured, is shown for the mentioned parameter values. The linear range is surprisingly high for such a simple sensor realization, ranging from -100 mT to +100 mT.

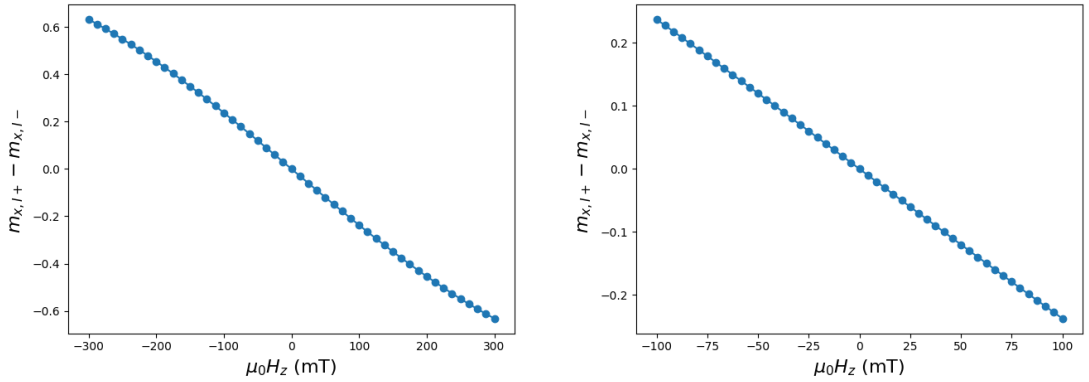

Figure 3.11: Transfer curves for different ranges of the magnetic field in z-direction.

The offset of this sensor is zero in the simulation, which was expectable for the given setup with pure magnetic fields in z-direction. However, this is an artificial situation since the field to be measured might be distorted with non-negligible x- or y-components or with additional fields as disturbing noise. Therefore, it is crucial to examine the system with additional x- and y-fields. To prove zero-offset also for x- and y-field components, they are added to the overall magnetic field in the simulation. In Figure 3.12 the corresponding transfer curves for pure x- or y-fields as disturbances are shown, where the field strength of the additional field is chosen to be 10 mT. It turns out, that disturbing fields either solely in x-direction or in y-direction do not affect the zero-offset of the sensor element, which at first seems promising. The slope of the transfer curves are different compared to the original one, which disables field sensing with this simple design. However, it has to be mentioned, that a disturbing field of 10 mT for the given measurable field range is quite high. Moreover, by using more of these zero-offset sensor elements with different alignments and by combining their signals, field sensing might be possible.

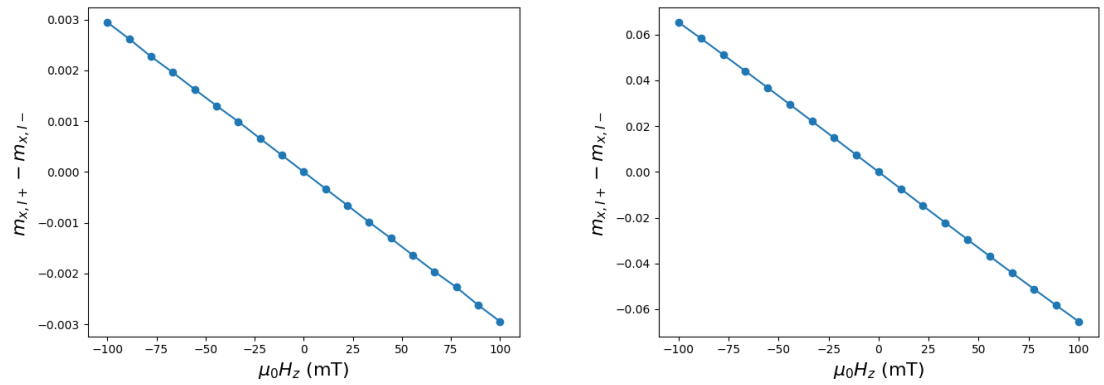

(a) Additional x-field of 10 mT.

(b) Additional y-field of 10 mT.

Figure 3.12: Transfer curves for disturbing fields either in x- or in y-direction.

Until now, only disturbing fields solely in x- or in y-direction were applied. Another problem appears when going one step further and applying disturbing magnetic fields with both x- and y-component. In Figure 3.13a a disturbing field of $\mu_0 H = 5$ mT $\cdot (1, 1, 0)^\mathsf{T}$ is applied in addition to the magnetic field in z-direction. Besides a small bending of the transfer curve, this leads to a conspicuous offset of approximately -45 mT. The examined disturbing field is quite high, but the immense offset suggests that also for small disturbing fields the offset is not negligible at all. In Figure 3.13b a rotating disturbing field of 1 mT is applied to measure the offset depending on the angle of the field to the x-axis. Note that in simulation no z-field is applied and that the offset is quantified in terms of the magnetization difference, so in terms of the actual signal at zero field. For pure x-fields (0° and 180°) and pure y-fields (90° and 270°) the offset is zero, whereas it is non-zero in between. Where the disturbing field is aligned 45°, 135°, ... to the x-axis, the offset reaches its maximum. This is, where the x- and y-component are equal in magnitude. In the following, the dependency of this offset on different parameters is investigated.

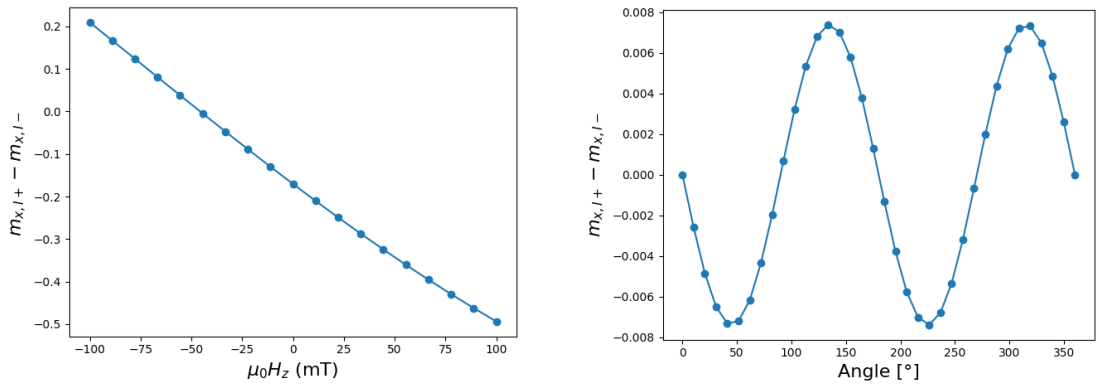

(a) Additional magnetic field of 5 mT in x-direction and 5 mT in y-direction.

(b) Offset of transfer curve for a rotating disturbing field of 1 mT.

Figure 3.13: Transfer curve behaviour for disturbing fields in x- and in y-direction.

3.2.1 Offset dependency on additional anisotropy

A parameter, that could be adapted to reduce the offset by reducing the impact of disturbing y-fields, is an additional anisotropy. This additional anisotropy in y-direction leads to a magnetization vector, that tends to align according to the additionally introduced easy axis and therefore lowers the maximum offset for disturbing fields aligned 45°, 135°, ... to the easy axis. There are some ways to introduce such an additional anisotropy in the sensor element. One possibility is to use an elliptical form for the sensor element, where the major axis of the ellipsis defines the additional easy axis. This is called shape anisotropy. Other possibilities would be to apply a magnetic field during film-growth or to use specific crystal substrates. (Lim et al., 2022) In Figure 3.14a, an additional anisotropy in y-direction is introduced. The higher the additional anisotropy is, the lower is the offset. The values for the anisotropy field range from 0 mT to 10 mT, which is small compared to the original anisotropy in z-direction, where the coercive field in z-direction is $\mu_0 H_{k,z} = 125$ mT. The magnitude of the rotating disturbing field is 1 mT.

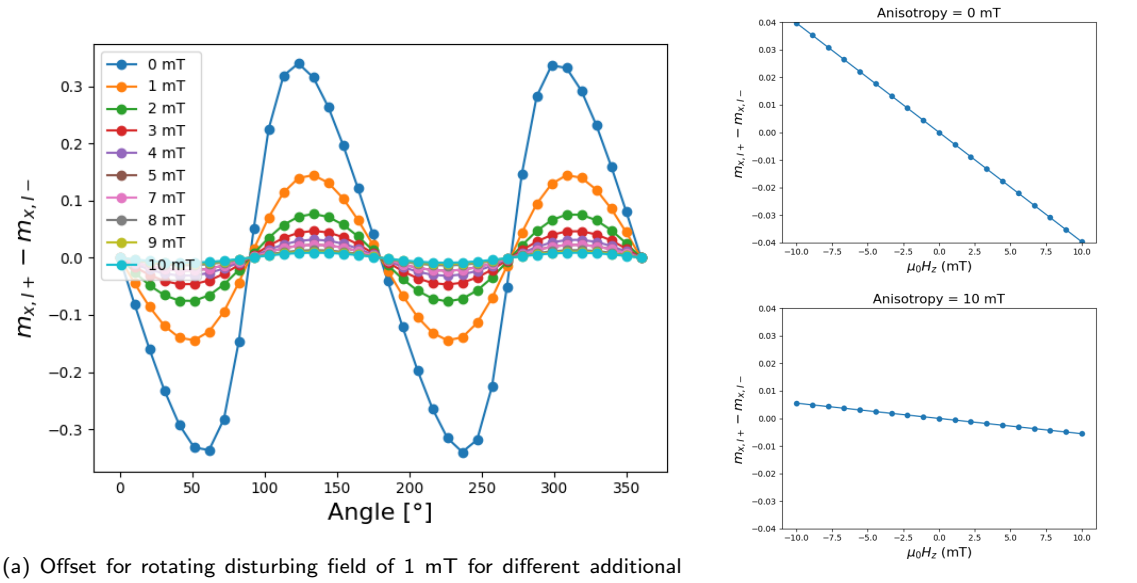

(a) Offset for rotating disturbing field of 1 mT for different additional anisotropy fields in y-direction named in the legend.

(b) Transfer curve for additional anisotropy fields of 0 mT and 10 mT.

Figure 3.14: Offset dependency on additional anisotropy in y-direction.

Nevertheless, it has to be taken into account, that introducing an additional anisotropy also reduces the actual signal, which might make the offset lowering non-profitable. This can be seen in Figure 3.14b, where the transfer curves for additional anisotropy fields of 0 mT and 10 mT are depicted. The signal strength is reduced by a factor of approximately 10. The offset reduction is bigger than the signal reduction, which shows that the introduction of an additional anisotropy is beneficial to realize offset-reduction.

3.2.2 Offset dependency on η_{field} and η_{damp}

Other parameters that might influence the offset are η_{field} and η_{damp}, which are the coefficients for the fieldlike and dampinglike torque, respectively. These depend on the choice of the materials used in the in-plane sensor. To extract these parameters there are different experimental methods. Prominent examples of such extraction methods are the Hayashi method (Hayashi et al., 2014) and the Dutta method (Dutta et al., 2021). Without going further into detail about these methods, the offset dependency on these parameters is observed. In Figure 3.15 the signal offset for a rotating field of 1 mT is examined for different values of η_{field} and a fixed value of $\eta_{\text{damp}} = 0.1$. This examination is repeated for a different value of $\eta_{\text{damp}} = 0.01$ in Figure 3.16. In the left plots, the range of η_{field}-variation is 0 to 0.09, whereas it is 0.10 to 0.19 in the right plots. Note that the graphs on the right showing the dependencies for higher values of η_{field} have another y-range than the graphs on the left for reasons of visibility.

The figures illustrate that the FLT is responsible for the offset and that the signal offset increases for increasing values of η_{field} until a threshold of $\eta_{\text{field}} = 0.06$. Above this threshold the offset decreases for increasing η_{field} values. It is remarkable that the maxima of the signal offset are shifted away from 45°, 135°, ... so strongly, especially at and around the threshold value of $\eta_{\text{field}} = 0.06$.

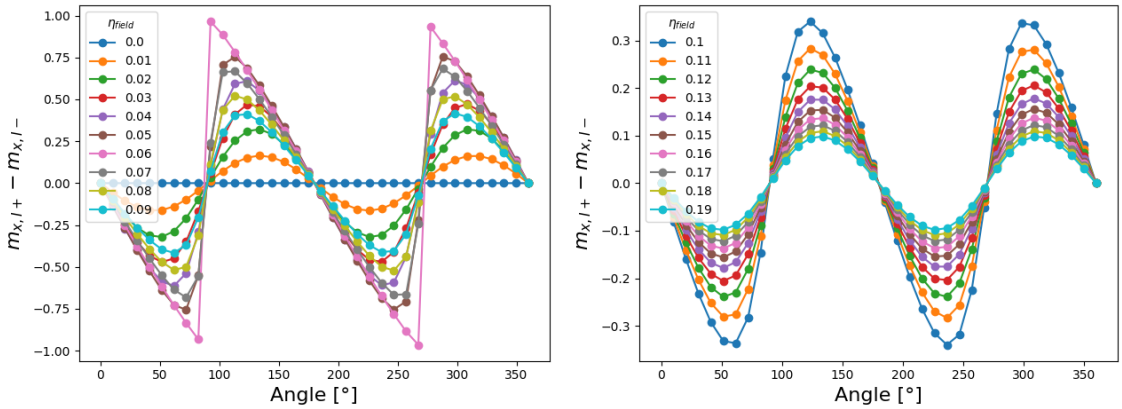

Figure 3.15: Offset for rotating disturbing field of 1 mT for $\eta_{\text{damp}} = 0.1$ and different values of η_{field}. (The left figure displays values from 0 to 0.09 and the right figure displays values from 0.10 to 0.19).

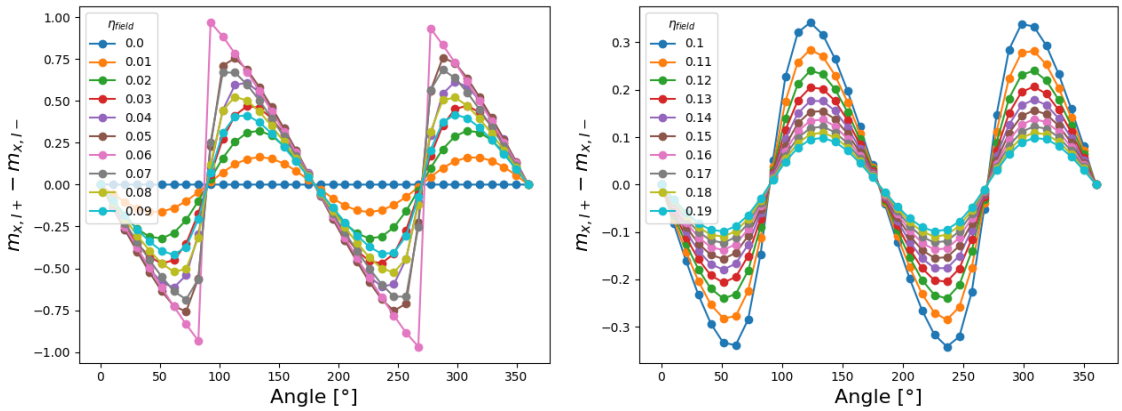

Figure 3.16: Offset for rotating disturbing field of 1 mT for $\eta_{\text{damp}} = 0.01$ and different values of η_{field}. (The left figure displays values from 0 to 0.09 and the right figure displays values from 0.10 to 0.19).

From the above results it is already clear that η_{damp} has no effect on the offset behavior of the in-plane sensor element. To validate this observation the offset behaviour for a rotating field of 1 mT is investigated for fixed η_{field} values and different values of η_{damp}. In Figure 3.17 and 3.18 the simulations are performed with the values $\eta_{\text{field}} = 0.1$ and $\eta_{\text{field}} = 0.01$, respectively. In the left plots, the range of η_{damp}-variation is 0 to 0.09, whereas it is 0.10 to 0.19 in the right plots. Note that the plot on the right in Figure 3.18 showing the dependencies for higher values of η_{damp} has another y-range than the plot on the left for reasons of visibility.

As expected, the offset does not depend on η_{damp} in Figure 3.17. However, for very high values of η_{damp} at $\eta_{\text{field}} = 0.01$ there appear some offset fluctuations, which might have its origin in the numerical approach of solving the underlying differential equations. Probably, these fluctuations are non-physical and can be neglected in the offset reduction.

The circumstance that the offset does not depend on η_{damp} can be explained analytically. For the LLGS equation (1.13), an expression can be extracted for the equilibrium by requiring that the magnetization does not change anymore in time. This expression is given in (3.1). For further analytical examinations of the LLGS equation the reader is referred to (Zhu & Zhao, 2020).

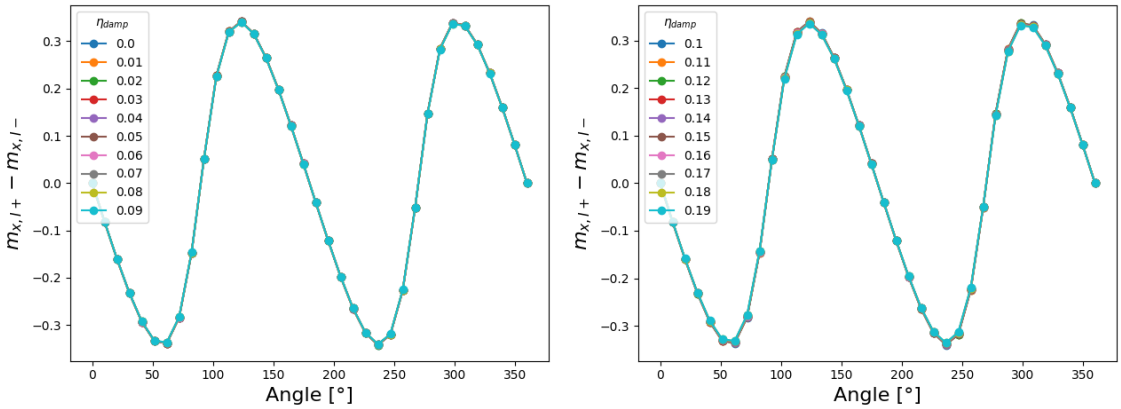

Figure 3.17: Offset for rotating disturbing field of 1 mT for $\eta_{\text{field}} = 0.1$ and different values of η_{damp}. (The left figure displays values from 0 to 0.09 and the right figure displays values from 0.10 to 0.19).

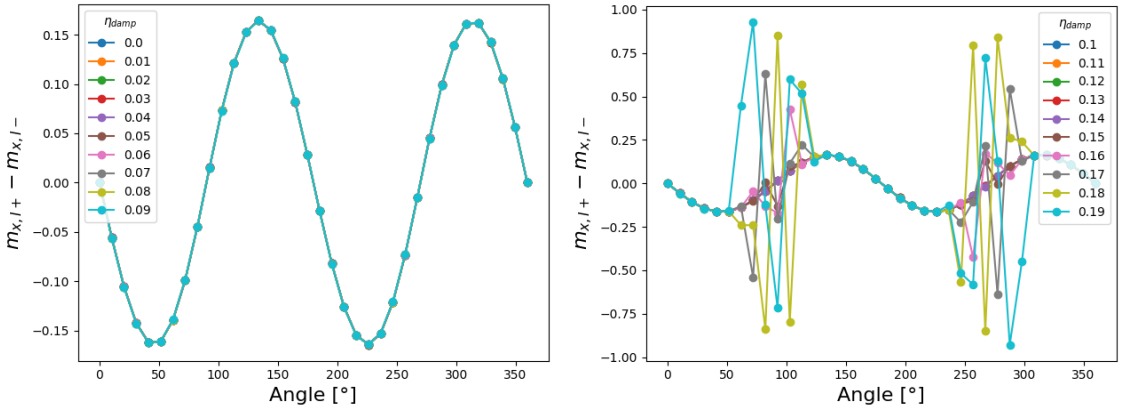

Figure 3.18: Offset for rotating disturbing field of 1 mT for $\eta_{\text{field}} = 0.01$ and different values of η_{damp}. (The left figure displays values from 0 to 0.09 and the right figure displays values from 0.10 to 0.19).

$$\mathbf{m} \times \left[\mathbf{H_{eff}} - \frac{j_e \hbar}{2et\mu_0 M_s} \left[\eta_{\text{damp}} \mathbf{p} \times \mathbf{m} + \eta_{\text{field}} \mathbf{p} \right] \right] = 0 \tag{3.1}$$

Without an applied external field the magnetization is pointing parallel to the y-axis due to the FLT and DLT terms, since the polarization vector is $(0,-1,0)^T$ or $(0,1,0)^T$ depending on the current direction. The DLT leads to a tilting of the magnetization vector into the x-direction if an external field in z-direction H_z is applied. This can be seen by looking at the contribution of the DLT term and neglecting the FLT in equation (3.2). Computing the cross-product in the inner brackets for the different polarization vectors (3.3) leads to the mentioned observation. The magnetization vector gets a small z-component m_z due to H_z, which leads to a respective reduction of the y-component of the vector. The DLT results in a tilting of the vector in the x-direction.

$$\mathbf{m} \times \left[\mathbf{H_{eff}} - \frac{j_e \hbar}{2et\mu_0 M_s} \left[\eta_{\text{damp}} \mathbf{p} \times \mathbf{m} \right] \right] = 0 \tag{3.2}$$

$$\mathbf{p_{I_\pm}} \times \mathbf{m} = \begin{pmatrix} 0 \\ \mp 1 \\ 0 \end{pmatrix} \times \begin{pmatrix} 0 \\ \sqrt{1 - m_z(H_z)^2} \\ m_z(H_z) \end{pmatrix} = \begin{pmatrix} \mp m_z(H_z) \\ 0 \\ 0 \end{pmatrix} \tag{3.3}$$

The above analytical examination especially implies that the signal offset of the sensor is zero if only the DLT is taken into account, since for $H_z = 0$ (valid for the offset) no tilting happens. This directly leads to the finding that the FLT is responsible for the offset.

Additional anisotropy and the insight on the dependencies of the offset on the parameters η_{field} and η_{damp} can be exploited to reduce the signal offset of the in-plane sensor device. Other material parameters and the current strength also affect the offset and by choosing the material composition and the used current density wisely it can be reduced even further. Concerning the SOT-current a higher current density reduces the signal offset. However, it cannot be reduced to zero. Therefore, a potential explanation of the offset and a possible workaround should be provided in the following.

3.2.3 Offset explanation and workaround

The main reason for the offset comes from the asymmetry of the elliptical in-plane sensor with respect to the different current directions and external fields not pointing exactly in x- or y-direction. The elliptical shape provides a given initial magnetization, which is different for the two possible current directions I_+ and I_-. This is visualized in Figure 3.19. If no magnetic field is applied, the magnetization equals the initial magnetization. If a magnetic field is applied in x- or y-direction solely, the tilting of the magnetization direction happens to be symmetric. If it is applied in another direction, especially in the direction 45° off the x-axis H_{xy}, the situation is not symmetric anymore. This is also illustrated in Figure 3.19. The tilting of the magnetization for I_+ is small compared to the tilting of the magnetization for I_-. Since the signal is proportional to $m_{x,I_+} - m_{x,I_-}$, the sensor signal appears with an offset.

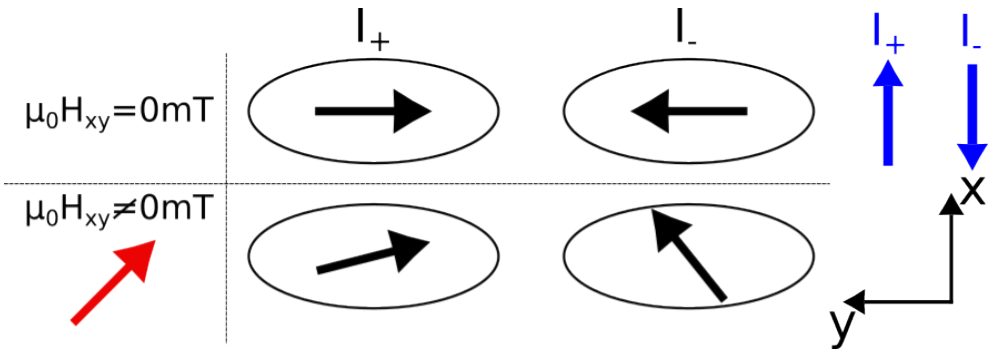

Figure 3.19: Tilting of magnetization due to no magnetic field or a magnetic field rotated 45° from x-axis for different current directions.

A simple solution to the offset problem is to remove the asymmetry from the sensor element, which causes the offset. This can be done by combining the sensor signals of two in-plane sensor elements which are rotated 90° to each other. This workaround is visualized in Figure 3.20. By adding up the sensor signals of the two elements a new signal is generated, which shows symmetry concerning disturbing in-plane magnetic fields in any direction. The disadvantage of this workaround is the need of 2 sensor elements, but that would be no serious drawback in practical realizations since such sensor elements are easy and cheap to produce.

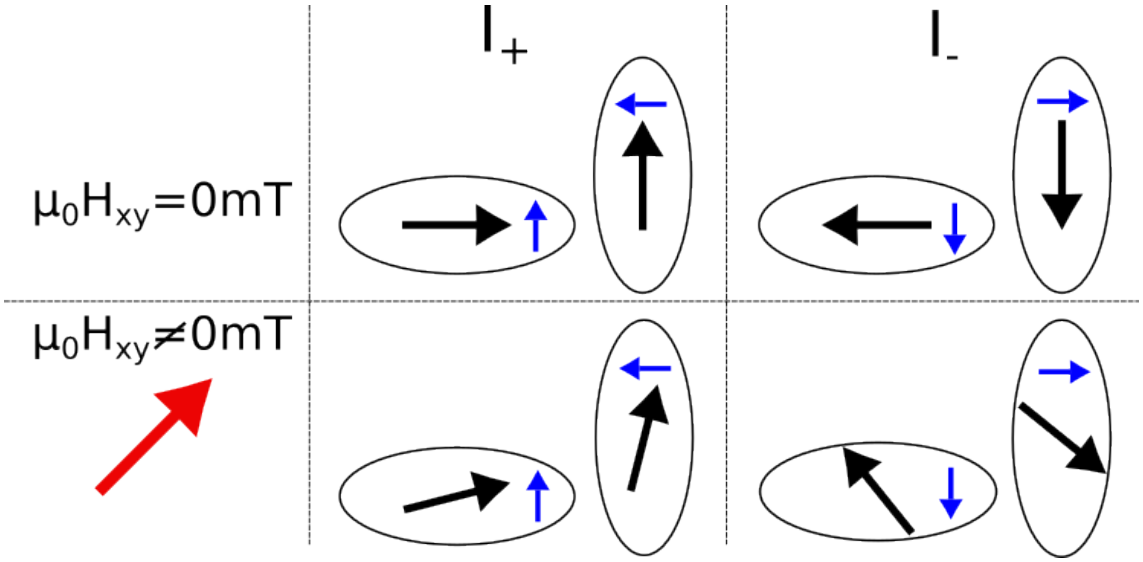

Figure 3.20: Potential workaround avoiding the signal offset of the single in-plane sensor element. The red arrow depicts the magnetic field rotated 45° from the x-axis and the little blue arrows visualize the current directions in each sensor element.

3.3 Wheatstone SMR-sensor (results from (Xu et al., 2018))

In the following section, a sensor design proposed by a Chinese group around Yanjun Xu et al. from 2018 should be investigated. The title of the corresponding paper calls the sensor design an "Ultrathin All-in-One Spin Hall Magnetic Sensor with Built-In AC Excitation Enabled by Spin Current" and the paper appeared in the journal *Advanced Materials Technologies*. (Xu et al., 2018) The sensor consists of 4 distinct sensor elements, which are arranged in a Wheatstone bridge circuit. The design is shown in Figure 3.21. Note here, that the illustration of the heavy metal layer (Platinum Pt) and the free ferromagnetic layer (Nickel-iron NiFe) with the according current paths is a bit misleading. The current flows through the heavy metal layer and the magnetization gets tilted in the adjacent free magnetic layer. In Figure 3.22 the circuit depiction is simplified and the circuit is identified to be a typical Wheatstone bridge.

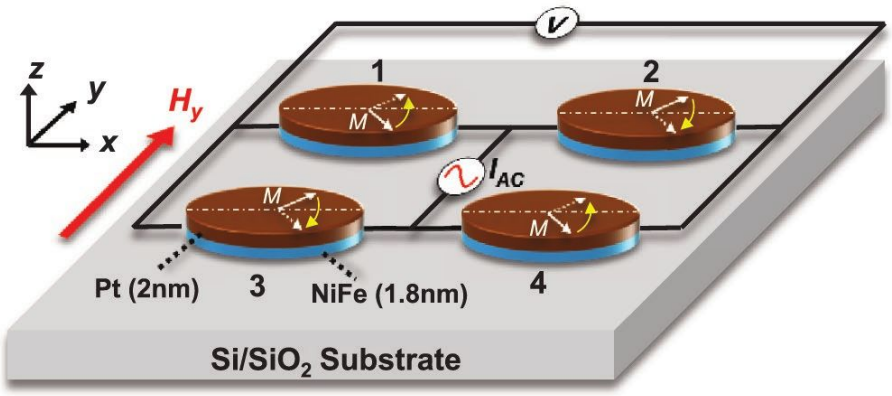

Figure 3.21: Schematic illustration of the Wheatstone SMR-sensor. (taken from Xu et al., 2018, p. 7).

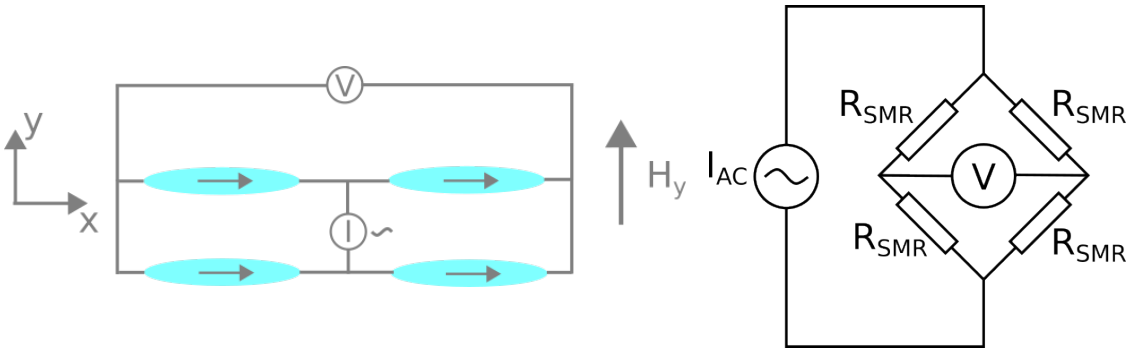

Figure 3.22: Simple schematic of Wheatstone SMR-sensor and Wheatstone bridge circuit.

The distinct sensor elements consist of a 2 nm thick Platinum heavy metal layer and a 1.8 nm thick Nickel-iron layer as the ferromagnetic free layer. These elements are of elliptical shape with a ratio long axis to short axis of 4:1 and they are grown up on a Si/SiO_2 substrate. The working principle of this sensor design is based on the coexistence of the Spin Hall Magnetoresistance (SMR) and the SOT in the bilayers of the distinct sensor elements. By using Alternating Current (AC) current for the supply of the Wheatstone bridge, the demonstrated sensor seems to be an all-in-one magnetic sensor that features a simple structure, nearly zero Direct Current (DC) offset, negligible hysteresis, a high sensitivity and low noise. For small fields it can be used as field sensor, but also as rotation and vibration detector. (Xu et al., 2018)

To examine this type of sensor design the experimental properties demonstrated in the paper are presented in the following. Afterwards, some simulations are performed to confirm the properties and also to investigate the properties at higher magnetic fields. First of all, the origin of the sensor signal has to be examined analytically. The current flows symmetrically through the upper and the lower branch in Figure 3.21, so the same amount of current flows through the elements 1 and 2 as it flows through the elements 3 and 4. Therefore, the voltage signal can be described by looking only at one branch. In Figure 3.23 one branch, in this case the lower branch, is illustrated with the according current flows and the schematic magnetization tilting due to the applied external magnetic field.

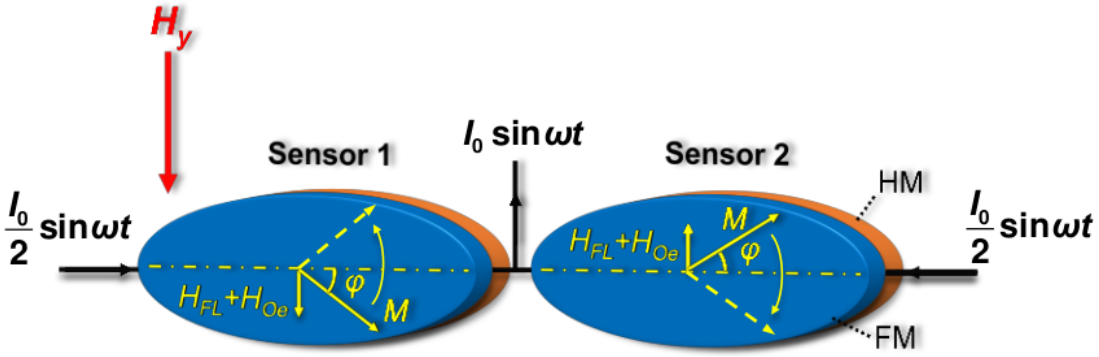

Figure 3.23: One branch of the Wheatstone SMR-sensor. (taken from Section 2 of Supporting Information of Xu et al., 2018).

For the exact derivation of the voltage output of the sensor the reader is referred to the Supporting Information of (Xu et al., 2018). Here, only the final formulas for the signal taken from the mentioned source should be discussed. The voltage output of the Wheatstone SMR-sensor V_{out} is given in equation (3.4), where I_0 is the current amplitude ($I = I_0 \sin\omega t$), ΔR_0 is the resistance offset difference between the elements 1 and 2, ω is the angular frequency of the current and α is the SOT-efficiency parameter with the property that the overall SOT-bias field can be written as $H_{\text{bias}} = H_{\text{FL}} + H_{\text{Oe}} = \alpha I$ with H_{FL} being the effective field contribution from the FLT and H_{Oe} being the Oersted field generated due to the current flow through a conductor. ΔR takes into account the changes in resistance due to magnetoresistance effects and is given as $\Delta R = \Delta R_{\text{SMR}} + \Delta R_{\text{AMR}}$ with ΔR_{SMR} being the contribution of SMR and ΔR_{AMR} being the contribution of AMR. Therefore, the overall magnetoresistance is given as $R = R_0 + \Delta R \sin^2\varphi$ with R_0 being the resistance offset and φ being the angle between the current direction and the magnetization. At this point, it has to be mentioned that besides SMR also AMR can be used for the measurement. However, SMR and AMR can be seen as two sides of a coin and it turns out that concentrating on the SMR-effect has practical benefits. H_D and H_K are the demagnetization field and the uniaxial anisotropy field, respectively, and H_y is the external field, which is the field of interest.

$$V_{\text{out}} = \frac{1}{2} I_0 \Delta R_0 \sin\omega t + \frac{1}{2} \frac{\alpha I_0^2 \Delta R H_y \cos 2\omega t}{(H_D + H_K)^2} - \frac{1}{2} \frac{\alpha I_0^2 \Delta R H_y}{(H_D + H_K)^2} \tag{3.4}$$

The time average of the voltage signal, so the DC-component of V_{out} can be computed from (3.4) and is given as (3.5). This formula shows the direct link between the voltage output, the magnetoresistance and the magnetic field of interest.

$$\overline{V_{\text{out}}} = \frac{\alpha I_0^2 \Delta R}{2(H_D + H_K)^2} H_y \tag{3.5}$$

At this point it is important to mention that this DC-component of V_{out}, which is necessary to measure the magnetic field, can be obtained in two different ways. One way would be to use DC excitation instead of AC excitation. However, the paper (Xu et al., 2018) states clearly that DC excitation makes an initial magnetization 45° off the current direction and therefore off the easy axis necessary. "It is worth noting that, under the AC excitation, it is no longer necessary to bias the magnetization 45° away from the easy axis for output linearization, which greatly simplifies the sensor design." (Xu et al., 2018, p. 4) Since for this thesis no experiments were performed, this experimental issue cannot be confirmed. In simulation, it does not make a difference if DC excitation or AC excitation with subsequent time averaging is exploited. However, it is comprehensible that process fluctuations might have a problematic impact on the experimental procedure when exciting the circuit only with DC current and an initialization as given in Figure 3.21 is necessary to obtain correct results. The second way, which solves this issue in a very efficient way and which is demonstrated as the way to go for this sensor design, is to use AC current and to compute the time average in the sensing procedure by using a standard lock-in technique and extracting the DC signal from the second harmonic. Going further into detail about the experimental extraction of the sensor signal is beyond the scope of the thesis.

The experimental results in the according paper seem very promising. In Figure 3.24 field sweeps from -0.5 Oe forwards to 0.5 Oe and afterwards from 0.5 Oe backwards to -0.5 Oe are performed. The signal curve, which is the time averaged voltage output, is a surprisingly smooth transfer curve, that although performed experimentally seems to be obtained in simulation. The used AC current density amplitude is $5.5 \cdot 10^5$ A/cm^2 ($j_{\text{Pt\_rms}}$ stands for the root mean square amplitude of the current density flowing through the Platinum layer) and the AC frequency is 5000 Hz. The resulting signal output range for the given field sweep is in the order of a few hundreds of μV, which can be measured easily. The linear range of the transfer curve extends from -0.1 Oe to 0.1 Oe, which can be seen in the small frame in Figure 3.24. Although promising, the field measurement also shows the very narrow linear range from -10 μT to 10 μT. If the scope is to achieve good measurement results for such small magnetic fields, this sensor clearly exhibits beneficial properties.

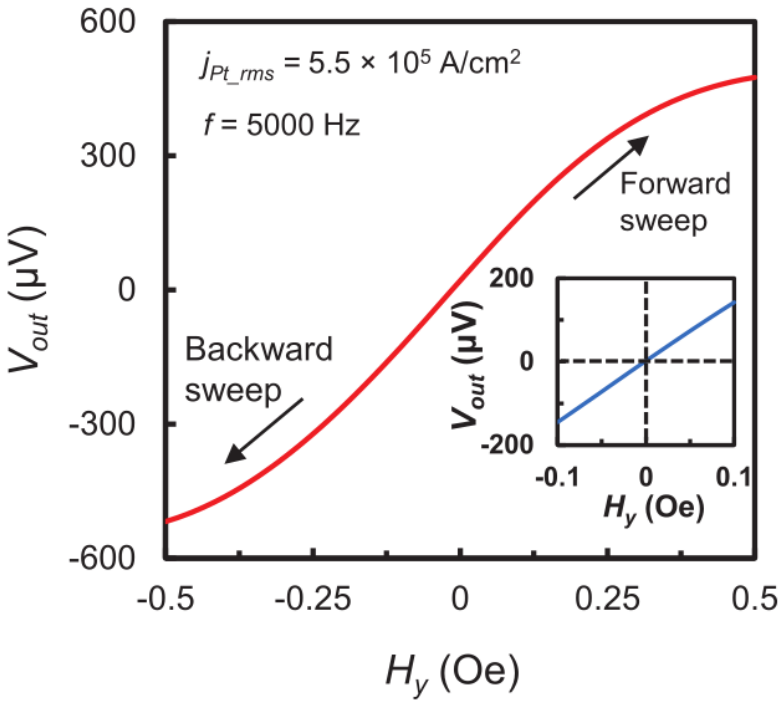

Figure 3.24: Field measurement for a field range between -0.5 Oe to 0.5 Oe (additional magnification for the range between -0.1 Oe and 0.1 Oe). (taken from Xu et al., 2018, p. 7).

An experiment performed in the paper, that shows a strength of this sensor, is visualized in Figure 3.25. An external oscillating magnetic field with an amplitude of 0.1 Oe and an oscillation frequency of 0.1 Hz is applied and the respective sensor signal is examined. Due to the choice of the amplitude being 0.1 Oe the single vector components are always in the linear range between -0.1 Oe and 0.1 Oe, which ensures that the sensor is always working in the given working window. From the visual inspection of the signal curve in Figure 3.25a at the beginning and after 1, 2 and 3 hours of measurement it can be derived that the change of the signal curve properties over time has to be very small. This observation is confirmed in Figure 3.25b, which shows the change of the amplitude and the change of the offset over time. The amplitude and offset change are about 0.2% and 0.3%, respectively, compared to the signal amplitude. This negligible changes emphasize the stability of the presented Wheatstone SMR-sensor over time.

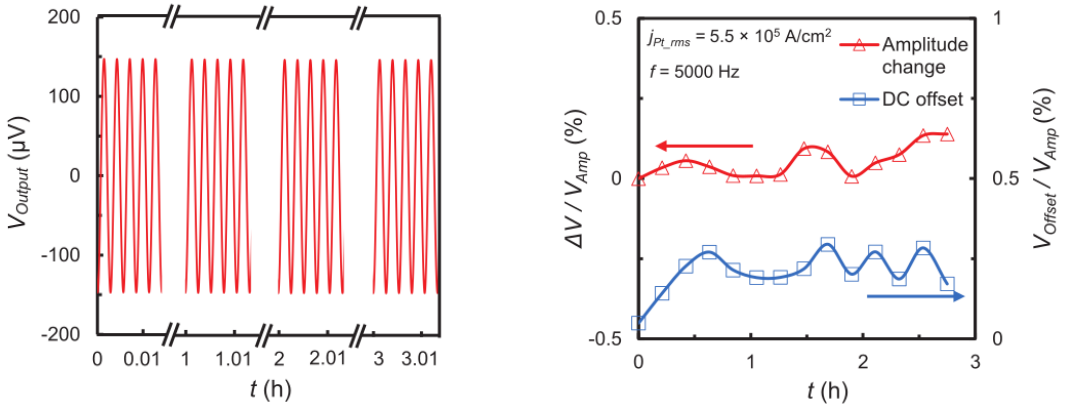

(a) Illustration of the oscillating sensor signal at the beginning and after 1, 2 and 3 hours of measurement.

(b) Amplitude change and change of DC offset during the oscillation measurement.

Figure 3.25: Investigation of sensor signal for an oscillating magnetic field with an amplitude 0.1 Oe and an oscillation frequency of 0.1 Hz. (taken from Xu et al., 2018, p. 7).

There are two contributions to the overall magnetoresistance in the resulting voltage output, the SMR and the AMR. Even though both effects contribute, SMR is dominant, which is why the sensor is referred to as Wheatstone SMR-sensor. This fact can be seen in Figure 3.26. At room temperature the SMR contribution is two times bigger than the AMR contribution. Therefore, the change in magnetoresistance is predominantly determined by the SMR-effect contributing with $2/3$, while only $1/3$ comes from the AMR-effect. This circumstance is even amplified for higher temperatures emphasizing the dominant role of SMR. Since the SMR-contribution nearly does not change for higher temperatures, the sensor is stable to temperature changes.

Another important characteristic of a sensor is the detectivity. Therefore, the detectivity of the Wheatstone SMR-sensor is investigated for the oscillation experiment visualized in Figure 3.25 for different bias current frequencies and for different frequencies of the oscillating magnetic field. The result is illustrated in Figure 3.27. At a frequency of 1 Hz for the oscillating field the sensor with DC bias shows a detectivity of 2.8 $\mathrm{nT}/\sqrt{\mathrm{Hz}}$, whereas it exhibits a detectivity of around 1 $\mathrm{nT}/\sqrt{\mathrm{Hz}}$ for AC bias at all AC frequencies, which shows another benefit of AC excitation. (Xu et al., 2018, p. 8) The detectivity is overall very good and even improves for higher oscillation frequencies as it exhibits small and even decreasing values. The peak for an AC bias at 500 Hz can be explained by bad filtering of the signal and does not represent a weakness of the sensor at this special AC frequency.

A major application for such sensor designs are rotation sensors. Therefore, a rotation measurement and a back and forth sweeping in a small angle range are performed in (Xu et al., 2018) to examine the quality of the Wheatstone SMR-sensor as rotation sensor concerning accuracy and angle resolution. In Figure 3.28 the rotation measurement is illustrated. By comparing the signal curve to the sine fit it can be observed that the sensor works very accurately due to the high accordance between experimental data and fitting curve. To investigate the angular resolution of the sensor the field is swept between 0° and 0.1° back and forth with steps of 0.01°. The angles and the according sensor signals are depicted in Figure 3.29. The experimental curve (red) shows that the angular resolution of the sensor is in the order of 0.01°, which is better than most comparable sensor designs available can do.

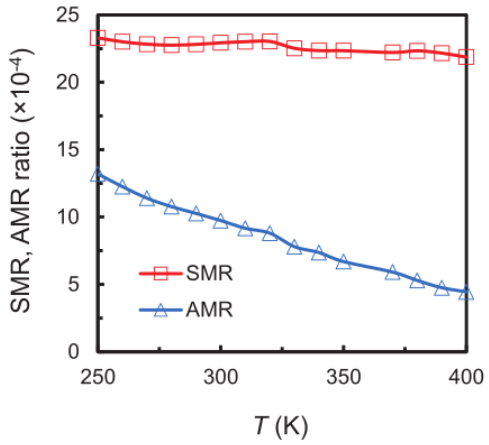

Figure 3.26: Temperature dependency of SMR and AMR contribution. (taken from Xu et al., 2018, p. 7).

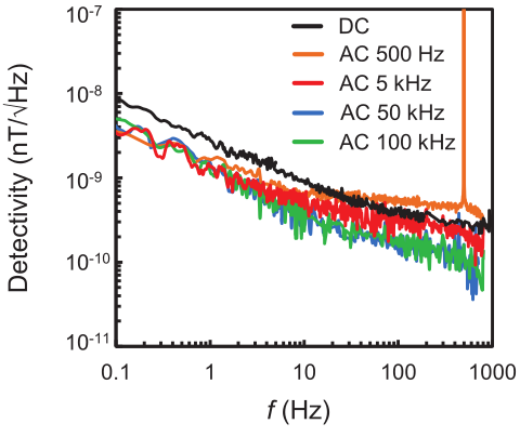

Figure 3.27: Detectivity of the sensor for the oscillation experiment from Figure 3.25 for different current biases and different oscillation frequencies. (taken from Xu et al., 2018, p. 11).

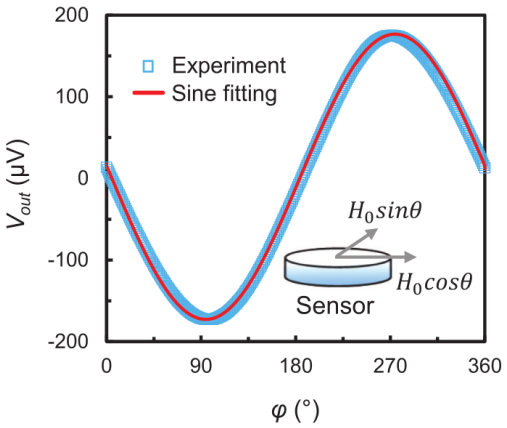

Figure 3.28: Rotation measurement for $H_0 = 0.1$ Oe. (taken from Xu et al., 2018, p. 13).

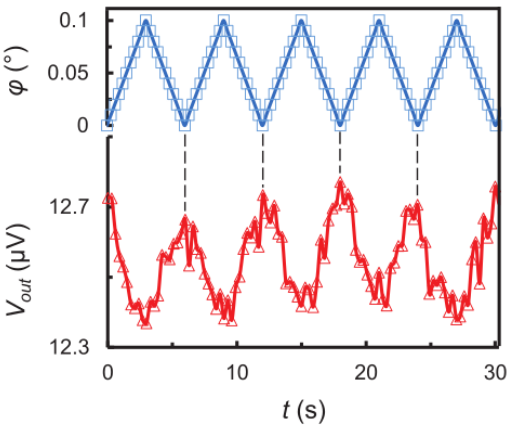

Figure 3.29: Sensor signal for sweeping the field back and forth from $\varphi = 0°$ to $0.1°$ in steps of $0.01°$. (taken from Xu et al., 2018, p. 13).

All of the examination in the paper (Xu et al., 2018) described above seems very promising. Another illustrative proof-of-concept experiment is performed to show the capability of this Wheatstone SMR-sensor. A finger motion sensor is realized using the sensor design, which is illustrated in Figure 3.30. By changing the angle of the finger to the Earth's surface from 90° to 15°, the y-component of the acting external field on the sensor gets more and more equal to the horizontal component of the Earth's magnetic field, which explains the increase in signal magnitude along the experiment. The stepwise change visualizes the accuracy of the sensor. The experiment works since the Earth's magnetic field is in the order of a few μT. However, depending on the location of the experimenter on the Earth, the Earth's magnetic field might already be too high to provide accurate measurement results, since it is typically higher than the 10 μT accurately measurable with the Wheatstone SMR-sensor.

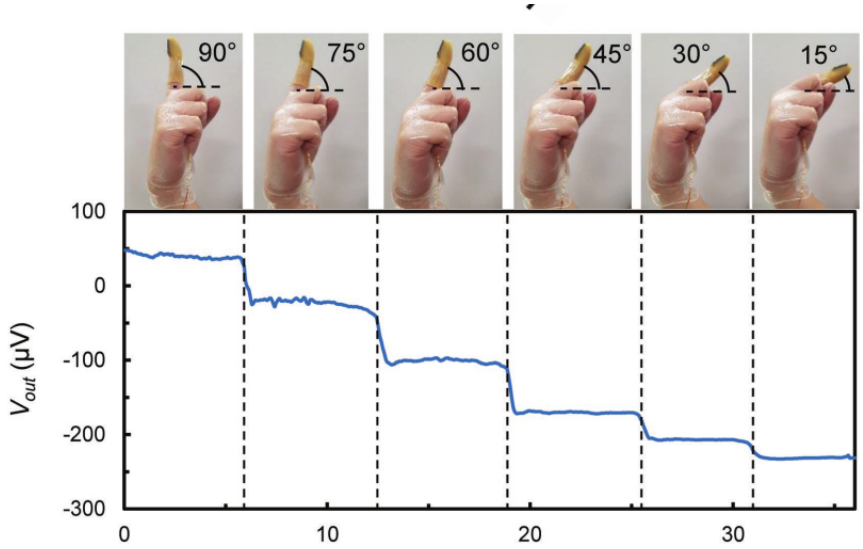

Figure 3.30: Finger motion sensor exploiting the Wheatstone SMR-sensor design. (taken from Xu et al., 2018, p. 18).

As already mentioned and emphasized in the paper, the results from the paper (Xu et al., 2018) discussed above are surprisingly promising, since the sensor exhibits properties as astonishing detectivity, negligible hysteresis and DC offset and better angular resolution than comparable sensors. When listing these characteristics, it is of utmost importance to mention that the Wheatstone SMR-sensor only works for a very narrow field range of a few μT. Higher fields cannot be detected accurately and for practical realizations it might even be necessary to shield the sensor from the Earth's magnetic field, since it might already have a strong impact of the sensing accuracy. Till now, only the experimental examination performed in the paper (Xu et al., 2018) was taken into account. In the following, simulations are performed to investigate the system further. The above mentioned properties should be confirmed and the behaviour at higher fields should be looked at.

3.4 Wheatstone SMR-sensor (simulation results)

The simulation scripts performing single spin simulations look similar to the presented single spin simulation script in Appendix A, just with more sensor elements included in the simulation process. Therefore, presenting a simulation script for the Wheatstone SMR-sensor is renounced.

First of all, a way of obtaining the Wheatstone SMR-sensor signal by single spin simulations has to be elaborated. Therefore, the magnetization components, that contribute to the change in magnetoresistance due to SMR, have to be identified. This is elaborated in the paper (Cho et al., 2015). In this paper, field rotations along different rotation axis relative to the current direction are performed and the resistance signals are measured. The experimental setup to measure the longitudinal resistance along the current direction R_{xx} and the transversal resistance normal to the current direction R_{xy} is a Hall cross. The applied field rotations as well as the resistance signals are illustrated in Figure 3.31.

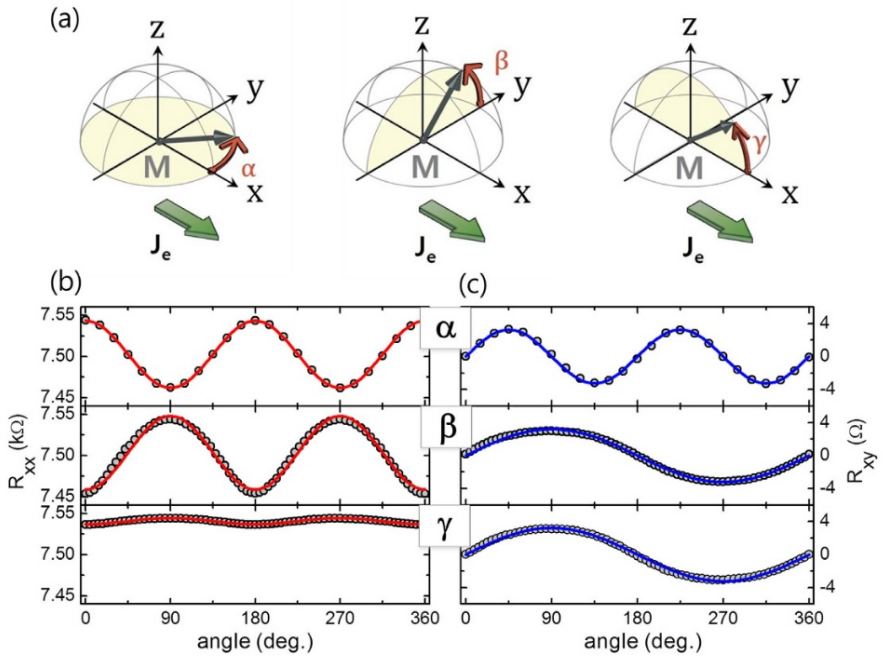

Figure 3.31: Field angular dependency of the magnetoresistance. (a) Schematic of the applied field rotations. (b) Longitudinal resistance R_{xx} (along the current direction). (c) Transversal resistance R_{xy} (normal to the current flow direction). (taken from Cho et al., 2015, p. 3).

The theory behind SMR is further explained in (Chen et al., 2013). There, the longitudinal and transversal resistivities ρ_{xx} and ρ_{xy} are identified (besides some adaptions from (Cho et al., 2015)) as (3.6) and (3.7). Besides ρ as the intrinsic electric resistitvity and $\Delta\rho_0$ as the resistivity without spin-orbit contributions, the important contributions are $\Delta\rho_1$ and $\Delta\rho_2$ as the changes of the longitudinal resistivity due to SMR and AMR effect, which are also the changes of the transversal resistivity due to Planar Hall Effect (PHE) and Anomalous Hall Effect (AHE). According to these formulas the magnetoresistance effects can be assigned to the different signals in Figure 3.31, since for different rotation axes different magnetization components change.

$$\rho_{xx} = \rho + \Delta\rho_0 + \Delta\rho_1(1 - m_y^2) + \Delta\rho_2 m_x^2 \tag{3.6}$$

$$\rho_{xy} = \Delta\rho_1 m_x m_y + \Delta\rho_2 m_z \tag{3.7}$$

However, the important thing to note is that the SMR-effect is proportional to m_y^2. Therefore, in the simulation the y-component of the magnetization vector can be exploited to obtain a measure of the sensor signal. As already mentioned, for simulation purposes it does not make a difference, if AC or DC current is used since no process fluctuations appear and the upper and lower branch of the Wheatstone bridge are equal. On account of simplicity, DC current is assumed. A simplified illustration of the sensor with the sensor elements used for the simulation is plotted in Figure 3.32.
To obtain the corresponding sensor signal, the magnetization of the two elements is simulated and the y-components are taken to mimic the SMR-effect. The logic, that is also illustrated in Formula (3.8), is the following: When using DC current, the experimental signal, i. e. the DC-voltage output, is given as the product of the current strength I times the resistance due to SMR. This resistance is zero for the initial state, when no

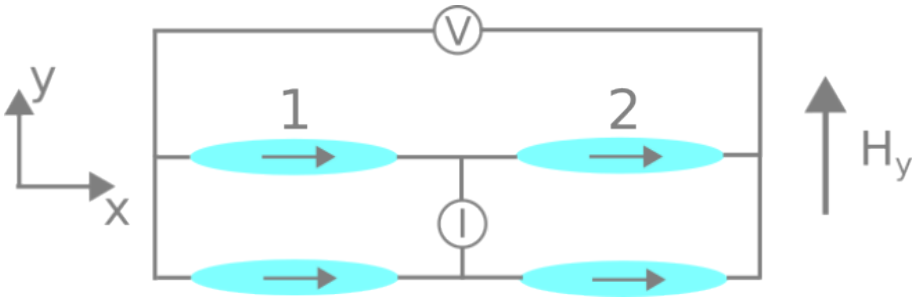

Figure 3.32: Simple illustration of the Wheatstone SMR-sensor with the elements used in the simulation.

external field is applied. I is obviously proportional to the current density j_e since the cross-sections of the elements do not change in time. Both elements 1 and 2 contribute to the magnetoresistance and they do so in opposing manner. That is because the current direction in element 1 is the opposite compared to the current direction in element 2. Due to this circumstance and the proportionality of the resistance to the squared y-component of the magnetization in each element, the resistance signal is given as $R_{\text{SMR}} \propto (m_{y,1}^2 - m_{y,2}^2)$. All in all, a direct link between the experimental signal and the simulation signal is established enabling the simulation of the Wheatstone SMR-sensor.

$$\text{Experimental signal} = \overline{V_{\text{out}}} = I \cdot R_{\text{SMR}} \propto (m_{y,1}^2 - m_{y,2}^2) \cdot j_e = \text{Simulation signal} \quad (3.8)$$

In the following, some sensor properties are examined by means of numerical simulations. For all the simulations, the following parameters are fixed: $\eta_{\text{damp}} = 0.1$, $\eta_{\text{field}} = 0.1$, saturation magnetization $\mu_0 M_s = 0.5T$ and thickness of the free magnetic layer $d = 2$ nm. These parameters do not represent the original parameters for the used materials in the experiment, since the exact values for η_{damp} and η_{field} of the given Pt/NiFe-bilayer is not given. For thickness and saturation magnetization, the nearly exact value and a typical value for the saturation magnetization are used, respectively. While this means that the exact signal curves are not reproduced exactly, which is not the scope of numerical simulations of magnetic sensors, some main sensor characteristics still can be extracted.

3.4.1 Application of Wheatstone SMR-sensor as field sensor

First of all, the experimentally obtained astonishingly smooth transfer curve in Figure 3.24 should be reproduced in simulation. Therefore, a field sweep from -0.5 Oe to 0.5 Oe (so from -50 μT to 50 μT) is performed in a single spin simulation. A shape anisotropy of 0.12 mT due to the elliptical shape is assumed as effective anisotropy field and a current density of $5.5{\cdot}10^9$ A/m^2 ($= 5.5{\cdot}10^5$ A/cm^2) is taken into account. The initial magnetization is set into x-direction for all sensor elements. The result is the transfer curve in Figure 3.33. The y-axis is showing the signal with respect to a maximal signal strength in the subsequent image. This, however, does not change the characteristics of the signal curve since the experimental signal and simulation signal are just equal up to an unknown proportionality factor, which does not affect the shape of the curve. The sensor curve is indeed smooth and has a linear range between -10 μT to 10 μT. The very small curvature might come from an inadequate choice of the SOT-parameters. However, the experimentally obtained signal curve can be confirmed.

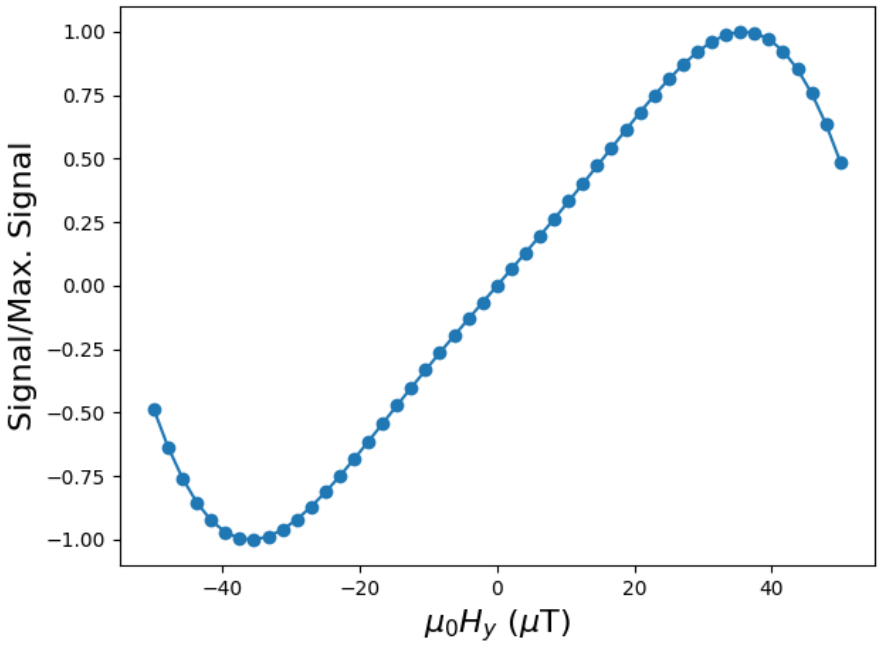

Figure 3.33: Simulated field sweep in the field range between -50 μT and 50 μT.

Another interesting examination of the system can be done by varying the current density used in the sensor. This is done in Figure 3.34, which shows the signal curves for a wider field range between -100 μT and 100 μT. The enormous dependence of the signal curve properties on the current density is surprising. Note that a current reversal does not change the sign of the slope since the branches of the Wheatstone bridge are symmetric. However, varying the current density changes the linear range and also the sign of the slope in this potential working window of the sensor. For example, raising j_e from 5.5 $\cdot 10^9$ A/m^2 to 1 $\cdot 10^{10}$ A/m^2 increases the linear range, but changes the sign of the transfer curve slope to negative. For 2 $\cdot 10^{10}$ A/m^2 an even higher linear range with positive slope is obtained. Further increases in the current density lead partially to higher linear ranges with negative slope until at a current density of 1 $\cdot 10^{11}$ A/m^2 the transfer curve collapses. This might be due to the high current flow in the small sensor elements. At $j_e = 1 \cdot 10^{11}$ A/m^2 the current flowing through the sensor elements is at least 40 mA at the largest extent of the elements. This might be already critical for the tiny elliptical sensor elements.

Some current densities seem to be beneficial exhibiting a wider linear range. To examine this further, the current densities 3 $\cdot 10^{10}$ A/m^2, 4 $\cdot 10^{10}$ A/m^2 and 5 $\cdot 10^{10}$ A/m^2 are chosen for a field sweep in a wider field range. The result is illustrated in Figure 3.35. A good choice of the current density leads to a better linear range, which however does not extend significantly over a few tens of μT.

The major scope of the simulation part for the Wheatstone SMR-sensor is to establish higher linear ranges and therefore to increase the working window of the sensor, besides looking at the corresponding properties. An obvious way of increasing the linear range is to reduce the ability of the magnetization vector to tilt away from the easy axis. This scope can be achieved by introducing an additional uniaxial anisotropy with easy axis along the current direction or by establishing a so called exchange bias. Additional

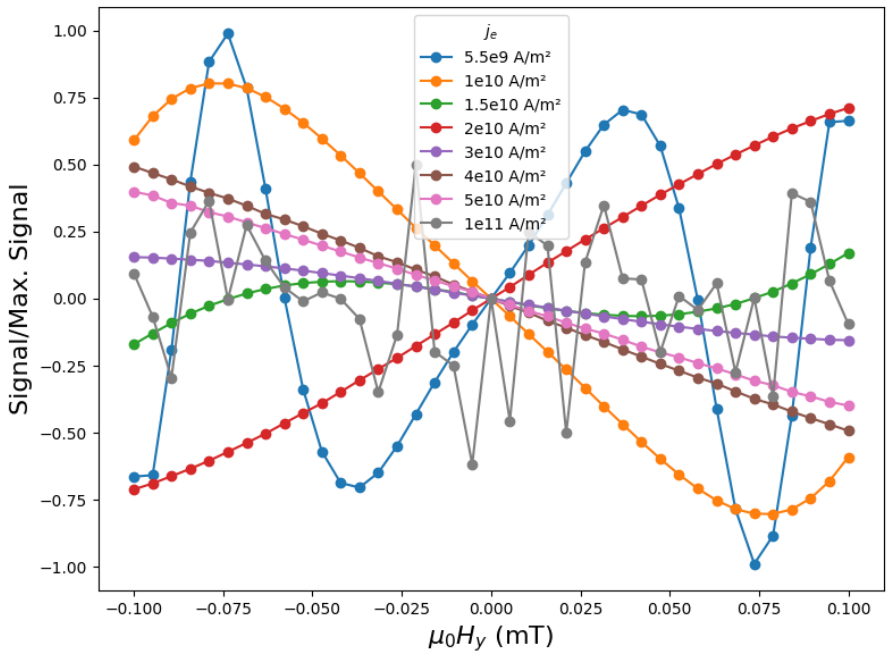

Figure 3.34: Simulated field sweep in the field range between -100 μT and 100 μT for different current densities.

anisotropy is already discussed above for the single sensor elements and can be obtained by using a more elliptical shape, by applying a field during depositional growth or by using a single-crystal substrate. Exchange bias can be seen as a bias field applied during sensing and is further described in the paper (Lim et al., 2022). To illustrate the improvement due to these adjustments, simulations are performed with a shape anisotropy field of 10 mT as effective anisotropy field and different exchange bias fields. An anisotropy field of 10 mT is high, but the same effect can be achieved by using higher exchange biases. The current density is set to $j_e = 5 \cdot 10^9$ A/m^2. Figure 3.36 is obtained by these simulations. In Figure 3.36a no exchange bias is established, whereas in Figure 3.36b an exchange bias field of 10 mT is applied as an additional external field.

It can be seen that this method is able to increase the linear range. Already without exchange bias, a stronger shape/additional anisotropy leads to an improvement of the operation margin compared to the result illustrated in Figure 3.33, where a small shape anisotropy of 0.12 mT is considered. An additional exchange bias enlarges the linear range even further. However, it has to be taken into account, that the signal strength itself also decreases when making the tilting of the magnetization vector smaller. This might be a problem in the practical signal measurement, even though the measurement of tiny voltages is not a big experimental obstacle.

Another important aspect of why to establish some sort of bias field in one direction is the initialization of the sensor. Without such a constraint, an anisotropy along the x-axis could lead to an initial magnetization in positive or negative x-direction. This could, in the worst case, lead to the initial configuration visualized in Figure 3.37. There are other possible initial configurations, but the shown configuration leads to the same magnetization outcomes in both sensor elements of the upper and the lower branch, which causes the cancellation of the overall signal output. This is illustrated in the simulated transfer curve in Figure 3.38, where the mentioned initial magnetization is assumed.

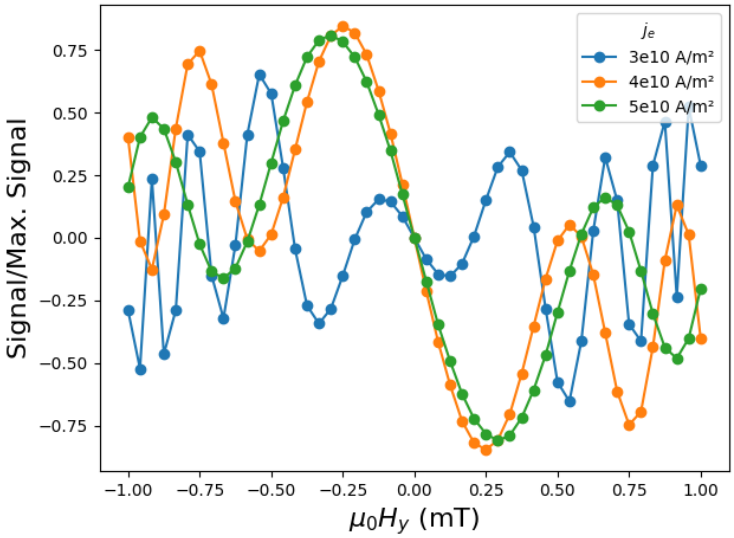

Figure 3.35: Simulated field sweep in the field range between -1 mT and 1 mT for 3 specific current densities.

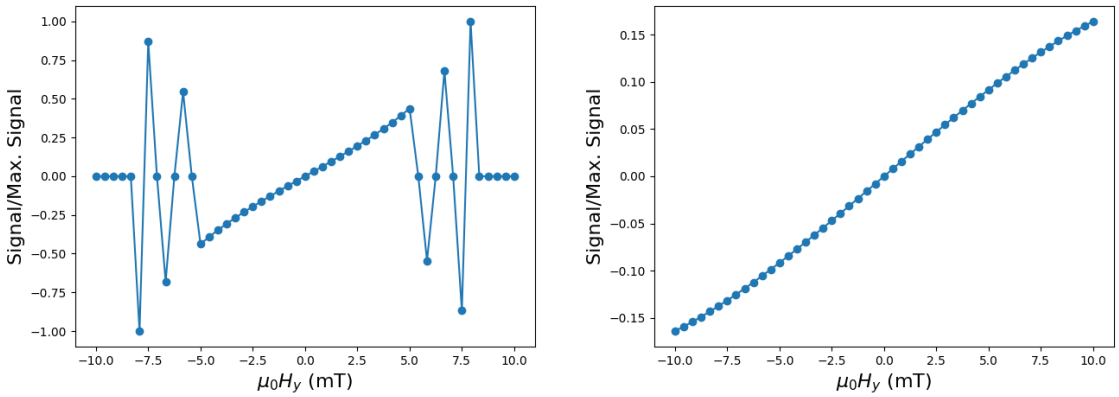

(a) Signal curve for no exchange bias field and a shape/additional anisotropy field of 10 mT.

(b) Signal curve for an exchange bias field of 10 mT and a shape/additional anisotropy field of 10 mT.

Figure 3.36: Influence of reducing the tilting ability of the magnetization vector on sensor signal.

The Wheatstone SMR-sensor is sensitive to magnetic fields in y-direction. An important examination of the sensor principle is to apply x-fields as disturbing fields. The results of this observation have also a huge impact on the potential performance of the sensor as rotational sensor. Positive x-fields act into the same direction as constraining bias fields. Therefore, they should have a positive impact on the linear range of the transfer curve with a resulting reduction in the signal strength as already pointed out. This can be confirmed with the simulated transfer curves shown in Figure 3.39, where different x-fields from 0 mT to 1 mT are assumed. The used current density is $j_e = 5 \cdot 10^9$ A/m^2 and a shape anisotropy of 10 mT is assumed to achieve wider linear ranges. The overall strength decreases for higher magnetic fields in the positive x-direction. This trend continues also for higher fields as shown in Figure 3.36, which can be explained theoretically, since higher fields in positive x-direction reduce the tilting of the magnetization vector further and further.

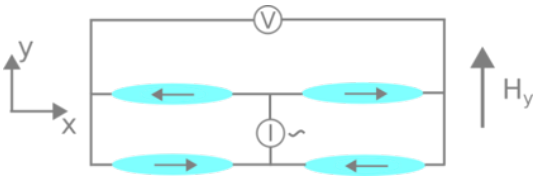

Figure 3.37: Visualization of the Wheatstone SMR-sensor with wrong initialization caused potentially by missing bias field constraint.

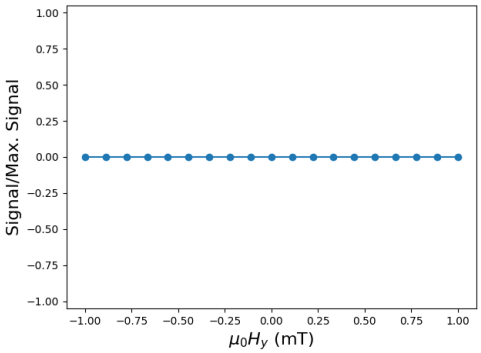

Figure 3.38: Sensor signal with the initial magnetization given in Figure 3.37.

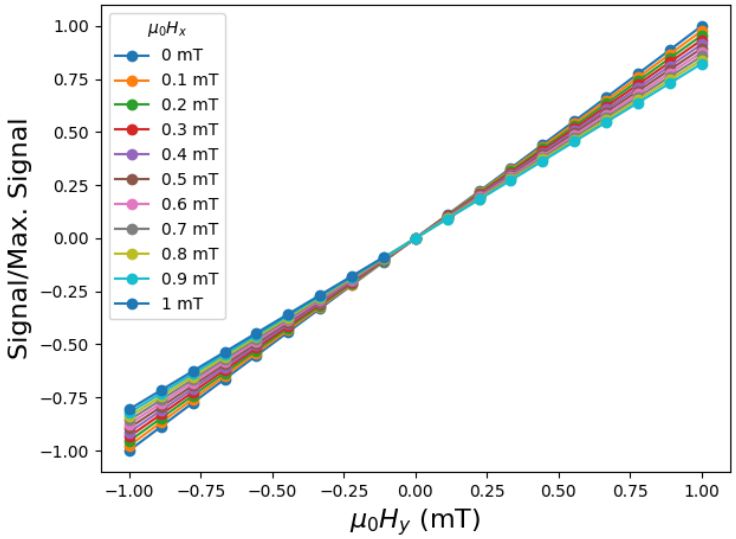

Figure 3.39: Sensor signal for disturbing fields in the positive x-direction.

The examination of disturbing fields in negative x-direction is more interesting. Such constraining fields lead to a higher signal strength, since the tilting of the magnetization vector is benefited. The same simulation as before is now performed in Figure 3.40 for different fields in negative x-direction ranging from 0 mT to 1 mT (Figure 3.40a) and also for distinct field strengths ranging from 0 mT to 3 mT (Figure 3.40b). For small disturbing fields in the negative x-direction the overall signal strength is slightly increased. However, for higher fields fluctuations appear and the linear range is reduced strongly. Especially the behaviour with magnetic fields in negative x-direction, but also the change in signal strength for x-fields in general might cause severe problems when using the sensor to measure rotations.

3.4.2 Application of Wheatstone SMR-sensor as rotation sensor

In Figure 3.28, the sensor principle is used for rotation sensing. It is important to note, that the rotating field has a strength of $H_0 = 0.1$ Oe, which is $\mu_0 H_0 = 10\ \mu$T, which is very small. Even for such a small magnetic field, it might be seen in the mentioned illustration of the sensor signal, that the signal curve deviates slightly from the sine

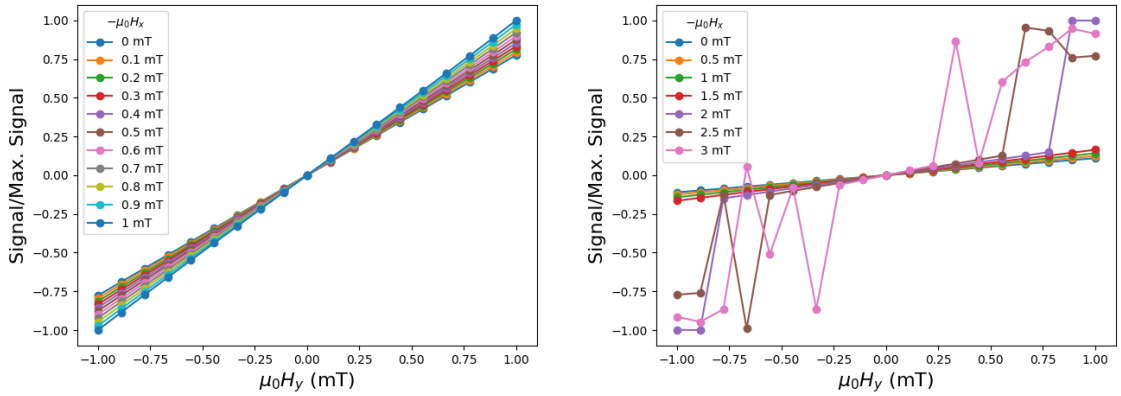

(a) Sensor signal for disturbing fields in the negative x-direction ranging from 0 mT to 1 mT.

(b) Sensor signal for disturbing fields in the negative x-direction ranging from 0 mT to 3 mT.

Figure 3.40: Sensor signal for disturbing fields in the negative x-direction.

curve at the minimum and maximum at 90° and 270°. To examine the potential of the sensor principle for rotation sensing, a higher shape anisotropy of each sensor element is assumed to increase the linear range of the field sensor. It is set to 10 mT and the current density is chosen to be $j_e = 5 \cdot 10^9$ A/m^2. First, a rotating magnetic field with $\mu_0 H_0 = 10$ μT is applied. This leads to the signal curve in Figure 3.41. The curve seems to be quite good and close to the sine curve. The opposite course of the curve compared to the curve presented in the paper has no physical meaning, since the signal curves in simulation and experiment are just proportional to each other.

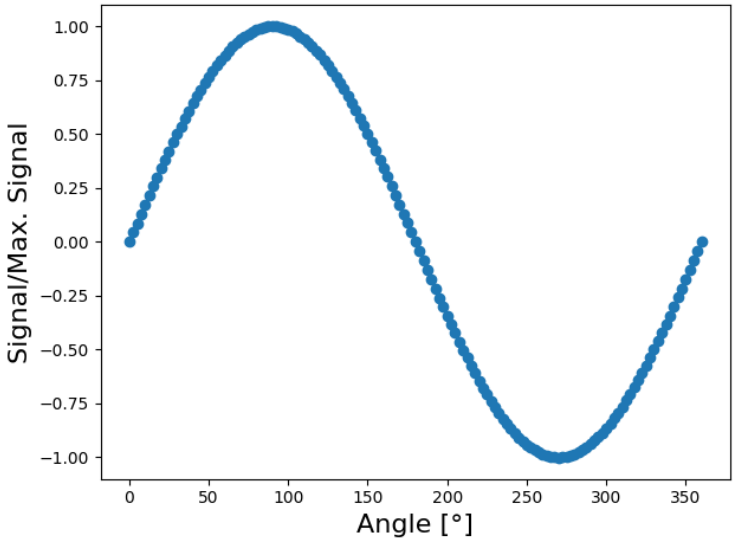

Figure 3.41: Sensor signal for rotating field of $\mu_0 H_0 = 10$ μT.

Problems appear, if higher magnetic fields are chosen to rotate. This is visualized in Figure 3.42. In Figure 3.42a a magnetic field with $\mu_0 H_0 = 0.1$ mT is chosen, whereas in Figure 3.42b a magnetic field with $\mu_0 H_0 = 1.8$ mT is applied. Due to the severe problems with negative x-fields the maximum and the minimum of the curve are shifted together when increasing the rotating field.

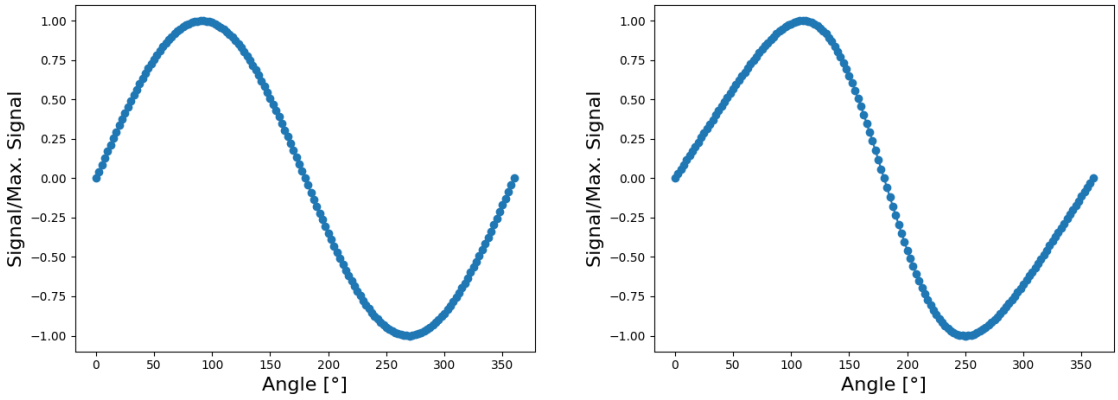

(a) Sensor signal for rotating field of $\mu_0 H_0 = 0.1$ mT.

(b) Sensor signal for rotating field of $\mu_0 H_0 = 1.8$ mT.

Figure 3.42: Sensor signal for rotating fields with higher strengths.

To illustrate this further, the shift of the maximum in the signal curves of the rotation sensing is examined for increasing magnitude of the rotating field. Therefore, different field strengths between 0.1 mT and 1.8 mT are applied in the rotation simulation and the shift of the angle, at which the maximum appears, is visualized in Figure 3.43. It can be seen clearly that the angle of the maximum increases linearly with increasing field strength and the shift is tremendous. For the sensor to work properly as rotation sensor the angle of the maximum should be 90° and already for a field strength of 1 mT the displacement of the maximum amounts to more than 10°. If the curve in Figure 3.43 is prolonged, the conclusion can be drawn that flawless rotation sensing is only possible in the limit of zero rotating field, which however would not deliver any signal. Already for tiny rotating fields an error occurs, which might be insignificant to some extent.

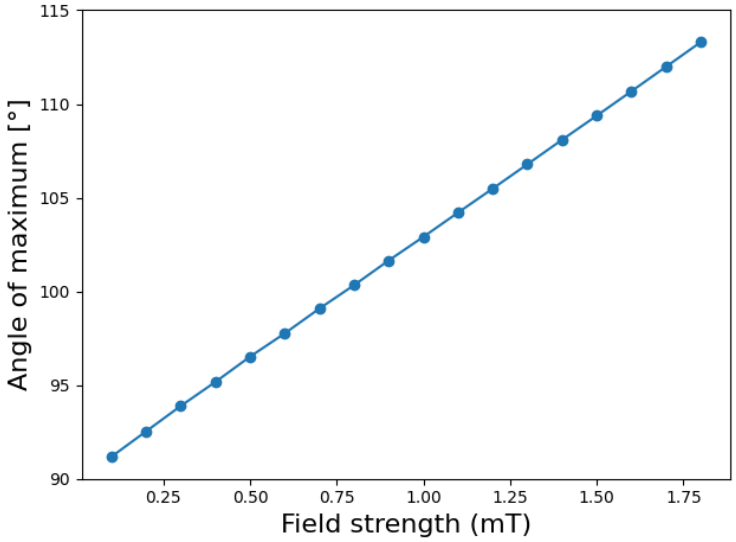

Figure 3.43: Shift of angle of signal maximum in rotation measurement for increasing strength of rotating field.

In the following, the potential of the Wheatstone SMR-sensor for rotation sensing should be examined. The simplest possible realization of a rotation sensor with this sensor principle are two Wheatstone SMR-sensors rotated 90° to each other as depicted in Figure 3.44. The reason for this necessity is that the sine curve is not an injective imaging, meaning that two distinct angle values can be projected onto one and the same signal output. This leads to an indeterminacy in the sensing procedure, which can be eliminated by measuring the signal outputs of two sensor elements arranged in the illustrated manner. The signal curves of the two sensor elements are a sine curve and a cosine curve. By dividing the signal of the left sensor in Figure 3.44 by the signal of the right one and applying the arctangent to this value, the rotation angle can be extracted and therefore sensed unambiguously. This works only flawlessly, if the signal curves are ideal sine and cosine curves.

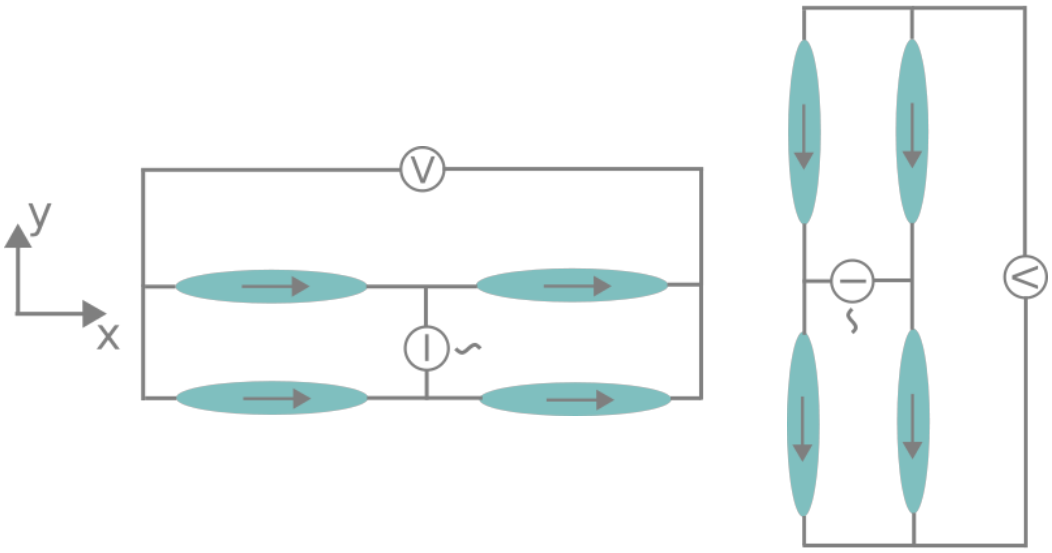

Figure 3.44: Realization of a rotation sensor using two Wheatstone SMR-sensors rotated 90° to each other.

With the above concept the rotation sensing procedure can be simulated. First, a rotating magnetic field with a small magnitude of $\mu_0 H_0 = 10\ \mu$T is assumed. In Figure 3.45, the corresponding two signal curves are drawn. Moreover, the angle is extracted from the two sensor signals and the deviation of this calculation from the actual angle is illustrated. Although small, the worst detection error amounts to nearly 0.1°. If this error is acceptable for practical use, the sensor principle is capable of rotation sensing in the case of very small rotating magnetic fields.

Due to the deformation of the signal curve for higher rotating fields, the rotation sensing becomes more and more inaccurate when increasing the strength of the rotating field. In Figure 3.46a and 3.46b the rotation sensing procedure is simulated as before for field magnitudes of 0.1 mT and 1 mT, respectively. The shift of the maximum and minimum toward each other leads to a more and more inaccurate angle detection for increasing field strengths. For a magnetic field of 1 mT the worst sensing error amounts already to nearly 10°, which is obviously unacceptable for any field of use.

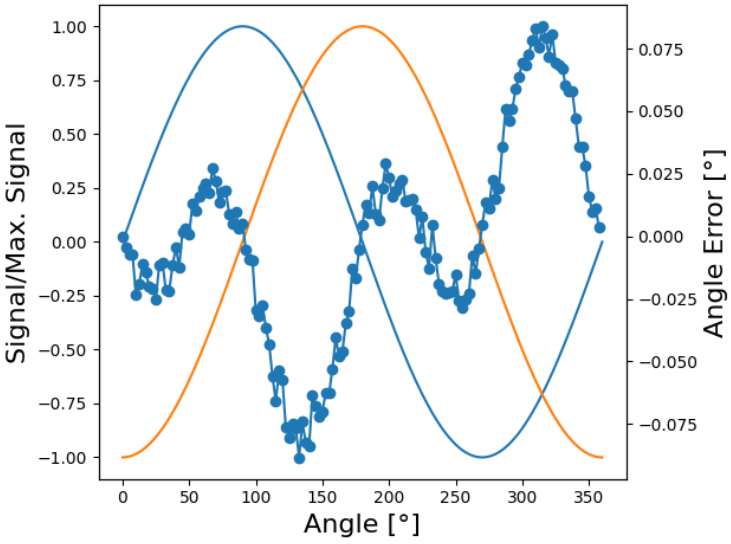

Figure 3.45: Sensing error for a rotating field with a magnitude of $\mu_0 H_0 = 10$ μT.

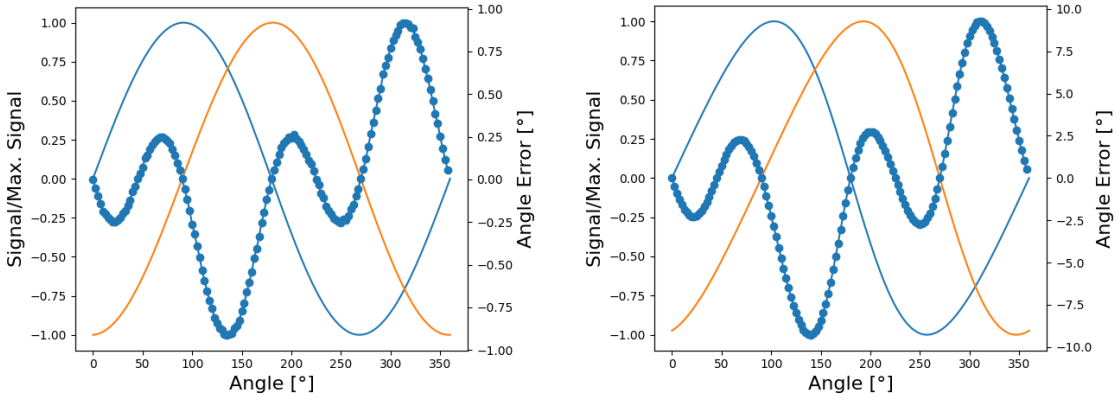

(a) Sensing error for a rotating field with a magnitude of $\mu_0 H_0 = 0.1$ mT.

(b) Sensing error for a rotating field with a magnitude of $\mu_0 H_0 = 1$ mT.

Figure 3.46: Sensing error for rotating fields with higher magnitudes.

All in all, the Wheatstone SMR-sensor is not capable of flawless rotation sensing for any field strength. However, if small, but not negligible, detection errors are acceptable, the sensor principle can be used combined with small field strengths and an adequate shielding. It has to be taken into account, that a rotating magnetic field of $\mu_0 H_0 = 10$ μT is superposed considerably by the Earth's magnetic field, which hampers rotation sensing substantially.

Chapter 4

Hall cross sensors exploiting Spin Orbit Torque

The Hall cross design plays a crucial role in magnetic field measurements. The classical Hall effect enables field sensing in bigger dimensions and the respective Hall sensor is one of the most widely used sensor concepts. Instead of the well-known Hall effect, the SOT effect should be exploited in the following to show potential field sensing possibilities. There are different approaches to such a sensor concept. In the paper by Li et al. (Li et al., 2021) an SOT-device is presented, that is able to sense magnetic fields in all three dimensions. The concept is based on the movement of a DW due to the SOT-current and the external magnetic field. An analytical description of Hall cross SOT-devices based on DW-motion is given in the paper (Schulz et al., 2017). In the following chapter, a different concept should be examined that uses a multidomain SOT-device.

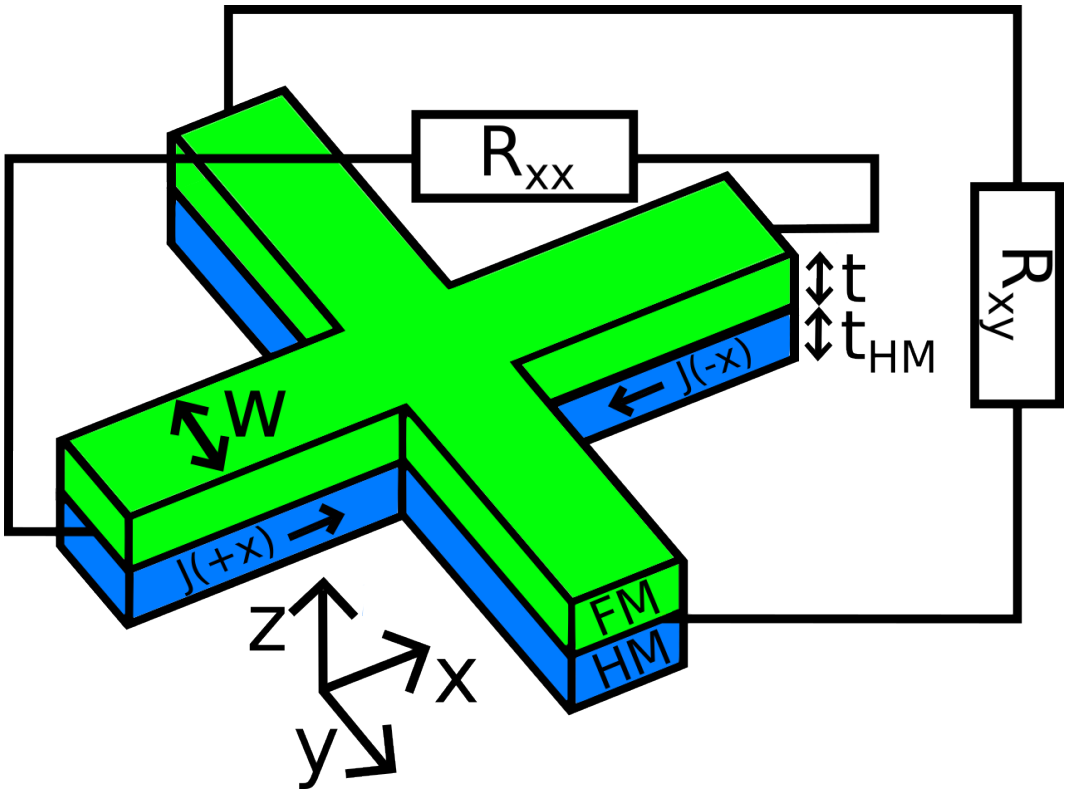

Figure 4.1: Schematic illustration of the Hall cross structure.

In Figure 4.1 the schematic illustration of the used Hall cross design is depicted. The relevant part of the sensor consists of a heavy metal (HM) layer with thickness t_{HM} and a ferromagnetic (FM) layer with thickness t. In addition, an oxide as insulator is added on top of the FM layer. As HM tantalum is used with a thickness of $t_{\mathsf{HM}} = 6$ nm. CoFeB is used as FM with a thickness of $t = 0.92$ nm. The width of the Hall cross is assumed to be $w = 2$ nm and the length of the crossing arms is set to 10 nm. The SOT-current is flowing in x-direction through the sensor in positive or negative direction, but the flow is illustrated in the HM layer since the current flow through the heavy metal is causing the SOT-effect and the current flow through the FM layer should have a negligible effect.

The necessary resistances used for field evaluation R_{xx} and R_{xy} are also visualized in the schematic figure. As already mentioned in the context of Figure 3.31 these resistances depend on the magnetization vector according to equations (3.6) and (3.7). For the resistance along the current direction R_{xx} the SMR-effect ($\propto m_y^2$) and the AMR-effect ($\propto m_x^2$) are relevant, whereas for the transversal resistance R_{xy} the PHE ($\propto m_x \cdot m_y$) and the AHE ($\propto m_z$) are the determining factors. By measuring the resistances in combination with an appropriate sensing principle, magnetic field sensing can be enabled.

The assumed sensor is based on the patented sensor concept (Suess et al., 2021). A Hall cross sensor is used which breaks up into a multidomain state. This means that the Hall cross consists of many magnetic domains that point out-of-plane either in positive or negative z-direction with DWs in between. The starting point for field measurements is illustrated in Figure 4.2 with red regions being magnetic domains with magnetization pointing in positive z-direction and blue regions being magnetic domains with magnetization pointing in negative z-direction. This state corresponds to zero SOT-current. For most simulations only the resistance along the current direction R_{xx} with the slightly greyed out area is computed, since the behaviour of the magnetization leading to the desired signal can be fully observed in the respective area. In the simulation, the magnetization components are computed in contrast to the experiment, where only the resistances are available.

The grey area outside of the Hall cross sensor is set to be non-magnetic in the simulation. The vector of the magnetic field to be measured is located in the plane of the Hall cross and it turns out, that the sensor principle is sensitive to the x-component of the magnetic field. By choosing the experimental setup wisely and being able to change the current direction and the arm of the Hall cross pervaded by the current flow, it is possible to determine both components of an inplane magnetic field. Furthermore by combining the signals appropriately and using additional sensing concepts (especially by using an additional TMR-junction in the middle of the Hall cross), the multidomain Hall cross sensor might be used as three dimensional magnetic field sensor. The scope of this chapter is not to prove this potential application, but to investigate the ability of the sensor to sense the magnetic field component along the current direction. Therefore, the setup in Figure 4.2 is exploited with only one current direction.

For the following simulations (if not further specified), a saturation magnetization of $J_s = \mu_0 M_s = 0.75$ T, an exchange constant of $A = 9.2 \cdot 10^{-12}$ J/m, a Gilbert damping parameter of $\alpha = 1$ and an uniaxial anisotropy constant of $K = 0.24$ MJ/m^3 are assumed. These are adequate values for the stack Ta(6 nm)/CoFeB(0.92 nm)/MgO(2 nm). For the current density, different values are chosen for examination. The most com-

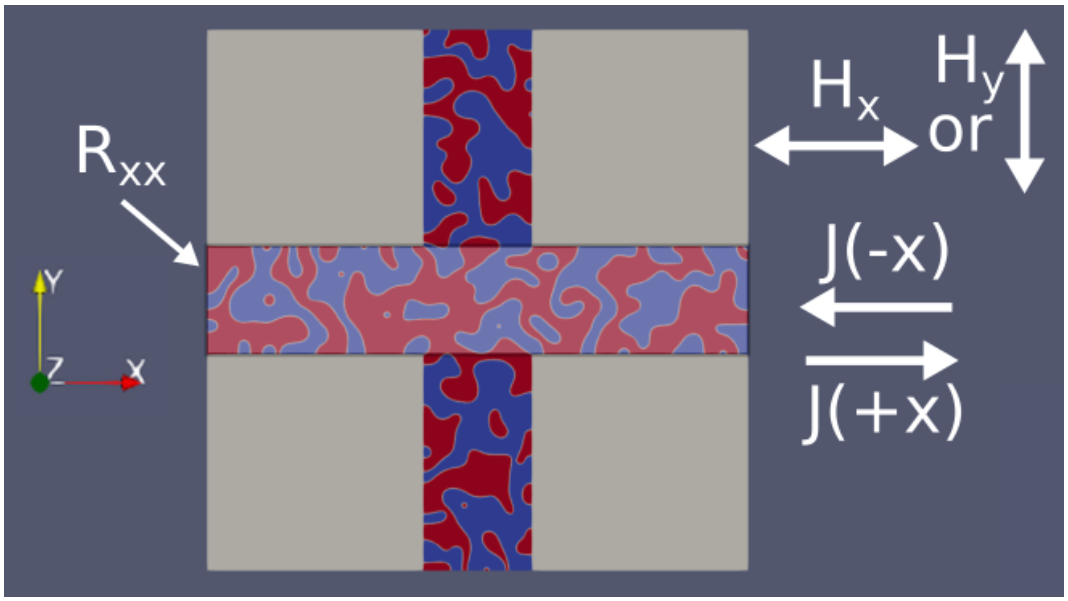

Figure 4.2: Multidomain state of the used sensor principle.

plicated part in choosing appropriate simulation parameters is finding adequate values for the SOT-efficiency parameters η_{damp} and η_{field}. These are phenomenological parameters, that have to be determined experimentally by already mentioned means (e.g. Hayashi method (Hayashi et al., 2014) or Dutta method (Dutta et al., 2021)). This determination can be quite cumbersome and general values for the given sensor stack are hard to find in literature. In the scientific project this thesis aims to contribute to, the values are first assumed to be $\eta_{\text{damp}} = -0.1451$ and $\eta_{\text{field}} = -0.0276$. Throughout the project the used parameters change to $\eta_{\text{damp}} = 0.09$ and $\eta_{\text{field}} = -0.17$, which changes the sign of the transfer curve. The used torque parameters are specified in the following sections. Since the scope of the simulations is to give qualitative insights into the system with some non-realistic assumptions and not to exactly compute experimental results, the exact values for these parameters do not play a major role in the following observation.

The field sweeps are simulated by starting from a random initial magnetization state, that relaxes into the final state due to the corresponding external applied field and due to the other contributions stated in the introductory part of this thesis, especially due to the SOT. The choice of an adequate relaxation time is important to achieve proper results, which is also discussed in the following.

4.1 Application of different current densities

In this part the torque parameters are $\eta_{\text{damp}} = -0.1451$ and $\eta_{\text{field}} = -0.0276$. The impact of the current magnitude should be examined by applying first a current density huge enough for appropriate field sensing and then comparing this to the behaviour of the sensor for small current densities. Afterwards, the performance of the sensor with different current strengths in the higher regime should be investigated.

A potential current density enabling field sensing and exploited in the experimental part of the underlying scientific project is $J_e = 2.4 \cdot 10^{11}$ A/m^2, which results from an applied current magnitude of $I = 3.351$ mA. A simulated field sweep in x-direction from -10 mT to 10 mT leads to the behaviour of the magnetic domains shown in Figure 4.3. For higher field magnitudes, the SOT-current drives out the different domains according to current and field direction, such that the entire arm flooded by the current is magnetized either in $+$z- (red) or in $-$z-direction (blue). The lower the field magnitude, the more different domains appear in this arm with a maximum of present domains at zero magnetic field. It is evident from looking onto the transversal arm of the Hall cross, that the z-magnetization and the according domain sizes are similar for all field strengths, if no current is flowing.

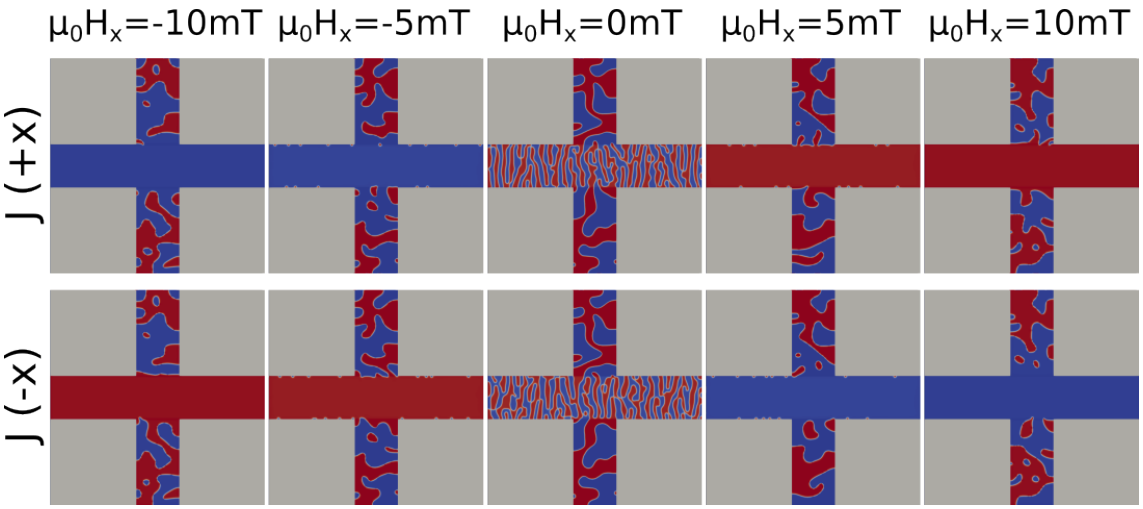

Figure 4.3: Field sweep for a current density of $J_e = 2.4 \cdot 10^{11}$ A/m^2 flowing in positive and negative x-direction.

The sensing principle is based on the AHE, which is proportional to the z-component of the magnetization. In the simulation, this is directly available. The behavior of the z-magnetization in the longitudinal arm for the different current directions is illustrated in Figure 4.4. Combining the different magnetization behaviours by subtracting the two curves leads to the sensor signal curve. The potential transfer curve as the linear part of the signal ranges approximately from -2 mT to 2 mT.

Furthermore, the AMR and SMR signal curves might be interesting to examine. Since these effects are proportional to m_x^2 and m_y^2, respectively, the corresponding signal curves should behave as in Figure 4.5. In the linear range of the transfer curve the two signal curves exhibit opposing parabolic behaviour, which gives rise to the already mentioned fact that AMR- and SMR-effect are just two sides of one coin. This can be also seen from the following representation of the resistance change $\Delta R_{xx,\text{AMR,SMR}}$ due to AMR and SMR in the longitudinal arm, where ΔR_{AMR} and ΔR_{SMR} are the respective contributions of the two effects, $\mathbf{m}$ is the unit magnetization vector and σ is the polarization vector:

$$\Delta R_{xx,\text{AMR,SMR}} = (\Delta R_{\text{AMR}} + \Delta R_{\text{SMR}})(\mathbf{m} \cdot \sigma)^2$$

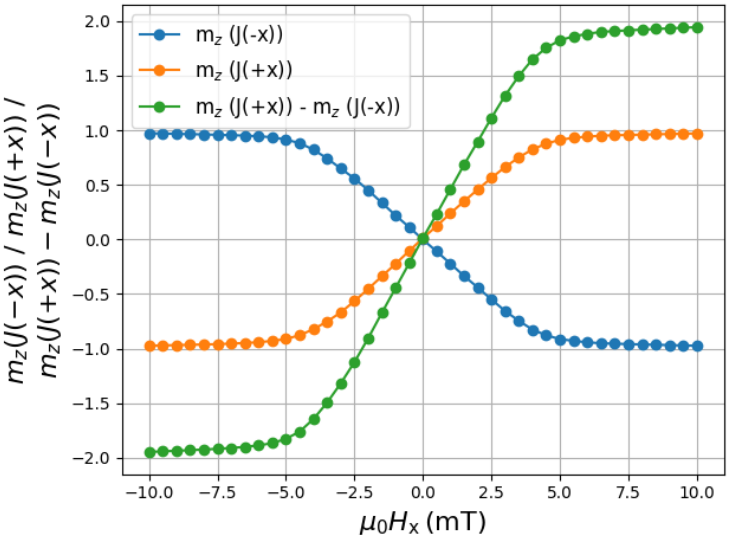

Figure 4.4: Z-Component of the magnetization as a function of external field and transfer curve for the current $I = 3.351$ mA.

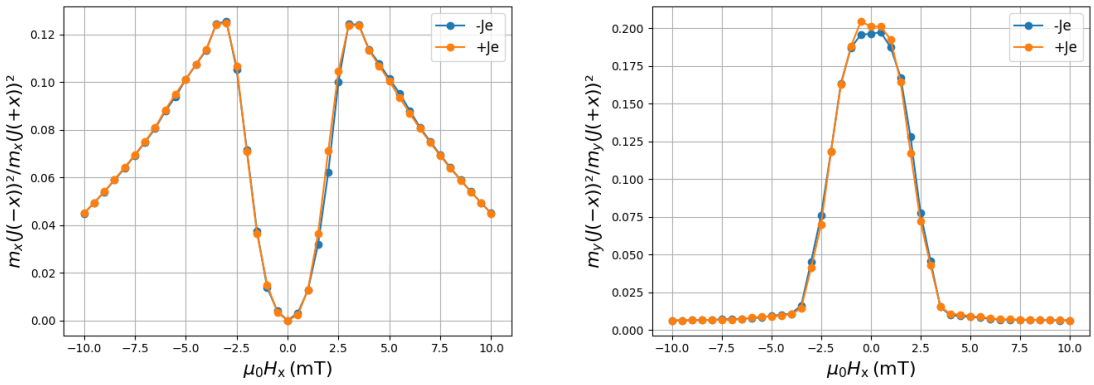

(a) AMR signal curve.

(b) SMR signal curve.

Figure 4.5: AMR and SMR signal curves for the different current directions for $I = 3.351$ mT.

Besides looking at big current densities enabling field measurement, it is also important to examine small current densities and the corresponding behaviour. For example, if the resistance in the transversal arm has to be measured, a small current is applied through this arm and the impact on the magnetic domains is relevant. Therefore, a field sweep with a current density of $J_e = 7.2 \cdot 10^9$ A/m^2 is performed, which would result from an applied current of 0.1 mA. It turns out, that the magnetic domains pointing either in +z- or −z-direction do not change significantly in terms of size and orientation. This is illustrated in Figure 4.6, where only the x-component of the magnetization is visualized. The grey regions in between the domain walls occupy nearly the same areas in all cases and it can be seen clearly, that the magnetization of the domain walls itself changes and aligns with the applied external field. Therefore, an applied small current in the transversal direction would not affect the magnetization behaviour in the longitudinal arm due to a big current density.

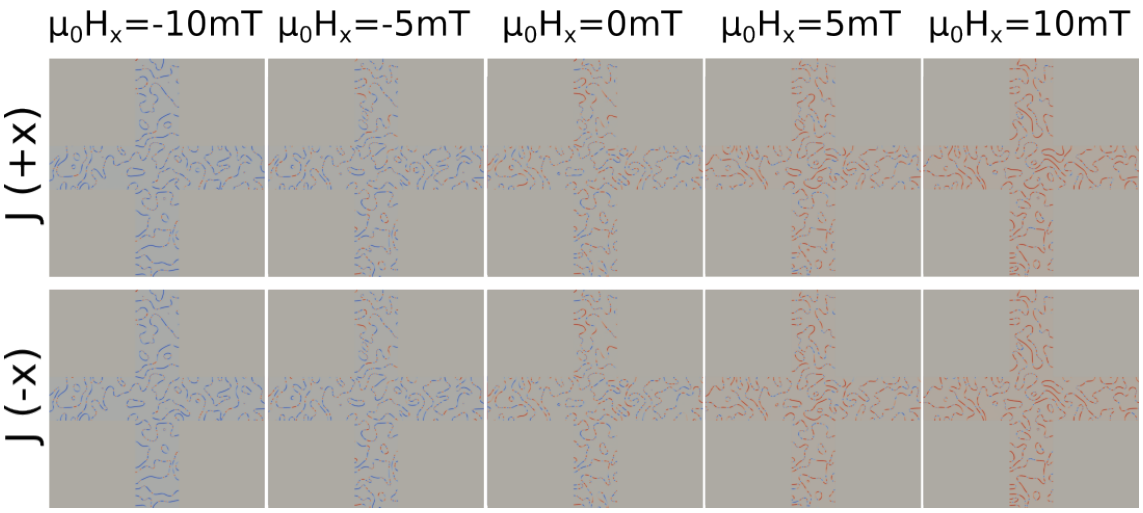

Figure 4.6: Field sweep with illustrated x-component of the magnetization for a current density of $J_e = 7.2 \cdot 10^9$ A/m^2 flowing in positive and negative x-direction.

Also for the case of a small applied current, the signal curve and the SMR and AMR curves can be depicted. In Figure 4.7, the signal curve for the small current is visualized. The signal is tiny compared to the signal in Figure 4.4, since the magnetic domains do not change significantly in size. Moreover, the curve does not exhibit a smooth linear range. In Figure 4.8, the AMR and SMR curves are depicted. Since the effect of polarization due to SOT is negligible for the small current, the y-component remains zero. The x-component increases almost linearly, which results in a parabolic behaviour of the AMR curve, where the corresponding strength is very small.

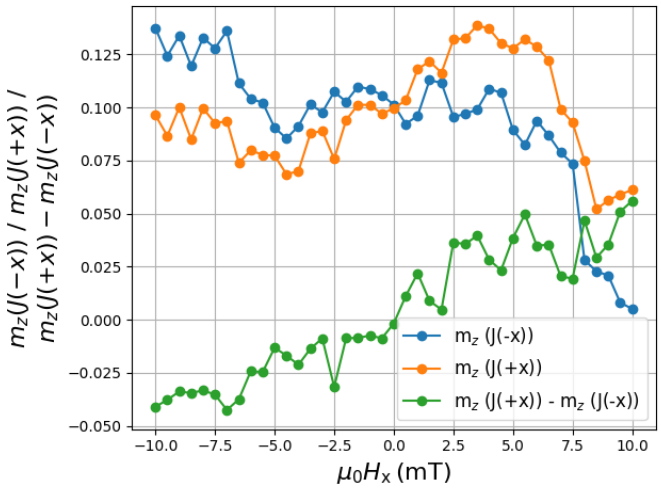

Figure 4.7: Z-Component of the magnetization as a function of external field and signal curve for the current $I = 0.1$ mA.

The possibilities to enlarge the linear range of the transfer curve should be explored. Potentially, the current density flowing through the Hall cross can be varied. Therefore, 3 different currents $I = 2.5$ mA, $I = 3$ mA and $I = 3.351$ mA are assumed. First, all temperature dependent parameters are also varied according to the exploited current density. This leads to the results in Figure 4.9. For smaller currents, that are large

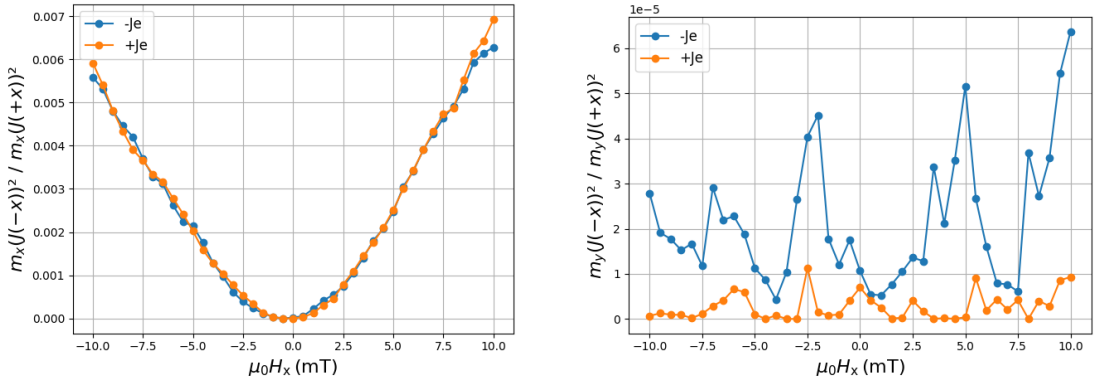

(a) AMR signal curve.

(b) SMR signal curve.

Figure 4.8: AMR and SMR signal curves for the different current directions for $I = 0.1$ mA.

enough for application, the linear range is larger than for bigger currents. So by using smaller currents, the working window of the sensor could be enlarged. However, the simulation takes also into account the change of the other parameters (especially of the uniaxial anisotropy and the saturation magnetization) with respect to the temperature and hence with respect to the current density. This means, that the current density itself might not be the determining parameter for this change. In Figure 4.10 the simulation is repeated with fixed magnetic parameters and only changing current density. It can be seen, that the linear range stays the same for all current magnitudes. Thus, the current itself does not control the linear range, but dependent parameters might do.

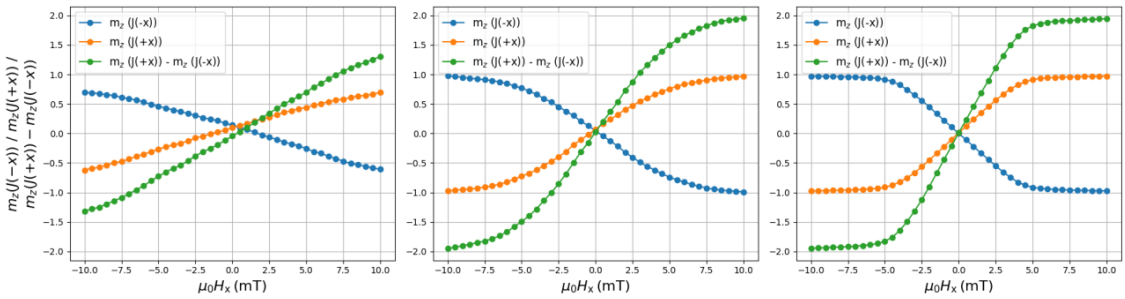

Figure 4.9: Z-Component of the magnetization as a function of external field and transfer curve for the different currents $I = 2.5$ mA, $I = 3$ mA and $I = 3.351$ mA.

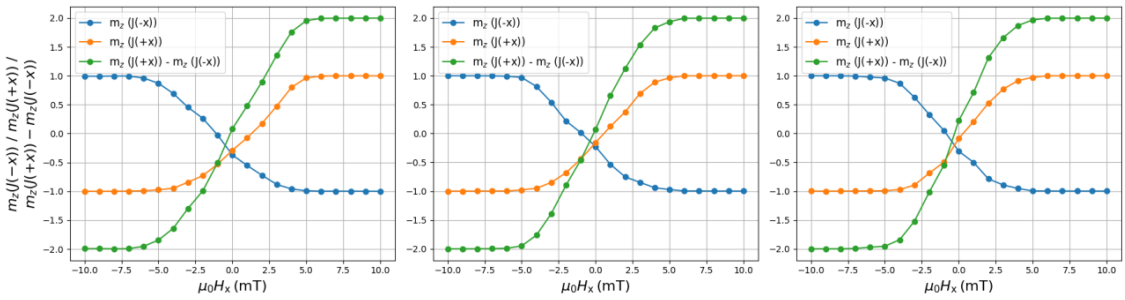

Figure 4.10: Z-Component of the magnetization as a function of external field and transfer curve for the different currents $I = 2.5$ mA, $I = 3$ mA and $I = 3.351$ mA (other magnetic parameters are fixed).

The examination of the other magnetic parameters in terms of their potential to enlarge the linear range should be waived in this thesis. As illustrated in Figure 4.9, a combination of the changing parameters increases the linear range slightly, but as it turned out during simulations tuning only the single parameters does not improve the transfer curve. The increase of the linear part in the above figure results in small bumps in the curve making it unprofitable to reduce the current density with the according parameter changes. Other possibilities have to be exploited to achieve a larger linear range. Especially the use of multistack structures, i.e. stacking heavy metal, ferromagnet and insulator more times above each other, seems promising, but the investigation of such systems goes beyond the scope of this thesis.

4.2 Impact of relaxation time in simulation

In this section, a small comment should be given about the impact of the relaxation time in simulation on the sensor behaviour. It is crucial to let the system relax long enough such that the right experimental reaction can be simulated. This is necessary in any simulation and it can be also seen in the following example. For the upper simulations a simulation time of about 20 ns is used. For the first simulations performed for this section, it was assumed that a relaxation time of 5 ns is sufficient. With a relaxation time of 5 ns the field sweep in Figure 4.3 looks differently. It is visualized in Figure 4.11. In this non-relaxed field sweep, skyrmions appear and the magnetic domains for zero field are smaller than in the relaxed field sweep. This circumstance distorts the result since in experiment the strong current is able to drive out the skyrmions also for small external fields reducing the linear range of the Hall cross sensor.

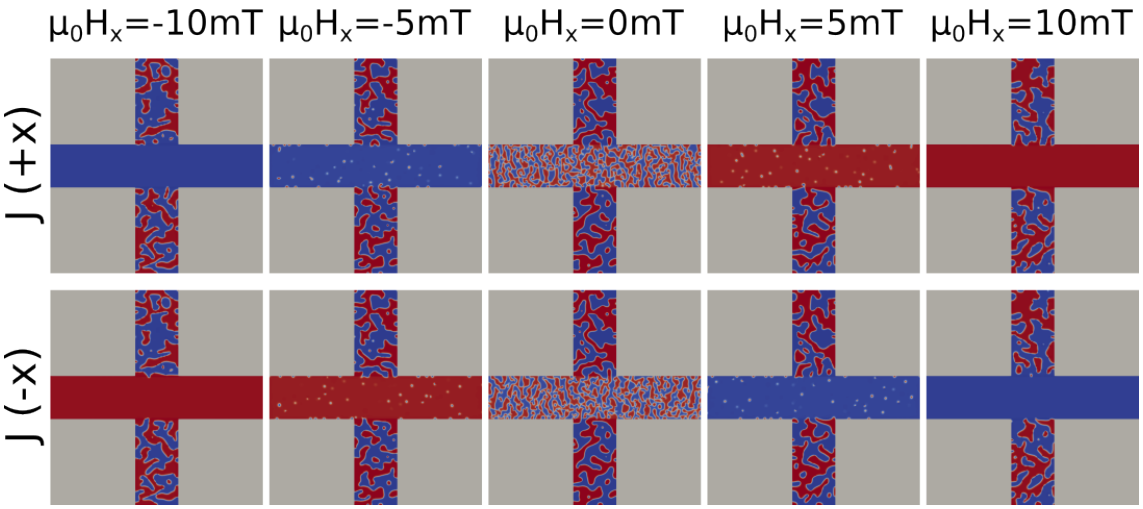

Figure 4.11: Field sweep for big current density flowing in positive and negative x-direction with a too short relaxation time.

The impact of the relaxation time on the sensor transfer curve is illustrated in Figure 4.12. The linear part shrinks for higher relaxation times and a relaxation time of 5 ns is not sufficient to imitate the trend of an experimental execution, whereas 20 ns is already an adequate amount of time.

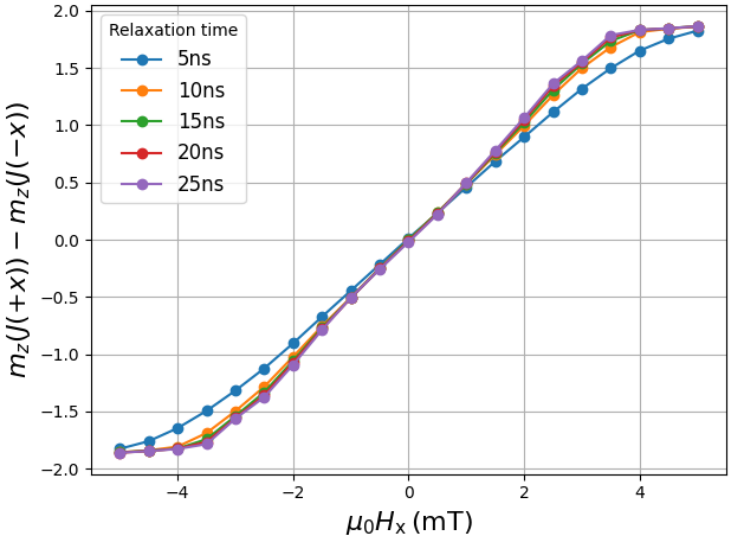

Figure 4.12: Impact of the relaxation time in simulation on the transfer curve.

Chapter 5

Multiturn Sensors

Rotational counters have many fields of application. They can be necessary for industrial applications, in the automotive sector or in other applications used on a daily basis. The point of these sensors is to count the number of performed rotations with a finite number of rotations maximally countable. Therefore, they enable rotation counting and position determination for a limited amount of rotations or a limited movement. In today's typical realizations, they rely on a steady power supply. This means, that the physical mechanism behind the rotation counting is based on current flowing through the sensor all the time, so during initialization, counting and read-out. With this steady power supply, reliable multiturn counters can be realized easily based on different physical principles.

However, the need for steady power supply leads to a fundamental weakness of the sensor. If the power supply at any time of the rotation sensing is interrupted e.g. by a power failure, the information about the current number of performed rotations gets lost and cannot be recovered without the help of other means. The multiturn counter itself cannot recover this information. This fundamental problem should be illustrated with an example of the macroscopic world visualized in Figure 5.1. Suppose there is a gate at a property's driveway, which opens and closes automatically. The closed state is the initial state. The rotary motor opening the gate is activated and determines the position of the gate by counting the number of performed rotations. At some point in the opening process the power supply is interrupted and the gate stops. After fixing the problem, the power supply is ensured again and the gate could continue to move. However, the rotational counter lost the information about the position of the gate, which cannot be recovered. The system needs to be fixed somehow.

Of course, for such a big system, which is not so delicate, there are many ways to overcome this circumstance. For example, the gate could open and close to certain positions by default, which makes it obsolete to determine the position in between. This can be realized with light barriers or contact sensors. In any system, an initial position can be defined, e.g. the open position, to initialize the system again and to start the counting process anew. This is also a common method for microscopic rotational sensors, which rely on steady power supply, to fix this circumstance. However, it would be much more favourable, if the information about the performed rotation is not lost due to an interruption in the power supply. The system could go on with the movement from any position after the failure. Therefore, it would be beneficial to realize a sensor concept, which needs power supply only for initialization and read-out and is able to count performed rotations without any intervention during the actual sensing process.

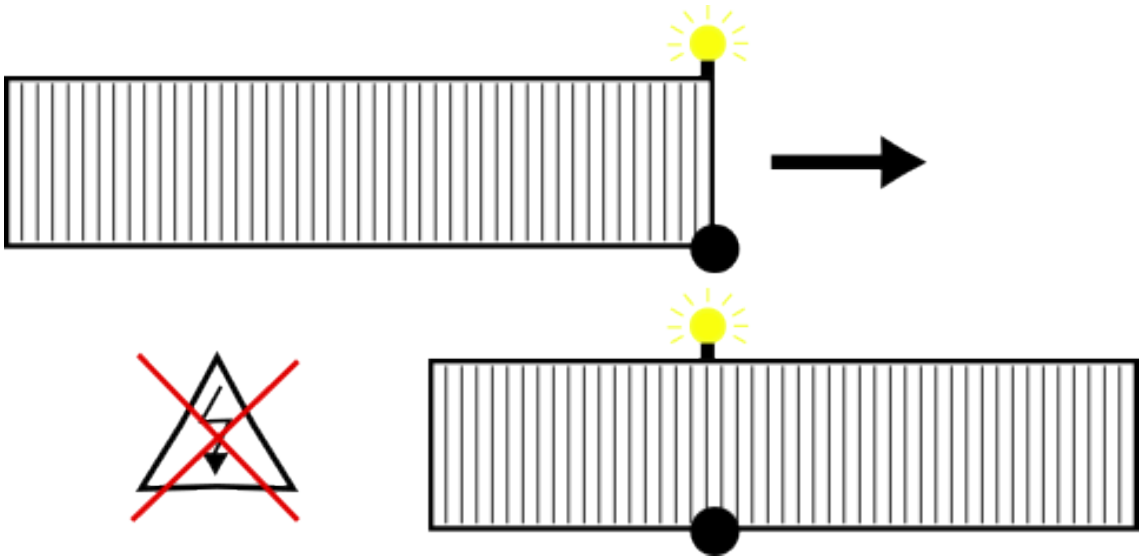

Figure 5.1: Schematic illustration of an automatic gate at a property's driveway as a macroscopic example for the problem of multiturn counters relying on steady power supply.

This is the goal of the multiturn counters presented in this chapter of the thesis. There are two main concepts of how to realize such counters. The first one uses the movement of domain walls in magnetic strips due to an external field. This idea is already exploited by many different approaches, since it is easy to understand and to use. By choosing the geometry of the stripe for the DW propagation wisely, reliable counters can be built. The second concept is based on the movement of magnetic bubbles as used in magnetic bubble memories. These memory devices were developed and examined in the 1970s and 1980s and the scientists understood the physics behind the memory concept quite well. Exploiting it for a multiturn counter is a new approach.

5.1 Motion of Domain Walls in magnetic stripes

Applying an external field on a magnetic stripe with a certain initial magnetization leads to the alignment of the magnetic moments according to the magnetic field, if the magnetic material is soft-magnetic. In Figure 5.2 a stripe is visualized, where the initial magnetization is pointing first into the positive x-direction (rightwards) and an external field is applied pointing left (into the negative x-direction). This leads to the generation of a DW separating the domain with the magnetization pointing into positive x-direction (red region) and the domain pointing into negative x-direction (blue region). Since the magnetization pointing into negative x-direction is favoured due to the external field, the DW propagates leftwards and is driven out of the stripe after relaxation of the system.

This easy concept can be used to count the rotations of a magnetic field by choosing a stripe geometry, where the DW can propagate through in a controlled way. The obvious choice is a spiral. The DW propagates circular in the structure and one rotation of the external field corresponds to one rotation of the DW. For the spiral, an open and a closed form can be used. These forms are described in the paper (Borie, Voto, et al., 2017) and schematically illustrated in Figure 5.3. The open form consists of a DW generator at the beginning and a pointed tail at the end. A rotating external field generates DWs,

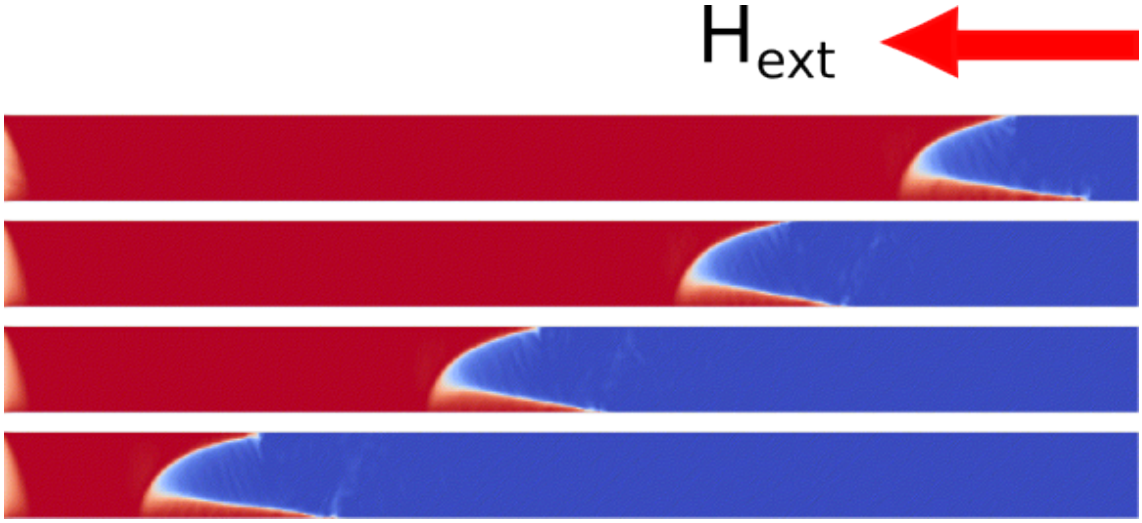

Figure 5.2: Schematic illustration of DW motion through a magnetic stripe due to an external field pointing left. The colour refers to the x-magnetization with red indicating a magnetization pointing rightwards and blue indicating a magnetization pointing leftwards.

which then propagate circular. In the closed form a DW has to be generated in the geometry, e.g. by a short strong magnetic field application or a local one. The benefit of this form is that after n rotations, where n is the number of loops, the initial state is reached again. In the paper (Borie, Voto, et al., 2017) the superiority of the closed loop in many realization is explained, but also the need for additional structural details to overcome problems at the crossings of the wires. Other papers describing and improving the DW motion in spirals are (Diegel et al., 2009) and (Borie, Wahrhusen, et al., 2017) amongst many others.

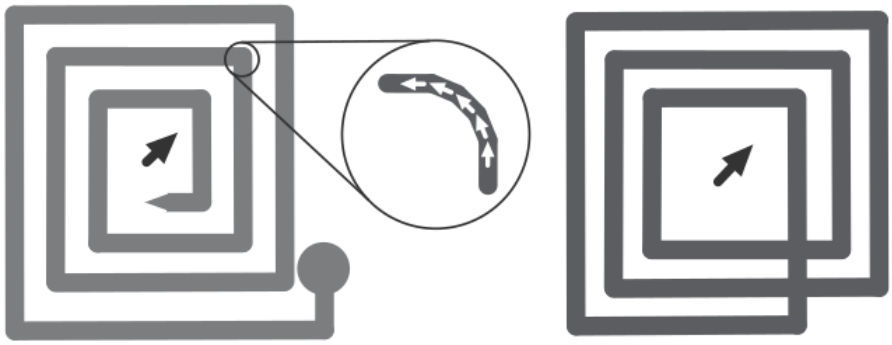

Figure 5.3: Open and closed form of a spiral as potential geometry for DW propagation. (taken and adapted from Borie, Voto, et al., 2017, p. 1).

All these reports describe 180° DWs, which separate domains with opposing magnetization directions. Without going too much into detail, one major problem of the wire crossing is explained in the paper (Borie, Voto, et al., 2017) and visualized in the following. Depending on how the magnetization is pointing in the DW and towards it, a Head-to-Head DW or a Tail-to-Tail DW is present visualized in Figure 5.4. If the magnetization in the DW is pointing into the same direction as in the transversal arm to be crossed, the crossing will happen without further issues. In the case of Figure 5.4 the crossing of the Head-to-Head DW is uncritical, since the magnetization in the

transversal arm points upwards. If this is not the case and a Head-to-Head DW tries to cross an arm with a magnetization pointing downwards, the situation is critical. This is illustrated in Figure 5.5, where besides the normal crossing two other outcomes can be generated.

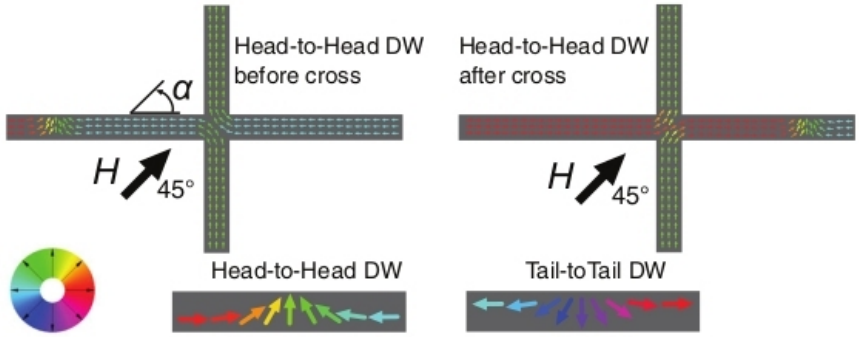

Figure 5.4: Propagation of a Head-to-Head DW through a crossing of wires in an uncritical configuration. (taken and adapted from Borie, Voto, et al., 2017, p. 3).

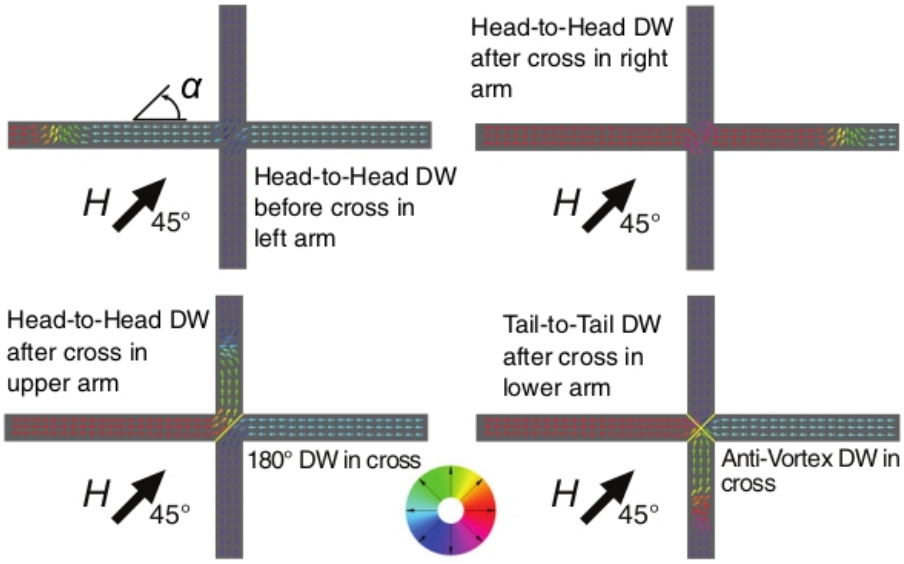

Figure 5.5: Propagation of a Head-to-Head DW through a crossing of wires in a critical configuration. (taken and adapted from Borie, Voto, et al., 2017, p. 3).

In the paper (Borie, Voto, et al., 2017) some geometrical resorts are presented, where a syphon structure at the crossing points has to be mentioned specifically. However, this detailed examination would go beyond the scope of the presentation of this counter concept, which will not be investigated further in this thesis. Besides using 180° DW, also 360° DW appearing in planar magnetic nanowires are exploited for propagation. This is presented in the paper (Geng & Jin, 2012).

5.1.1 Cusp sensor

This part of the thesis focuses on the concept presented in the paper (Mattheis et al., 2012). A loop with specifically shaped obstacles is used to count the rotations of the magnetic field. The obstacles hamper and slow down the circular propagation of the DW in the wire loop. The presented cusp geometry of the obstacles is shown in Figure 5.6 in the left subfigure. The wires have a certain width w, which is $w = 160$ nm in the report. The opening angle 2θ and the length of the neck l determine the window, for which magnetic field strengths the concept works, and how stable the rotation counting can be performed. On the other 3 subfigures, the magnetization configurations for different directions of the external magnetic field are illustrated. The colour quantifies the y-component of the magnetization with red pointing upwards and blue pointing downwards. The DW moves through the cusp in half a rotation. The propagation seems to be controlled and stable.

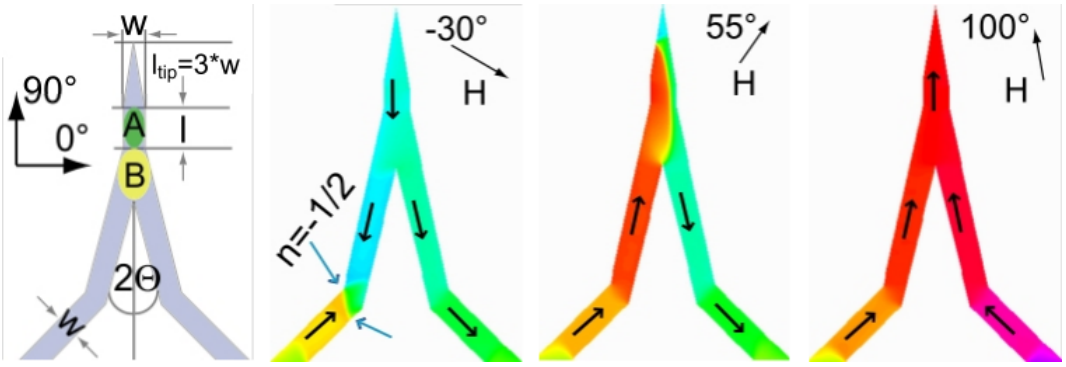

Figure 5.6: Geometry of cusp obstacles and magnetization for different directions of the external magnetic field. (taken and adapted from Mattheis et al., 2012, p. 2).

Combining these cusps in a loop leads to a potential multiturn counter. In Figure 5.7, one cusp is put into a wire loop and the position of the DW is shown for different directions of the external magnetic field. After one and a half rotations of the field, the DW is at the initial position again. A huge benefit of the cusp design is the possibility to combine more and more such obstacles in one loop without further issues. In Figure 5.8, 6 cusps are combined in one loop and 4 rotations can be counted. The experimental design in this Figure presented in the paper (Mattheis et al., 2012) shows a potential experimental realization exploiting the GMR effect with Gnd being the ground, V_{cc} being the supply voltage and U_{b1} and U_{b2} being bridge voltages indicating the relative magnetization direction in the adjacent arms, where the GMR of a nanowire is determined by the magnetization state with respect to a reference magnetization direction Ref.

If the length of the neck l in Figure 5.6 is fixed to be $l = 2 \cdot w$, the operation margin of the externally applied magnetic field is only determined by the opening angle 2θ. In Figure 5.9, this margin found in the paper (Mattheis et al., 2012) is visualized. The red dots indicate the minimal field, at which the sensor principle works with the given geometry, and the black dots indicate the maximal one. Below the minimal field, the propagation of the DW is not ensured and above the maximal field, other parts of the loop could suffer from unwanted reversals of the magnetization. The blue dots indicate the operation margin, which decreases with increasing opening angle. This is meaningful, since a wider opening angle makes the obstacle less efficient.

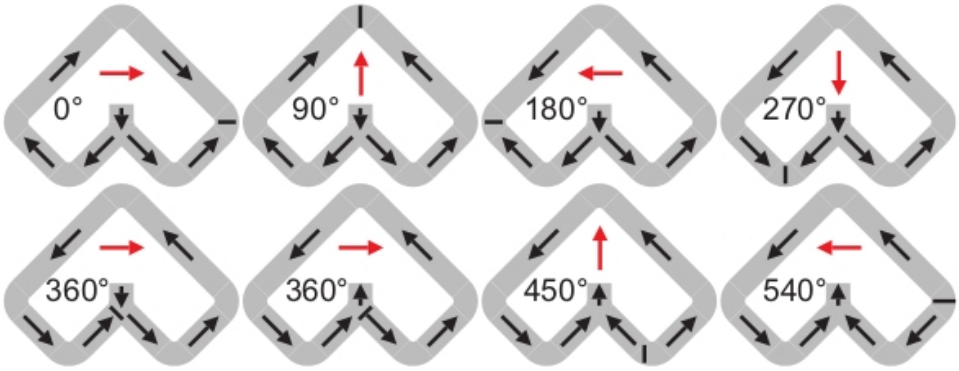

Figure 5.7: Loop with one cusp as obstacle and corresponding magnetization direction depending on the direction of the external magnetic field. (taken and adapted from Mattheis et al., 2012, p. 2).

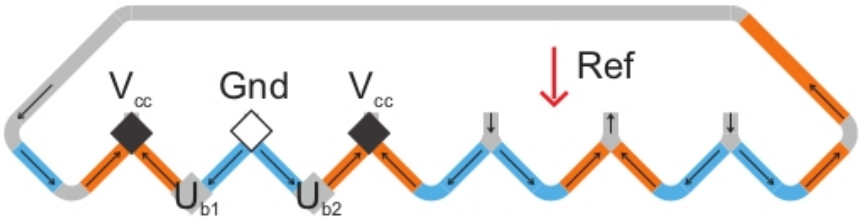

Figure 5.8: More cusp in one loop and potential experimental realization to determine the position of the DWs. (taken and adapted from Mattheis et al., 2012, p. 5).

To confirm the applicability of the cusps as obstacles for DWs, a finite element simulation of such cusps is performed. Therefore, 4 cusps are combined in a row. The permalloy wires have a saturation magnetization of $\mu_0 M_s = 1$ T, zero anisotropy and an exchange constant of $A = 13$ pJ/m. The width is chosen to be $w = 160$ nm as in the reference paper and the opening angle is chosen such that $\theta = 13°$. The length of the neck is set to $l = 2 \cdot w$ and the rotating field in the simulation has a strength of $\mu_0 H_{\text{rot}} = 25$ mT. During simulation it turned out, that the wide operation margin in Figure 5.9 can not be confirmed in simulation, since only 25 mT and slight deviations of approximately ± 2 mT work fine.

The initial magnetization is chosen as shown in Figure 5.10 such that only one DW is in the system. The colour indicates the y-component of the magnetization with red pointing into positive y-direction (upwards) and blue pointing into negative y-direction (downwards). In the light gray regions the y-component is zero and the magnetization is pointing solely along the x-axes. The arrows indicate the magnetization direction locally to make the visualization clearer. From this initial magnetization a counterclockwise rotation of the magnetic field with the magnitude of 25 mT is simulated, starting from the field pointing -30° as illustrated in Figure 5.6.

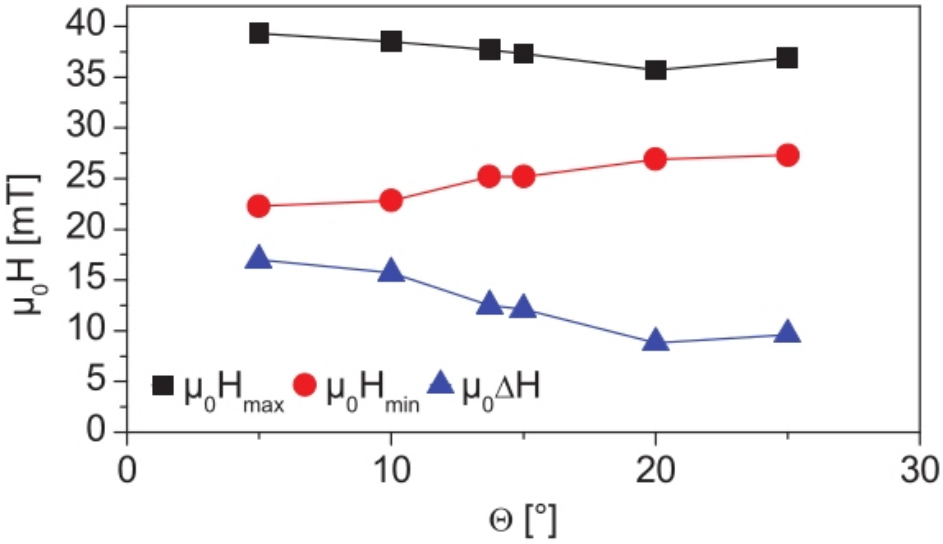

Figure 5.9: Operation margin for the applied rotating magnetic field. (taken and adapted from Mattheis et al., 2012, p. 3).

The rotation simulation is illustrated in Figure 5.11 and the simulation movie can be found on u:cloud.[1] Moreover, the simulation folder is located on GTO3, which is the recent computer for numerical calculations in the scientific group *Physics of Functional Materials* at the University of Vienna.[2] Due to the counterclockwise rotation of the field, the DW propagates along the cusps and after 2 rotations the DW is driven out of the system. This propagation of the DW is very stable and controlled. The presented simulation is performed dynamically, which means that the external field for the LLG-solver rotates constantly. However, if a quasistatic simulation is performed, where the field direction is rotated stepwise and at every distinct direction the system is relaxed, the behaviour of the DW stays the same. Thus, the cusp design can be used for rotation counting.

The row of cusps can be put into one loop and a closed sensor is realized. However, an important aspect has to be taken into account, namely how to initialize the system in practical application. For the mentioned simulation, a DW was put into the system artificially. Reversing the magnetization locally would be one option, but this is quite cumbersome, if only one DW should be in the system. Working with more DWs is another option. However, if the system is saturated, the loop is full of DWs and no information can be extracted from the sensor, since at every nook of the geometry a DW is placed and they move forward in a jointly manner. Thus, one or more DW have to be erased in the loop, which is also cumbersome. Trying out different ways of initializing the system in an easy way led to the following initializing steps:

1. **Saturate the structure:** First the entire geometry is magnetized into one direction. This can be realized by applying a strong magnetic field at first, exceeding noticeably the magnitude of the maximal magnetic field to use as rotating field.

[1] The simulation movie is located at https://ucloud.univie.ac.at/index.php/s/2CQ21jZ9d3lsS16 in the folder *movie_files* and it is named *cusps_in_a_row.mp4*.

[2] The according simulation folder is located on GTO3 with the following directory: /home/gasser/data/master_thesis/cusp_sensor/cusps_in_a_row.

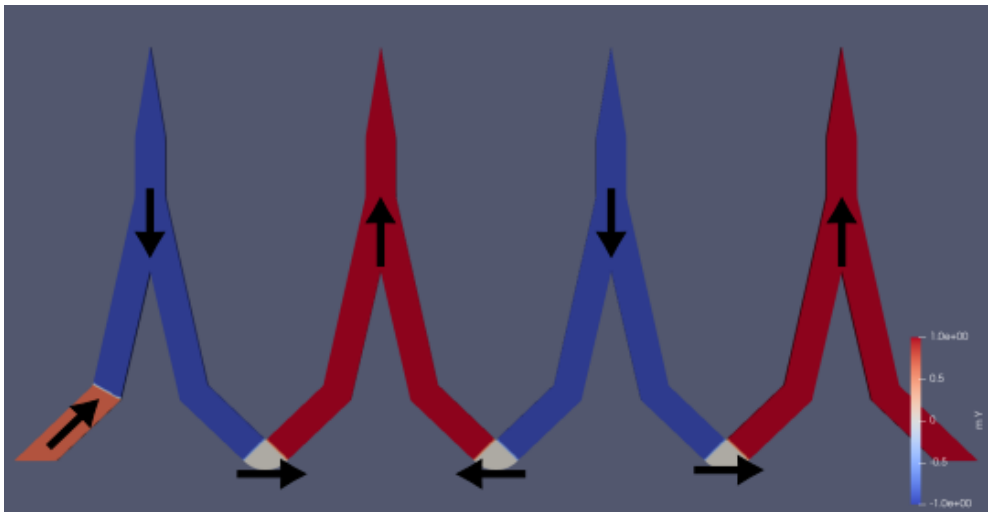

Figure 5.10: Initial magnetization for 4 cusps in a row with one DW in the system. (The colour indicates the y-component of the magnetization).

2. **Fast rotation:** If the rotating magnetic field has a high enough frequency, the DWs can propagate along the cusps, but they get stuck at one corner of the loop. Thus, all the DWs join to one DW at one corner of the loop. The initial state is reached.

3. **Normal rotation:** Afterwards, the rotational frequency of the applied external field is decreased such that the remaining DW propagates through the entire structure and rotation counting is enabled.

The ability of these steps to initialize the system properly should be proven in simulation. First, the system is saturated with a magnetization pointing downwards into negative y-direction by applying a strong starting field H_{start}. This is illustrated in Figure 5.12 in the upper left subfigure. The loop is filled with DWs labeled by the black arrows. Then the magnetic field with the "standard" field magnitude H_{rot} is rotated counterclockwise with a high rotational frequency. In the case of this simulation, a frequency of 20 MHz is used for the rotation of the magnetic field. The behaviour of the DWs is illustrated in the other subfigures of Figure 5.12, where at total 3.5 rotations are performed. It can be seen, that after each roation the number of DWs decreases, since they get stuck in the upper right corner of the loop and they cannot pass the long arm at the top of the loop. After 3.5 rotations only one DW remains in the system at the upper right corner. This is the initial state for the multiturn counter. Afterwards, the actual sensing process can start, where the rotational frequency of the magnetic field is smaller. In simulation, 5 MHz are used for the rotation at the sensing process, which works fine. In practical realization the rotational frequency is not constant, typically, but if it stays well below the fast rotational frequency hampering the propagation of the DW, no further issues should occur.

The DW propagation after the initializing steps is reliable. An entire rotation simulation is visualized in Appendix B, where a magnetic field of 25 mT is rotated several times. The red arrow illustrates the current direction of the magnetic field and the black arrow shows the position of the DW. Since it works for the 4 cusps in Figure 5.11, it is not surprising, that it also works in a loop constellation. Note that after one full propagation of the DW, the magnetization configuration in the cusps is reversed. Since 5 cusps are

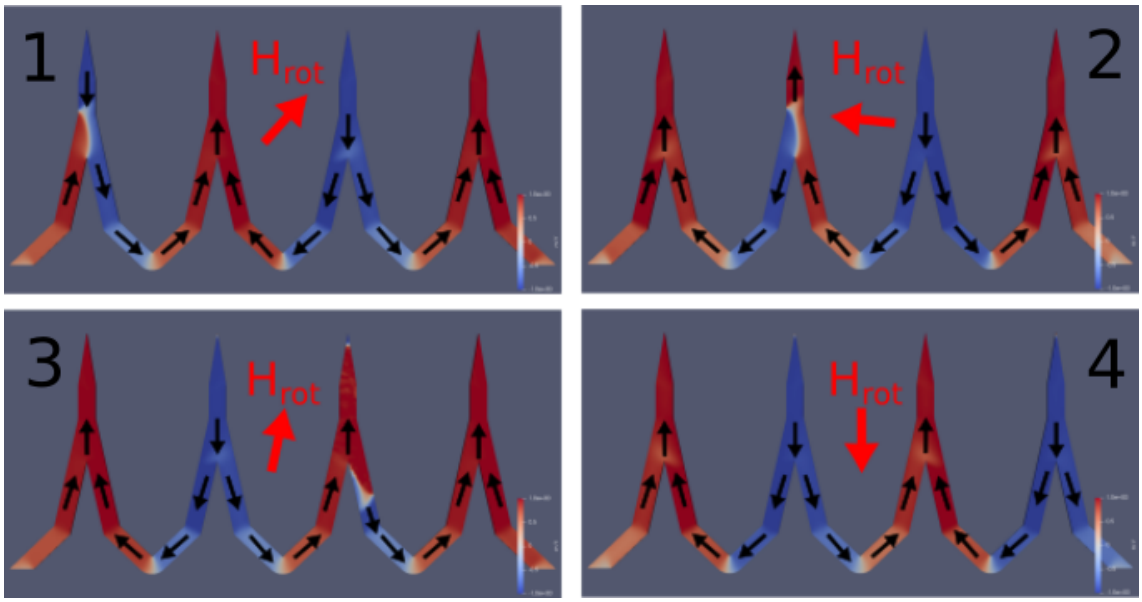

Figure 5.11: Magnetization configuration for different field directions of a counterclockwise rotating magnetic field. The subfigures ordered by numbers depict some consecutive situations. The colour indicates the y-component of the magnetization. (The simulation movie can be retrieved on https://ucloud.univie.ac.at/index.php/s/2CQ21jZ9d3lsS16/download?path=%2Fmovie_files&files=cusps_in_a_row.mp4. The according simulation folder is located on GTO3 with the following directory: /home/gasser/data/master_thesis/cusp_sensor/cusps_in_a_row.)

simulated, first 3 cusps are magnetized downwards and 2 upwards, whereas after one full propagation 3 cusps are magnetized upwards and 2 downwards. The full simulation movie including the initializing steps and the normal rotation can be found on u:cloud.[3] Moreover, the simulation folder is located on GTO3.[4]

Instead of having a high rotational frequency of the magnetic field at first, it might be possible to think of other possibilities of how to hamper the DWs at passing the long arm at the top of the loop and merging them at the upper right corner. Potentially, some obstacles at the long arm could be included, which cannot be passed with small fields, but with the fields used in the actual sensing process. Then the system can be initialized with the rotation of the smaller field, but the field has to be strong enough such that the DWs can propagate along the cusps. In simulation, the operation margin for the rotating magnetic field is very small, which makes this initialization process difficult. However, it might work in practical realization. Other possibilities might also be possible, but varying the angular frequency of the rotating field can be realized easily.

For the given configuration, the cusp sensor works well. The main problem of this concept is the need for small widths of the magnetic wires. In the simulation a width of $w = 160$ nm is used. This width is also used in the experimental verification in the paper (Mattheis et al., 2012) with some deviations in the practical realization. In simulation, it turns out that slightly bigger widths are also tolerable until approximately 300 nm. This can be achieved by decreasing the driving rotating magnetic field. However, increasing

[3]The simulation movie is located at https://ucloud.univie.ac.at/index.php/s/2CQ21jZ9d3lsS16 in the folder *movie_files* and it is named *cusp_loop.mp4*.

[4]The according simulation folder is located on GTO3 with the following directory: /home/gasser/data/master_thesis/cusp_sensor/loop.

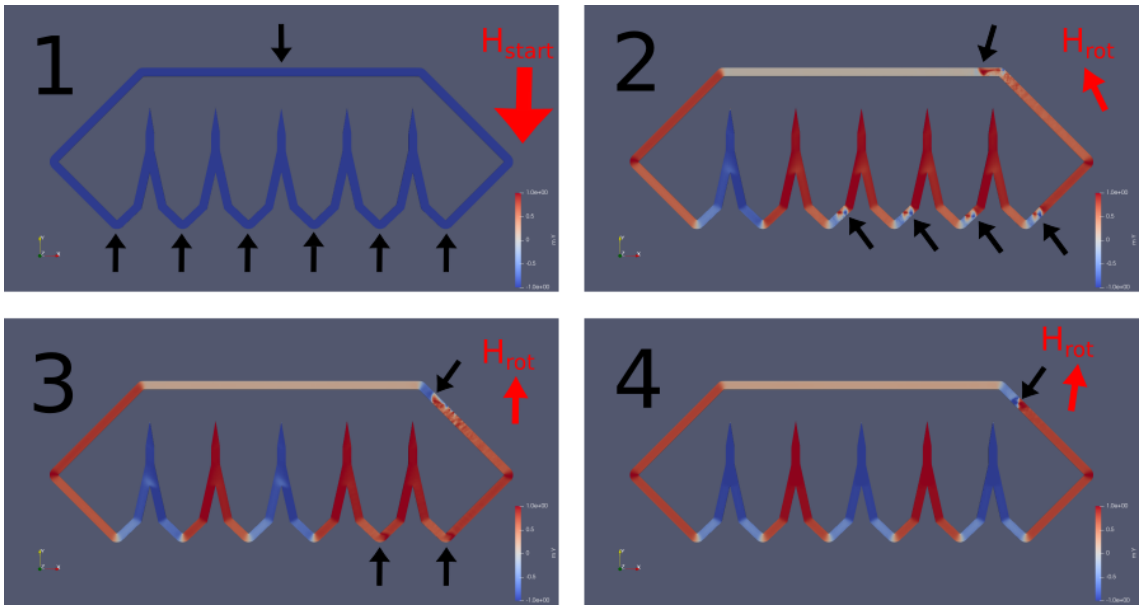

Figure 5.12: Initializing steps for the cusp loop and corresponding magnetization configuration. The subfigures ordered by numbers depict some consecutive configurations for a counterclockwise rotating field. 3.5 rotations are performed during initialization. The colour indicates the y-component of the magnetization. (The simulation movie, which shows the displayed initializing steps at the beginning, can be retrieved on https://ucloud.univie.ac.at/index.php/s/2CQ21jZ9d3lsS16/download?path=%2Fmovie_files&files=cusp_loop.mp4. The according simulation folder is located on GTO3 with the following directory: /home/gasser/data/master_thesis/cusp_sensor/loop.)

the width beyond this threshold is troublesome. The origin of the troubles at wider wires is the region B in the left subfigure of Figure 5.6. The magnetic field tries to change the magnetization in the region B according to its direction. This is already visible in the performed simulation procedure in Figure 5.11. The respective regions in the cusps, that are magnetized oppositely to the magnetic field, appear brighter than the tops and the branches of the respective cusps. This illustrates an initiating switching of the magnetization according to the external field. If the field strength stays under a certain threshold depending on the width of the wire, the alignment of the corresponding magnetization is inhibited. For bigger widths, the region B becomes bigger and the field strength has to be lowered correspondingly. If the region becomes too large, the magnetic field strength cannot be decreased sufficiently, such that the DWs move appropriately and the switching of the magnetization in the respective region is hindered. Trying to solve this problem, the geometry was adapted with respect to the opening angle 2Θ, the height of the cusps and the height of the tips throughout the work for this thesis. However, for wider wires with widths of approximately 500 nm the geometrical concept seems to be unusable. The magnetization in the troublesome region aligns too easily according to the external field. Maybe a rough adaption of the geometry solves this circumstance. Another possibility might be to use another material with non-zero uniaxial anisotropy or other different material parameters. Nevertheless, this might lead to problems in the DW motion and therefore to other severe troubles.

5.2 Motion of magnetic bubbles

Magnetic Bubble Memory (MBM) is based on the motion of magnetic bubbles in a magnetic garnet film. These bubble domains are small regions in a homogeneously magnetized garnet material, that appear with reversed magnetic polarity. The bubbles are stabilized by an external magnetic field exerted by a permanent magnet. Therefore, the bubble memory concept is nonvolatile since the bubble do not vanish due to missing power supply to the sensor. The magnetic bubbles are moved by guiding structures that produce magnetic field gradients. (Nielsen, 1979)

The schematic structure is illustrated in Figure 5.13. The permalloy guiding structure consists of T-shaped and I-shaped elements that move the magnetic bubbles existing in the underlying magnetic garnet film. H_{BIAS} is the bias field that stabilizes the magnetic bubbles. The clockwise rotating magnetic field H_ω moves the magnetic bubbles into the marked bubble motion direction. This movement is based on the magnetic poles developing in the guiding structures due to the rotating driving field H_ω.

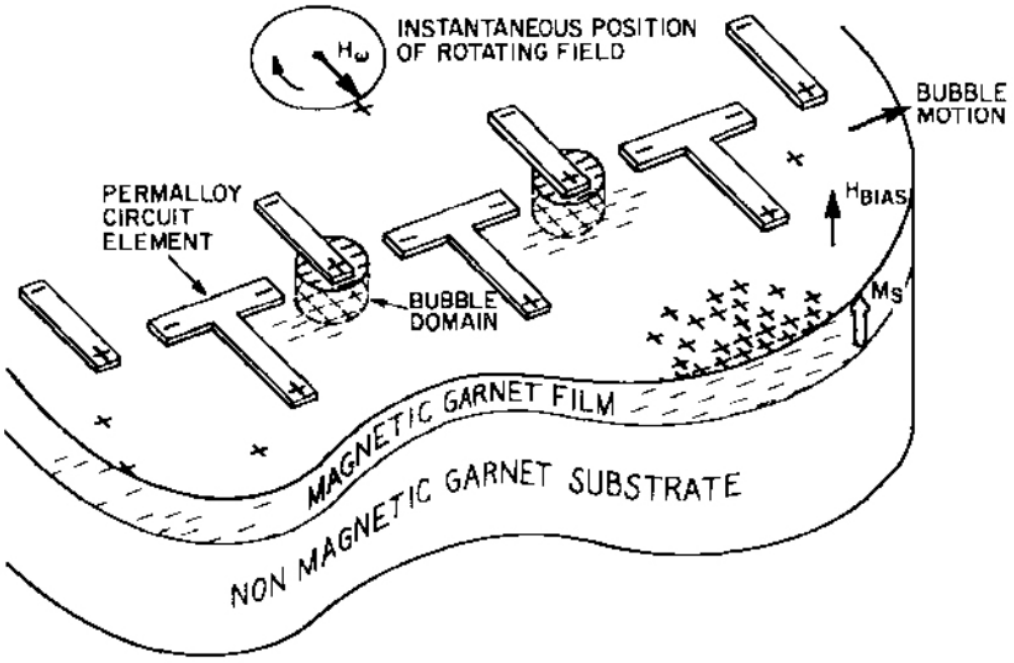

Figure 5.13: Visualization of basic structure for magnetic bubble devices. (taken from Nielsen, 1979, p. 89).

The magnetic poles and the corresponding positions of a magnetic bubble are visualized in Figure 5.14. The periodically appearing TI-structure and the clockwise rotating magnetic field cause the magnetic bubble to move rightwards along the guiding structure. After one full rotation of the driving field H_r the bubble is moved from one TI-group to the next one. The plus poles in the guiding structure attract the bubbles, where the magnetic polarity is reversed pointing anti-parallel to the bias field illustrated in Figure 5.13. Besides the TI-structure, also other guiding structures are used for magnetic bubble memory, for example a guiding structure consisting of V-shaped elements. However, the TI-structure is the most commonly used concept in literature.

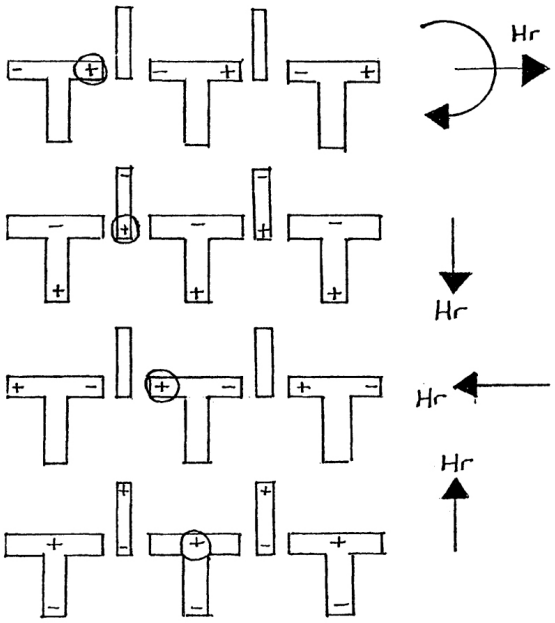

Figure 5.14: Visualization of developing magnetic poles in the guiding structure forcing the magnetic bubble to move. (taken and adapted from Gowland, 1977, p. 8).

For MBM, a rotating driving field has to be produced artificially. This is done with two coils wrapped around the above described structure, that are arranged perpendicular to each other. This is illustrated in Figure 5.15. By sending a current through a coil, a magnetic field along the axis of the coil is produced. By varying the current flowing through two coils standing perpendicular to each other, a rotating magnetic field inside the coils can be generated. (Salzer, 1976)

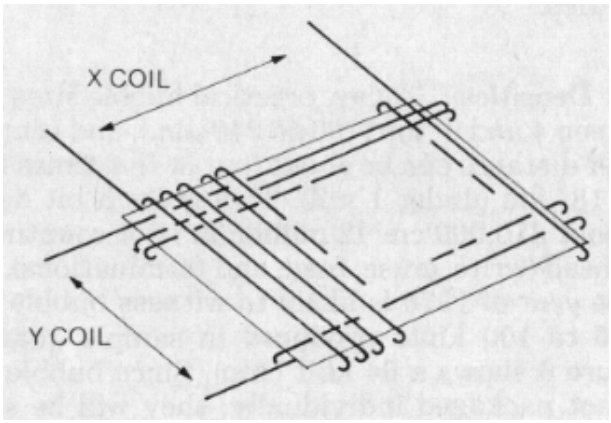

Figure 5.15: Coils wrapped around the structure for magnetic bubble memory to generate a rotating magnetic field. (taken from Salzer, 1976, p. 37).

MBM uses the bubbles to store information in the sense that bubble and no bubble are related to the bits 0 and 1 or vice versa. By moving the bubbles to certain positions in the garnet film, a certain bit sequence can be achieved, which enables the storage of information. Bubbles are generated by specifically structured elements in the guiding structure that serve as generators (Gowland, 1977) or by electric current pulses that are exerted to reverse the bias field direction locally. (Theis, 1984)

To adapt the concept for multiturn counters, no rotating field has to be generated artificially. A permanent magnetic field is exerted in-plane and the rotation to be measured causes the movement of the magnetic bubbles. Since the design has been realized in MBM, it can be expected that the adaption for rotation sensing should be feasible. However, many problems occurred when trying to exploit this concept for rotation counters.

First tries are done with small dimensions in the range of a few nanometers. Thus, the thickness and the width of the guiding structure elements are chosen to be a few tens of nanometers, for example 50 nm. Also, the bubble garnet is chosen for bubbles with the same size. Nevertheless, to be able to move bubbles the guiding structure has to split up into different magnetic domains. This splitting does not happen in such small structures. The magnetization in these small elements points into the direction of the rotating driving field, but no attracting magnetic poles exist.

Typical Magnetic Bubble Memory devices exhibit bigger dimensions. The width of the guiding structure elements amounts to some micrometers and so does the diameter of the magnetic bubbles. For example, the paper (Nielsen, 1979) proposes a width of the guiding structure elements of 3 μm to move bubbles with a size of 3 μm. Throughout the work for this thesis, many different parameters and sizes were used to see, if the concept works for rotation counting. The paper (Nielsen, 1979) offers different potential material choices from many different approaches in the past. Unfortunately, none of the materials and structural concepts worked out well in simulation. The magnetic bubbles do not move according to the rotating field. This is especially surprising since Magnetic Bubble Memory devices were realized with stable bubble movement.

The purpose of this thesis is not to show all tries performed, since most of them do not work. However, the best and most promising try throughout the simulation approaches should be mentioned in the following. The approach by (Bullock et al., 1975) is investigated, who used the compositions $Lu_xSm_{3-x}Fe_5O_{12}$ with $1.5 \leq x \leq 1.9$ as bubble garnet. For the guiding structure, permalloy is used. The material parameters are summarized in Table 5.1. Additionally, other important structural details as the thickness of the isolation layer between the guiding structure and the bubble garnet, the diameter of the magnetic bubbles and the necessary fields are given in this table.

	Bubble garnet	**Permalloy**
Saturation magnetization $\mu_0 M_s$	0.2 T	1 T
Anisotropy constant K	30 kJ/m^3	0 J/m^3
Exchange constant A	8.2 pJ/m	13 pJ/m
Thickness of layer	1.5 μm	20 nm
Thickness of isolation	50 nm	
Bubble diameter	0.5 μm	
z-Bias field	100 mT	
Rotating driving field	10 mT	

Table 5.1: Material parameters for the bubble garnet and the permalloy as well as structural parameters.

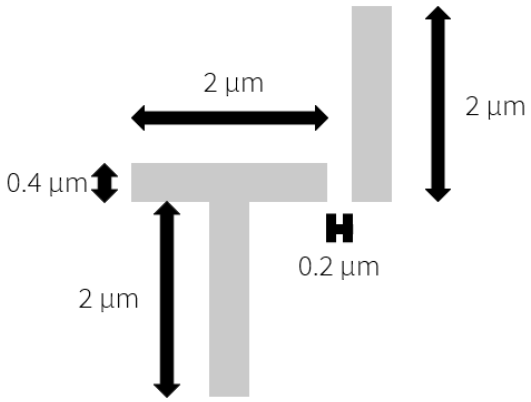

Figure 5.16: Dimensions of the used TI-guiding structure.

In Figure 5.16, the dimensions of the exploited guiding structure with the T-shaped and I-shaped elements is depicted. The lengths of the longer arms amount to 2 μm and the width of the structure amounts to 0.4 μm, which is slightly smaller than the diameter of the magnetic bubbles. The distance between the elements is chosen to be smaller than the width of the elements, which deviates from the geometry described in (Bullock et al., 1975). This is due to the problem, that the bubbles do not jump from one element to another. Larger distances were also investigated without success.

Instead of simulating a rotating field directly, which did not work out well for other approaches, the rotation is simulated quasistatically. Thus, the driving field is exerted in distinct directions simulating the behaviour of a rotation, however ensuring, that the system is able to relax for every distinct field direction. This is important to ensure, since in simulation only nanoseconds elapse, whereas in reality the time spans can be significantly larger. The simulation strategy is to exert the driving field in-plane into 4 different directions, namely upwards, downwards, leftwards and rightwards. The effect of the different field directions on the magnetization of the guiding structure can be seen in Figure 5.17. The elements split up into different magnetic domains and magnetic poles develop. Especially for the downward direction, the plus pole in the middle of the horizontal T-bar is noticeable. This configuration is able to attract the bubble at this plus pole best. Moreover, the other directions seem to generate the correct patterns to move the bubble. Unfortunately, the magnetic poles, especially the plus pole, are not so remarkable than for the downward direction. This leads to an uncontrolled motion of the magnetic bubble. For a clockwise rotating field, the bubble should move rightwards, but in Figure 5.18 the motion of a bubble under such constraints is simulated. The initial position for the left-pointing field is correct, but the bubble does not jump to the I-shaped element. Instead, it moves closer to the T-shaped element under the influence of the plus pole for the field pointing downwards. This configuration seems to be the only stable configuration, where the bubble is attracted towards the middle of the horizontal T-bar. Afterwards, the bubble moves at the T-shaped element in an uncontrolled manner. The simulation movie of this bubble motion is available on u:cloud.[5] Moreover, the simulation folder can be found on GTO3.[6]

[5]The simulation movie is located at https://ucloud.univie.ac.at/index.php/s/2CQ21jZ9d3lsS16 in the folder *movie_files* and it is named *bubble_motion.mp4*.

[6]The according simulation folder is located on GTO3 with the following directory: /home/gasser/data/master_thesis/bubble_sensor.

The jumping of the bubble between the guiding elements does not work out properly. Maybe the influence of the guiding structure in the z-direction on the garnet film is too small or the guiding structure is not designed properly such that the domains do not split up correctly. However, Figure 5.17 shows appropriate domains and the downwards configuration seems to attract the bubble properly. Maybe the thicknesses of the layers should be adapted or another bubble garnet material works better, but as already mentioned many different combinations of materials and dimensions were simulated with rotating fields and quasistatically rotating fields and none of them worked out well. It is astonishing that in experiment the Magnetic Bubble Memory is realized with stable bubble motion. Normally, the bubbles should be easier to control in simulation, since disturbances occurring in experiment are neglected. Nevertheless, when trying to exploit magnetic bubble motion for rotation sensing, it seems to be the other way around.

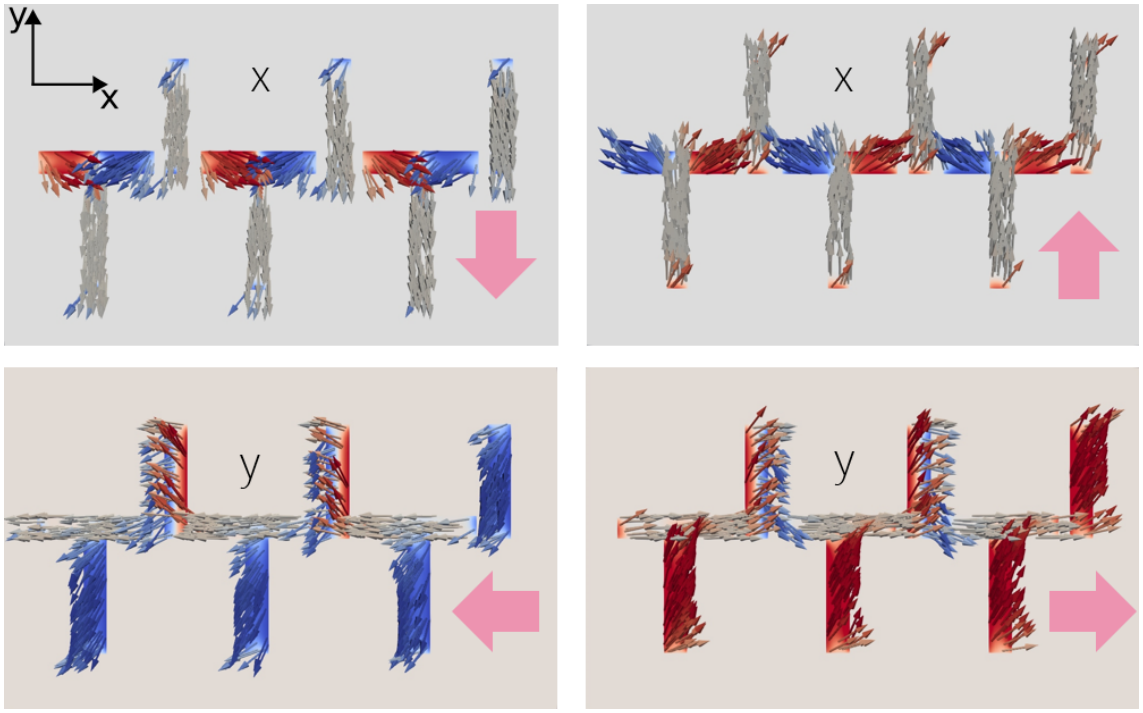

Figure 5.17: Magnetization of the guiding structure for different directions of the external in-plane driving field (big red arrow). The small arrows depict the magnetization direction and the colours visualize the x- or y-component of the magnetization as written with red being positive and blue being negative. The coordinate system is depicted in the upper left corner to clarify the x- and y-direction.

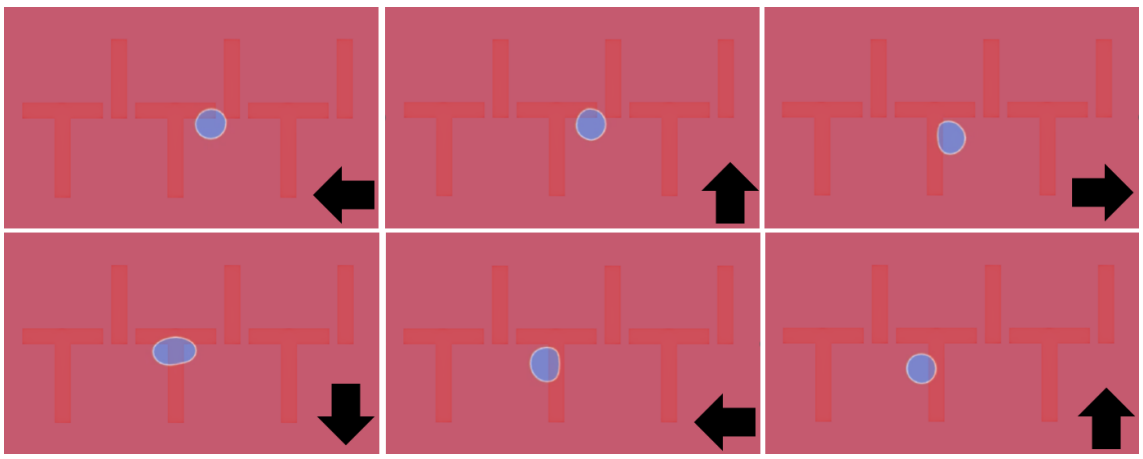

Figure 5.18: Motion of a magnetic bubble for the exertion of a clockwise rotating driving field. The guiding structure is illustrated transparently above the bubble garnet for visual reasons. (The simulation movie can be retrieved on https://ucloud.univie.ac.at/index.php/s/2CQ21jZ9d3lsS16/download?path=%2Fmovie_files&files=bubble_motion.mp4. The according simulation folder is located on GTO3 with the following directory: /home/gasser/data/master_thesis/bubble_sensor.)

Chapter 6

Conclusion

One aim of this thesis is to give a brief overview of some magnetic field sensing concepts exploiting the recently observed SOT-effect. This torque effect in thin layer structures mainly based on the SHE has an enormous potential in magnetic field sensing enabling reliable detection with small power consumption. Thus, such sensor concepts might be able to support or even replace today's typical Hall sensors in many fields of application, as for example in the automotive security sector.

First, simple out-of-plane and in-plane sensor elements are examined. These round or elliptical elements exploit the SOT-effect in the easiest way possible, where the read-out is done with some sort of magnetoresistance. Especially the out-of-plane sensor concept works well, however encountering some troubles concerning linear range. Some methods of improving the linear range and therefore the potential operation margin of the sensor are investigated. The in-plane device exhibits a severe offset for disturbing magnetic fields as elaborated above, if only one element is used. By combining two elements, the offset can be cancelled. Combining in-plane elements in a Wheatstone bridge gives an interesting sensor concept proposed in the paper (Xu et al., 2018). Some approaches to use this concept also for higher fields of a few mT are investigated, but it turns out, that the Wheatstone SMR-sensor concept only works well for tiny magnetic fields in the range of a few μT, which is also the used range in the paper. For such fields, the concepts seems surprisingly promising, however setting severe requirements for shielding methods against disturbing magnetic fields.

Moreover, the SOT-effect can be used in a Hall cross setup. The Hall cross splits up into a multidomain state and the magnetization configuration of the current-carrying arm is depending on the magnetic field along the current direction. This enables a two-dimensional magnetic field sensor, if both arms are used consecutively for field sensing. For proper current densities, the device works very reliable with the limitation, that the linear range is small. Other approaches have to be investigated to increase the range for field sensing.

Another aim of this thesis is to examine some nonvolatile multiturn sensor concepts. These should not depend on a steady power supply during rotation counting, which might enable a more robust sensing for security applications. The concept of a moving DW, which is often proposed in literature with a huge variety of realizations, seems to be very promising. The cusp sensor introduced in the paper (Mattheis et al., 2012) works

stable and reliable, as confirmed by simulations in this thesis. Moreover, a new initialization method is suggested for this sensor concept. The only drawback of the presented sensor is the need for narrow structures, making it difficult to produce it industrially on a larger scale. However, for certain special applications this sensor concept might be beneficial and maybe, by adapting the geometry, a production on a larger scale can be enabled.

The concept of moving magnetic bubbles for rotation counting is based on MBM realized in the past. The skyrmions in a garnet film move guided by a guiding structure according to a rotating magnetic field. Instead of storing data by controlling the rotating field, the rotations should be counted by determining the position of skyrmions in the system. Even though it seems obvious, that this method should work due to the already available realizations of MBM, in simulation severe problems appear concerning the motion control of the bubbles. The skyrmions do not move as expected for certain material combinations and certain setups. This is surprising, since in simulation the motion of skyrmions is not hampered by external influences in contrast to the experiment. However, by performing some adaptions the concept might probably be useful for rotation counting.

As already mentioned in the goals of this thesis, the aim is not to investigate exact properties of one specific sensor type, but rather to give an overview of some recent sensor concepts exploiting SOT and focusing on nonvolatility in the field of rotation counters. These concepts show an enormous potential towards practical realizations in magnetic field sensing. Instead of proposing certain concepts for certain fields of application, different concepts are presented and summarized, not to give specific information about them, but to encourage more investigation to learn, how they could be used in practical realizations as reliable sensors. Therefore, this thesis does not raise any claim to completeness, it rather supports further examination of recent magnetic field sensor concepts.

Bibliography

Abert, C. (2019). Micromagnetics and spintronics: Models and numerical methods. *The European Physical Journal B*, *92*(6), 120. https://doi.org/10.1140/epjb/e2019-90599-6

Abert, C., Exl, L., Bruckner, F., Drews, A., & Suess, D. (2013). magnum. fe: A micromagnetic finite-element simulation code based on FEniCS. *Journal of Magnetism and Magnetic Materials*, *345*, 29–35.

Alnaes, M. S., Blechta, J., Hake, J., Johansson, A., Kehlet, B., Logg, A., Richardson, C., Ring, J., Rognes, M. E., & Wells, G. N. (2015). The FEniCS Project Version 1.5. *Archive of Numerical Software*, *3*. https://doi.org/10.11588/ans.2015.100.20553

Baibich, M. N., Broto, J. M., Fert, A., Van Dau, F. N., Petroff, F., Etienne, P., Creuzet, G., Friederich, A., & Chazelas, J. (1988). Giant magnetoresistance of (001) Fe/(001) Cr magnetic superlattices. *Physical review letters*, *61*(21), 2472.

Borie, B., Voto, M., Lopez-Diaz, L., Grimm, H., Diegel, M., Kläui, M., & Mattheis, R. (2017). Reliable Propagation of Magnetic Domain Walls in Cross Structures for Advanced Multiturn Sensors. *Physical Review Applied*, *8*(4), 044004. https://doi.org/10.1103/PhysRevApplied.8.044004

Borie, B., Wahrhusen, J., Grimm, H., & Kläui, M. (2017). Geometrically enhanced closed-loop multi-turn sensor devices that enable reliable magnetic domain wall motion. *Applied Physics Letters*, *111*(24), 242402.

Bruckner, F., Koraltan, S., Abert, C., & Suess, D. (2023). magnum. np–A PyTorch based GPU enhanced Finite Difference Micromagnetic Simulation Framework for High Level Development and Inverse Design. *arXiv preprint arXiv:2302.08843*.

Bullock, D., Carlo, J., Mueller, D., & Brewer, T. (1975). Material and submicron bubble device properties of (LuSm) 3Fe5O12. *AIP Conference Proceedings*, *24*(1), 647–648.

Chen, Y.-T., Takahashi, S., Nakayama, H., Althammer, M., Goennenwein, S. T., Saitoh, E., & Bauer, G. E. (2013). Theory of spin Hall magnetoresistance. *Physical Review B*, *87*(14), 144411.

Chen, Y.-T., Takahashi, S., Nakayama, H., Althammer, M., Goennenwein, S. T., Saitoh, E., & Bauer, G. E. (2016). Theory of spin Hall magnetoresistance (SMR) and related phenomena. *Journal of Physics: Condensed Matter*, *28*(10), 103004.

Cho, S., Baek, S.-h. C., Lee, K.-D., Jo, Y., & Park, B.-G. (2015). Large spin Hall magnetoresistance and its correlation to the spin-orbit torque in W/CoFeB/MgO structures. *Scientific reports*, *5*(1), 1–9.

Diegel, M., Glathe, S., Mattheis, R., Scherzinger, M., & Halder, E. (2009). A new four bit magnetic domain wall based multiturn counter. *IEEE Transactions on Magnetics*, *45*(10), 3792–3795.

Dutta, S., Bose, A., Tulapurkar, A., Buhrman, R., & Ralph, D. (2021). Interfacial and bulk spin Hall contributions to fieldlike spin-orbit torque generated by iridium. *Physical Review B*, *103*(18), 184416.

Geng, L. D., & Jin, Y. M. (2012). Generation and storage of 360° domain walls in planar magnetic nanowires. *Journal of Applied Physics*, *112*(8), 083903. https://doi.org/10.1063/1.4759056

Gilbert, T. L. (2004). A phenomenological theory of damping in ferromagnetic materials. *IEEE transactions on magnetics*, *40*(6), 3443–3449.

Gowland, A. (1977). *Magnetic Bubble Memories* (Doctoral dissertation). The University of Manchester (United Kingdom).

Ham, D. A., Kelly, P. H. J., Mitchell, L., Cotter, C. J., Kirby, R. C., Sagiyama, K., Bouziani, N., Vorderwuelbecke, S., Gregory, T. J., Betteridge, J., Shapero, D. R., Nixon-Hill, R. W., Ward, C. J., Farrell, P. E., Brubeck, P. D., Marsden, I., Gibson, T. H., Homolya, M., Sun, T., et al. (2023). *Firedrake User Manual* (First edition). Imperial College London, University of Oxford, Baylor University, and University of Washington. https://doi.org/10.25561/104839

Hayashi, M., Kim, J., Yamanouchi, M., & Ohno, H. (2014). Quantitative characterization of the spin-orbit torque using harmonic Hall voltage measurements. *Physical Review B*, *89*(14), 144425.

Koraltan, S., Schmitt, C., Bruckner, F., Abert, C., Prügl, K., Kirsch, M., Gupta, R., Zeilinger, S., Salazar-Mejía, J. M., Agrawal, M., et al. (2023). Single-device offset-free magnetic field sensing with tunable sensitivity and linear range based on spin-orbit torques. *Physical Review Applied*, *20*(4), 044079.

Landau, L., & Lifshitz, E. (1992). On the theory of the dispersion of magnetic permeability in ferromagnetic bodies. *Perspectives in theoretical physics* (pp. 51–65). Elsevier.

Li, R., Zhang, S., Luo, S., Guo, Z., Xu, Y., Ouyang, J., Song, M., Zou, Q., Xi, L., Yang, X., et al. (2021). A spin–orbit torque device for sensing three-dimensional magnetic fields. *Nature Electronics*, *4*(3), 179–184.

Lim, B., Mahfoud, M., Das, P. T., Jeon, T., Jeon, C., Kim, M., Nguyen, T.-K., Tran, Q.-H., Terki, F., & Kim, C. (2022). Advances and key technologies in magnetoresistive sensors with high thermal stabilities and low field detectivities. *APL Materials*, *10*(5), 051108. https://doi.org/10.1063/5.0087311

Logg, A., Mardal, K., Wells, G. N., et al. (2012). *Automated Solution of Differential Equations by the Finite Element Method*. Springer. https://doi.org/10.1007/978-3-642-23099-8

Makarov, A. (2014). *Modeling of Emerging Resistive Switching Based Memory Cells* (Doctoral dissertation). Technische Universität Wien. Wien. Retrieved March 7, 2023, from https://www.iue.tuwien.ac.at/phd/makarov/dissertation.html#dissertationch5.html

Mattheis, R., Glathe, S., Diegel, M., & Hübner, U. (2012). Concepts and steps for the realization of a new domain wall based giant magnetoresistance nanowire device: From the available 2^{4} multiturn counter to a 2^{12} turn counter. *Journal of Applied Physics*, *111*(11), 113920. https://doi.org/10.1063/1.4728991

Nguyen, M.-H., & Pai, C.-F. (2021). Spin–orbit torque characterization in a nutshell. *APL Materials*, *9*(3), 030902. https://doi.org/10.1063/5.0041123

Nickel, J. (1995). *Magnetoresistance overview*. Hewlett-Packard Laboratories, Technical Publications Department Palo Alto.

Nielsen, J. (1979). Magnetic bubble materials. *Annual Review of Materials Science*, *9*(1), 87–121.

Paszke, A., Gross, S., Massa, F., Lerer, A., Bradbury, J., Chanan, G., Killeen, T., Lin, Z., Gimelshein, N., Antiga, L., Desmaison, A., Kopf, A., Yang, E., DeVito, Z., Raison, M., Tejani, A., Chilamkurthy, S., Steiner, B., Fang, L., Bai, J., et al. (2019). PyTorch: An Imperative Style, High-Performance Deep Learning Library. In H. Wallach, H. Larochelle, A. Beygelzimer, F. d'Alché-Buc, E. Fox, & R. Garnett (Eds.), *Advances in neural information processing systems 32* (pp. 8024–8035). Curran Associates, Inc. http://papers.neurips.cc/paper/9015-pytorch-an-imperative-style-high-performance-deep-learning-library.pdf

Ralph, D., & Stiles, M. (2008). Spin transfer torques. *Journal of Magnetism and Magnetic Materials*, *320*(7), 1190–1216. https://doi.org/10.1016/j.jmmm.2007.12.019

Salzer, J. M. (1976). Bubble Memories–Where Do We Stand? *Computer*, *9*(3), 36–41. https://ieeexplore-ieee-org.uaccess.univie.ac.at/abstract/document/1647306

Schulz, T., Lee, K., Krüger, B., Conte, R. L., Karnad, G. V., Garcia, K., Vila, L., Ocker, B., Ravelosona, D., & Kläui, M. (2017). Effective field analysis using the full angular spin-orbit torque magnetometry dependence. *Physical Review B*, *95*(22), 224409.

Suess, D., Ausserlechner, U., & Satz, A. (2021). *Device and method for detecting a magnetic field using the spin orbit torque effect* [US Patent App. 17/220,129].

Theis, G. A. (1984). *Utilization of a Bubble Memory System as a microcomputer disk resource.* (Doctoral dissertation).

Virtanen, P. et al. (2020). SciPy 1.0: Fundamental Algorithms for Scientific Computing in Python. *Nature Methods*, *17*, 261–272. https://doi.org/10.1038/s41592-019-0686-2

Xu, Y., Yang, Y., Zhang, M., Luo, Z., & Wu, Y. (2018). Ultrathin All-in-One Spin Hall Magnetic Sensor with Built-In AC Excitation Enabled by Spin Current. *Advanced Materials Technologies*, *3*(8), 1800073. https://doi.org/10.1002/admt.201800073

Yalamanchili, P., Arshad, U., Mohammed, Z., Garigipati, P., Entschev, P., Kloppenborg, B., Malcolm, J., & Melonakos, J. (2015). ArrayFire - A high performance software library for parallel computing with an easy-to-use API. https://github.com/arrayfire/arrayfire

Yuasa, S. (2008). Giant tunneling magnetoresistance in MgO-based magnetic tunnel junctions. *Journal of the Physical Society of Japan*, *77*(3), 031001.

Zhu, D., & Zhao, W. (2020). Threshold Current Density for Perpendicular Magnetization Switching Through Spin-Orbit Torque. *Physical Review Applied*, *13*(4), 044078. https://doi.org/10.1103/PhysRevApplied.13.044078

List of Figures

Appendix A

Examples of simulation scripts

Single spin simulation

```
from scipy.integrate import ode
import scipy.optimize
import numpy as np
import matplotlib.pyplot as plt
from functools import partial

class Parameters:
 gamma = 2.2128e5
 alpha = 0.01
 K1 =  -2.e4
 K12 = 1.e4
 Js = 0.5
 d = 2.5e-9
 hbar = 1.054571e-34
 e = 1.602176634e-19
 mu0 = 4*3.1415927*1e-7
 easy_axis = np.array([0,0,1])
 easy_axis2 = np.array([0,1,0])
 d = 2e-9
 currentd = 5e10
 K1 =  -0.5*Js**2/(mu0)
 linearrange = 0.000
 K12 = linearrange*Js/(2*mu0)

 p_axis = np.array([0,1,0])
 etadamp = 0.1
 etafield = 0.1

def f(t, m, p):
 prefactorpol = p.currentd*p.hbar/(2*p.e*p.Js*p.d)
 hani1=2*p.K1/p.Js*p.easy_axis*np.dot(p.easy_axis,m)
 hani2=2*p.K12/p.Js*p.easy_axis2*np.dot(p.easy_axis2,m)
 h=p.hext+hani1+hani2

 mxh = np.cross(m, h-prefactorpol*(p.etadamp*np.cross(m,p.p_axis)+p.etafield*p.
    p_axis))
 mxmxh = np.cross(m, mxh)
 rhs = -p.gamma/(1+p.alpha**2)*mxh-p.gamma*p.alpha/(1+p.alpha**2)*mxmxh
 return [rhs]

def calc_equilibrium(m0_,t0_,t1_,dt_,paramters_):
 t0 = t0_
 m0 = m0_
 dt = dt_
 r = ode(f).set_integrator('vode', method='bdf',atol=1e-14)
 r.set_initial_value(m0_, t0_).set_f_params(paramters_).set_jac_params(2.0)
 t1 = t1_
 while r.successful() and r.t < t1:
    mag=r.integrate(r.t+dt)
 return(r.t,mag)
```

```
50
51 ##################################################################
52 ######################################################################
53
54 paramters = Parameters()
55 p=paramters
56 a=0.05/(p.mu0)
57 fieldrange = np.linspace(-a, a, num=19)
58 signal  = []
59 fieldrangeT =[]
60 orgdensity = paramters.currentd
61 for i in fieldrange:
62  paramters.hext = np.array([0,0,i])
63  paramters.currentd = orgdensity
64  initm=[1,0,0]
65  initm=np.array(initm)/np.linalg.norm(initm)
66
67  t1,mag1 = calc_equilibrium(m0_ = initm,t0_=0,t1_=150e-9,dt_=1e-9,paramters_=
       paramters)
68  paramters.currentd = -paramters.currentd
69  t2,mag2 = calc_equilibrium(m0_ = initm,t0_=0,t1_=150e-9,dt_=1e-9,paramters_=
       paramters)
70  print("##################################################################")
71  print("field:",i*paramters.mu0)
72  print("mag1:",mag1[0],mag1[1],mag1[2])
73  print("mag2:",mag2[0],mag2[1],mag2[2])
74  print("signal:",mag2[0]-mag1[0])
75
76  signal.append(mag2[0]-mag1[0])
77  fieldrangeT.append(i*paramters.mu0)
78
79 plt.plot(fieldrangeT, signal, marker='o')
80 ax=plt.axes()
81 ax.set(xlabel=r'$\mu_0 H_z$ (T)',ylabel=r'$m_{x,I+} - m_{x,I-}$ ')
82 plt.savefig('signal.png')
83 plt.show()
```

Listing A.1: Single spin simulation for in-plance sensor device.

Micromagnetic simulation with *Magnum.af*

```
1 #!/usr/bin/python3
2 import arrayfire as af
3 from magnumaf import *
4 mu0 = Constants.mu0
5 args = parse()
6 filepath = args.outdir
7
8 def calcK1(Hk, Js):
9     Keff = Js*Hk/2./mu0
10    K = Keff + 0.5*mu0*(Js/mu0)**2.
11    return K
12
13 def calcAex(Js_T):
14    A0 = 20e-12#Joule/meter
15    J0 = 1.2#Tesla
16    Aex_T = A0*(Js_T/J0)**1.7
17    return Aex_T
18
19 def cross_geometry(nx : int, ny: int, nz : int, width_cross_x : float,
       width_cross_y : float, make_3d = True, region = 0):
20    thickness_x = int(width_cross_x/dx)
21    thickness_y = int(width_cross_y/dy)
22
23    cross = af.constant(0, nx, ny, nz, 1,  dtype=af.Dtype.f64)
24    x_strt = nx/2 - thickness_x/2
25    x_stop = nx/2 + thickness_x/2
26    y_strt = ny/2 - thickness_y/2
27    y_stop = ny/2 + thickness_y/2
```

```
    if region == 0:         #Hall Cross Geometry
        cross[x_strt : x_stop, :] = 1
        cross[:, y_strt:y_stop] = 1
    elif region == 1:       #Only stripe along X -> relevant for Rxx Measurements
        cross[:, y_strt:y_stop] = 1
    elif region == 2:     #Only stripe along Y -> relevant for Ryy Measurements
        cross[x_strt : x_stop, :] = 1
    elif region == 3:       #Only central region -> relevant for Ryx Measurements
        cross[x_strt : x_stop, y_strt : y_stop ] = 1
    if make_3d:
        return af.tile(cross, 1, 1, 1, 3)
    else:
        return af.tile(cross, 1, 1, 1, 1)

def get_random_m0(nx, ny, nz, mask, seed=None):
    if seed: np.random.seed(seed)
    m0 = np.random.normal(0,1,(nx,ny,nz,3))
    m0 = m0/np.linalg.norm(m0,axis=3,keepdims=True)
    m0 = af.interop.np_to_af_array(m0)
    return m0 * mask

def get_hext_arr(h_ext, h_axis):
    if h_axis == 'x':   # Field in X direction
        Hextarray = np.array([h_ext, 0, 0])
    elif h_axis == 'y': # Field in Y direction
        Hextarray = np.array([0, h_ext, 0])
    elif h_axis == 'z': # Field in Z direction
        Hextarray = np.array([0, 0, h_ext])
    return Hextarray

tlist = np.array([0.92e-9, 1.02e-9, 1.14e-9, 1.25e-9])#Units of m.
Jslist = np.array([1.15, 1.13, 1.06, 0.94, 0.76])#Mslist for T = 25, 100, 150, 200,
     250
I0list = np.array([0.1, 1.9, 2.5, 3, 3.351])*1e-3

transfer_curve = True # tranfer curve by relaxation at different external fields

tindex = 0    # Choose index for thickness, 0:= t = 0.92nm etc.
tempindex = 4
Jdir = '+x' # Choose current direction: +x, -x, +y, -y

width_cross_x = 2000e-9
width_cross_y = 2000e-9
length_cross_x = 10000e-9
length_cross_y = 10000e-9
thickness_Ta = 6.e-9

x, y, z = np.max([length_cross_x, width_cross_y]), np.max([length_cross_y,
    width_cross_x]), tlist[tindex]
dx,dy,dz = 5e-9, 5e-9, z
nx, ny, nz = int(2000), int(2000), int(1)

Acrosssection = width_cross_x if 'x' in Jdir else width_cross_y
Acrosssection *= (tlist[tindex] + thickness_Ta)
Jlist = I0list/Acrosssection

Hksystem = 20e-3
tsystem = tlist[tindex]
Tsystem = Tlist[tempindex]
Jssystem = Jslist[tempindex]
Jesystem = Jlist[tempindex]
K1system = calcK1(Hksystem, Jssystem)
Aexsystem = calcAex(Jssystem)

cross3d = cross_geometry(nx, ny, nz, width_cross_x, width_cross_y)
cross1d = cross_geometry(nx, ny, nz, width_cross_x, width_cross_y, make_3d = False)
crossrxx = cross_geometry(nx, ny, nz, width_cross_x, width_cross_y, make_3d = False
    , region = 1)
crossryy = cross_geometry(nx, ny, nz, width_cross_x, width_cross_y, make_3d = False
    , region = 2)
crossrxy = cross_geometry(nx, ny, nz, width_cross_x, width_cross_y, make_3d = False
    , region = 3)
crossrxx3d = cross_geometry(nx, ny, nz, width_cross_x, width_cross_y, make_3d =
```

```
    True, region = 1)
crossryy3d = cross_geometry(nx, ny, nz, width_cross_x, width_cross_y, make_3d =
    True, region = 2)
crossrxy3d = cross_geometry(nx, ny, nz, width_cross_x, width_cross_y, make_3d =
    True, region = 3)

testing = False
if testing:
    Util.write_vti(cross3d, dx, dy, dz, filepath + "Region_Hallcross")
    Util.write_vti(crossrxx, dx, dy, dz, filepath + "Region_rxx")
    Util.write_vti(crossryy, dx, dy, dz, filepath + "Region_ryy")
    Util.write_vti(crossrxy, dx, dy, dz, filepath + "Region_rxy")
    exit()

eta_damp = -0.1451
eta_field = -0.0276
if Jdir == '+x':
    #this results in a polarization p = [0, -1, 0]
    parray = crossrxx3d * Magnetization.homogeneous(nx, ny, nz, [0., -1., 0.])
elif Jdir == '-x':
    #this results in a polarization p = [0, +1, 0]
    parray = crossrxx3d * Magnetization.homogeneous(nx, ny, nz, [0., 1., 0.])
elif Jdir == '+y':
    #this results in a polarization p = [-1, 1, 0]
    parray = crossryy3d * Magnetization.homogeneous(nx, ny, nz, [-1., 0., 0.])
elif Jdir == '-y':
    #this results in a polarization p = [+1, 0, 0]
    parray = crossryy3d * Magnetization.homogeneous(nx, ny, nz, [1., 0., 0.])

Ms_array = cross1d * Jssystem / Constants.mu0
A_array = cross1d * Aexsystem
K_array = cross1d * K1system
Kaxis_array = cross3d * Magnetization.homogeneous(nx, ny, nz, [0, 0, 1])

random = True
homogenous = False
m0list = [0., 0., 1.]
artificial_DW = False
mrandomseed = 101
if random:
    m0 = get_random_m0(nx, ny, nz, cross3d, seed=mrandomseed)
    Util.write_vti(m0, dx, dy, dz, filepath + "m0_seed_%d"%mrandomseed)
elif homogenous:
    m0 = cross3d * Magnetization.homogeneous(nx, ny, nz, m0list)
elif artificial_DW: # this is only for Keff > 0.0
    m0 = cross3d * Magnetization.homogeneous(nx, ny, nz, m0list)
    m0[:, :ny/2, :, 2] += -1.0
    m0[:, ny/2:, :, 2] += 1.0

mesh  = Mesh(nx, ny, nz, dx, dy, dz)
state = State(mesh, Ms = Ms_array, m = m0)

exchange = ExchangeField(A_array, mesh)
demag = DemagField(mesh, verbose = True, caching = False, nthreads = 32)
aniso = UniaxialAnisotropyField(K_array, Kaxis_array)
sot = SpinTransferTorqueField(parray, eta_damp, eta_field, Jesystem, z)

llgterms = [exchange, demag, aniso, sot]
llg = LLGIntegrator(alpha = 1.0, terms = llgterms)

def relax_m(relax_time):
    cnt = 0
    stream = open(filepath +"m_relax.dat", "w")
    stream.write("#t(s), mx,my,mz, mx_rxx, my_rxx, mz_rxx, mx_rxy, my_rxy, mz_rxy,
    mx_ryy, my_ryy, mz_ryy\n")
    state.t = 0.0
    while state.t <= relax_time:
        mx,my,mz = Util.spacial_mean_in_region(state.m, cross1d)
        mx_rxx, my_rxx, mz_rxx = Util.spacial_mean_in_region(state.m, crossrxx)
        mx_rxy, my_rxy, mz_rxy = Util.spacial_mean_in_region(state.m, crossrxy)
        mx_ryy, my_ryy, mz_ryy = Util.spacial_mean_in_region(state.m, crossryy)
        stream.write("%g %g %g %g %g %g %g %g %g %g %g %g %g\n"%(state.t,
            mx,my,mz,
```

```
            mx_rxx, my_rxx, mz_rxx,
            mx_rxy, my_rxy, mz_rxy,
            mx_ryy, my_ryy, mz_ryy,
        ))
        print("%g %g %g %g"%(state.t,mx,my,mz))
        if int(cnt%1000) == int(0):
            state.write_vti(filepath + "m_relax_%d"%llg.accumulated_steps)
        llg.step(state)
        cnt += 1
    stream.close()

if transfer_curve:
    Bmax = 10e-3 # Maximal Field Value in Tesla
    B_step = 0.5e-3 #
    b_list = np.arange(-Bmax, Bmax+B_step, B_step)
    theta = np.deg2rad(0.)
    Hextdir = np.array([1., 0., 0.])
    #Hextdir = np.array([0., 1., 0.])
    #Hextdir = np.array([0., 0., 1.])

    relax_time = 5e-9
    m0 = get_random_m0(nx, ny, nz, cross3d)
    state = State(mesh, Ms = Ms_array, m = m0)
    def relax_trans(i, h, je_var, hbias, relax_time, cont = True):
        Hbias = af.constant(hbias, nx, ny, nz, 3, dtype=af.Dtype.f64)
        zeebias = ExternalField(Hbias)

        if cont:
            if i == 0:
                relax_time = 10e-9
                state.m = m0
            else:
                state.read_vti(filepath + "m_%.5d.vti"%(i - 1))
        else:
                state.m = m0

        zeeswitch = af.constant(0.0, nx, ny, nz, 3, dtype=af.Dtype.f64)
        zee = ExternalField(zeeswitch)
        Hextarray = h * Hextdir
        zee.set_homogeneous_field(Hextarray[0], Hextarray[1], Hextarray[2])

        sot = SpinTransferTorqueField(parray, eta_damp, eta_field, je_var, z)
        llgterms = [exchange, demag, aniso, sot, zeebias, zee]
        llg = LLGIntegrator(alpha = 1., terms = llgterms)

        filename = filepath + "log_%.5d.dat"%(i)
        state.t = 0.0
        with open(filename, 'w') as stream:
            while state.t <= relax_time+1e-12:
                mx, my, mz = Util.spacial_mean_in_region(state.m, cross1d)
                mx_rxx, my_rxx, mz_rxx = Util.spacial_mean_in_region(state.m,
    crossrxx)
                mx_rxy, my_rxy, mz_rxy = Util.spacial_mean_in_region(state.m,
    crossrxy)
                mx_ryy, my_ryy, mz_ryy = Util.spacial_mean_in_region(state.m,
    crossryy)
                stream.write("%g %g %g %g %g %g %g %g %g %g %g %g %g %g %g %g %g\n"
                    %(state.t, Hextarray[0], Hextarray[1], Hextarray[2],
                        mx, my, mz,
                        mx_rxx, my_rxx, mz_rxx,
                        mx_rxy, my_rxy, mz_rxy,
                        mx_ryy, my_ryy, mz_ryy,
                        ))
                print("%g %g %g %g"%(state.t,mx,my,mz))
                llg.step(state)
            state.write_vti(filepath + "m_%.5d"%(i))
    for i in range(0, len(b_list)):
        b = b_list[i]
        relax_trans(i, b/Constants.mu0, Jesystem, hbias = 0e-3 / mu0, relax_time =
    5e-9, cont = False)
```

Listing A.2: Micromagnetic simulation of Hall cross sensor with *Magnum.af* (Field sweep for one current direction and density).

Micromagnetic simulation with *Magnum.np*

```
from magnumnp import *
import torch

Timer.enable()

outpath="output_pos_je/"

# initialize mesh
eps = 1e-15
n  = (500, 300, 1)
dx = (0.5e-9, 0.5e-9, 1e-9)
mesh = Mesh(n, dx, origin = (-n[0]*dx[0]/2., -n[1]*dx[1]/2., 0.0))

state = State(mesh)
x, y, z = state.SpatialCoordinate()
a = n[1]*dx[1]/2.
b = (n[0]*dx[0] - n[1]*dx[1])/2.
magnetic = ( (((x-b)**2. + (y)**2. <= (a)**2.) | ((x+b)**2. + (y)**2. <= (a)**2.))
    | ( x**2 <= b**2.) )
write_vti(magnetic, outpath+"magnetic.vti")

# initialize polarization, p, and charge current amplitude
# thickness of thin film on which the SOT acts
p = state.Constant([0, -1, 0])
p[~magnetic] = 0.
je = 2.4e11
d = n[2] * dx[2]

#write Polarization to file
write_vti(p, outpath+"Polarization.vti", state)

#define space dependent material parameters
Ms = state.Constant([0.])
Ms[magnetic] = 0.75 / constants.mu_0

#define space dependent material parameters
K = state.Constant([0.])
K[magnetic] = 0.24e6

#define space dependent material parameters
A = state.Constant([0.])
A[magnetic] = 9e-12

# initialize material parameters
state._material = {
        "Ms": Ms,
        "A": A,
        "Ku": K,
        "Ku_axis": state.Tensor([0,0,1]),
        "alpha": 1.0,
        "eta_damp": -0.09,
        "eta_field": 0.17,
        "p": p,
        "d": d,
        "je": je
        }

state.m = state.Constant([0, 0, 1])
state.m[~magnetic] = 0.

# initialize field terms
demag = DemagField()
exchange = ExchangeField()
aniso = UniaxialAnisotropyField()
torque = SpinOrbitTorque()

#define external field
Hmax = 20e-3 / constants.mu_0
t_final = 200e-9
zeeman = ExternalField(lambda t: state.Tensor([(Hmax*t/t_final)-(Hmax*0.5), 0, 0]))
```

```

state._material["alpha"] = 0.1
Timer.enable()
llg = LLGSolver([demag, aniso, exchange, torque, zeeman])
logger = Logger(outpath, ['t', 'm'], ['m'])

while state.t < t_final:
    llg.step(state, 1e-10)
    logger << state

Timer.print_report()
```

Listing A.3: Micromagnetic simulation of elliptical out-of-plane SOT-device with *Magnum.np* for a current density of $j_e = 2.4 \cdot 10^{11}$ A/m^2 and one current direction.

Micromagnetic simulation with *Magnum.pi*

```
from magnumpi import *

mesh = Mesh("mesh/sample.msh")

state = State(mesh,
    cell_domains = {
        "other": 2,
        "down": (1,4),
        "up": (3,5),
        "right": (10,12),
        "left": 11,
        "magnetic": (1,2,3,4,5,10,11,12)
    },
    scale = 1e-9
)

state.material["magnetic"] = Material(
    alpha      = 0.01,
    Ms         = 8e5,
    A          = 1.3e-11,
    Ku         = 0.0,
    Ku_axis    = (0, 0, 1),
)

state.m = Constant((0, 0, 0,))
state.m["down"] = Constant((0, -1, 0))
state.m["up"] = Constant((0, 1, 0))
state.m["left"] = Constant((-1, 0, 0))
state.m["right"] = Constant((1, 0, 0))
state.m["other"] = Constant((1, 1, 0))
state.m.normalize()

# setup effective field
demag      = DemagField()
exchange   = ExchangeField()
aniso      = UniaxialAnisotropyField()

t_final = 200e-9
omega = 2*pi*1/t_final*2.
external = ExternalField(lambda t: Constant((25e-3/constants.mu_0 * cos(omega*(t-0e
    -8)-0.5236), 25e-3/constants.mu_0 * sin(omega*(t-0e-8)-0.5236), 0.)))
state.hext = external.h

state.h = exchange + aniso + demag + external
llg = LLGSolver()
logger = ScalarLogger("log_rot.dat", ['t', 'hext', 'm'])
mlogger = FieldLogger("m_rot/m.pvd", "m", every = 10)

while state.t < t_final:
    logger << state
    mlogger << state
```

```
51     llg.step(state, 1e-10)
```

Listing A.4: Micromagnetic simulation of 4 cusps as obstacles for domain walls with *Magnum.pi* (Simulation script for the procedure presented in the Figures 5.10 and 5.11).

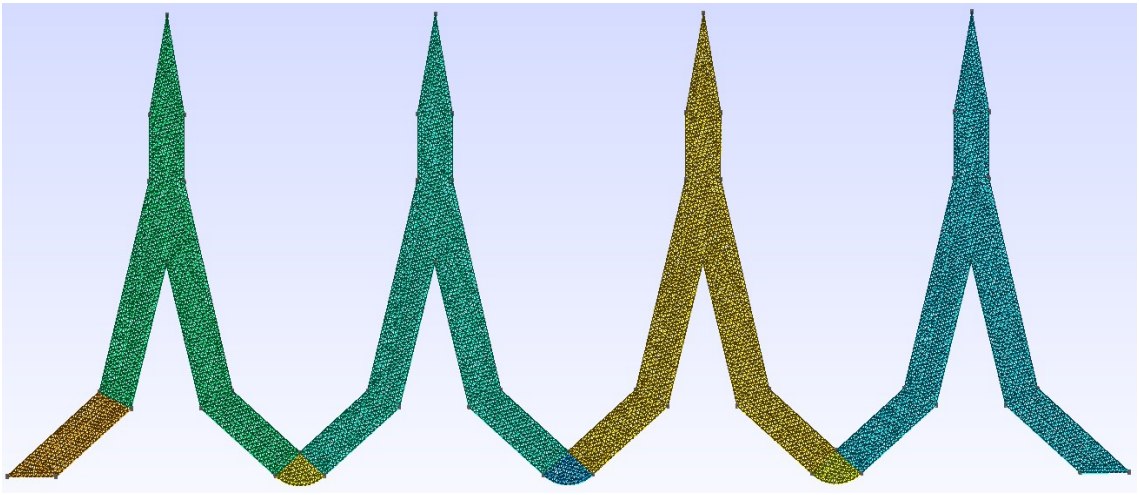

Figure A.1: Mesh of 4 cusps as obstacles used for the *Magnum.pi* simulation in Listing A.4. The different regions for the magnetic initialization are marked with different colours.

Appendix B

Domain Wall propagation after initialization

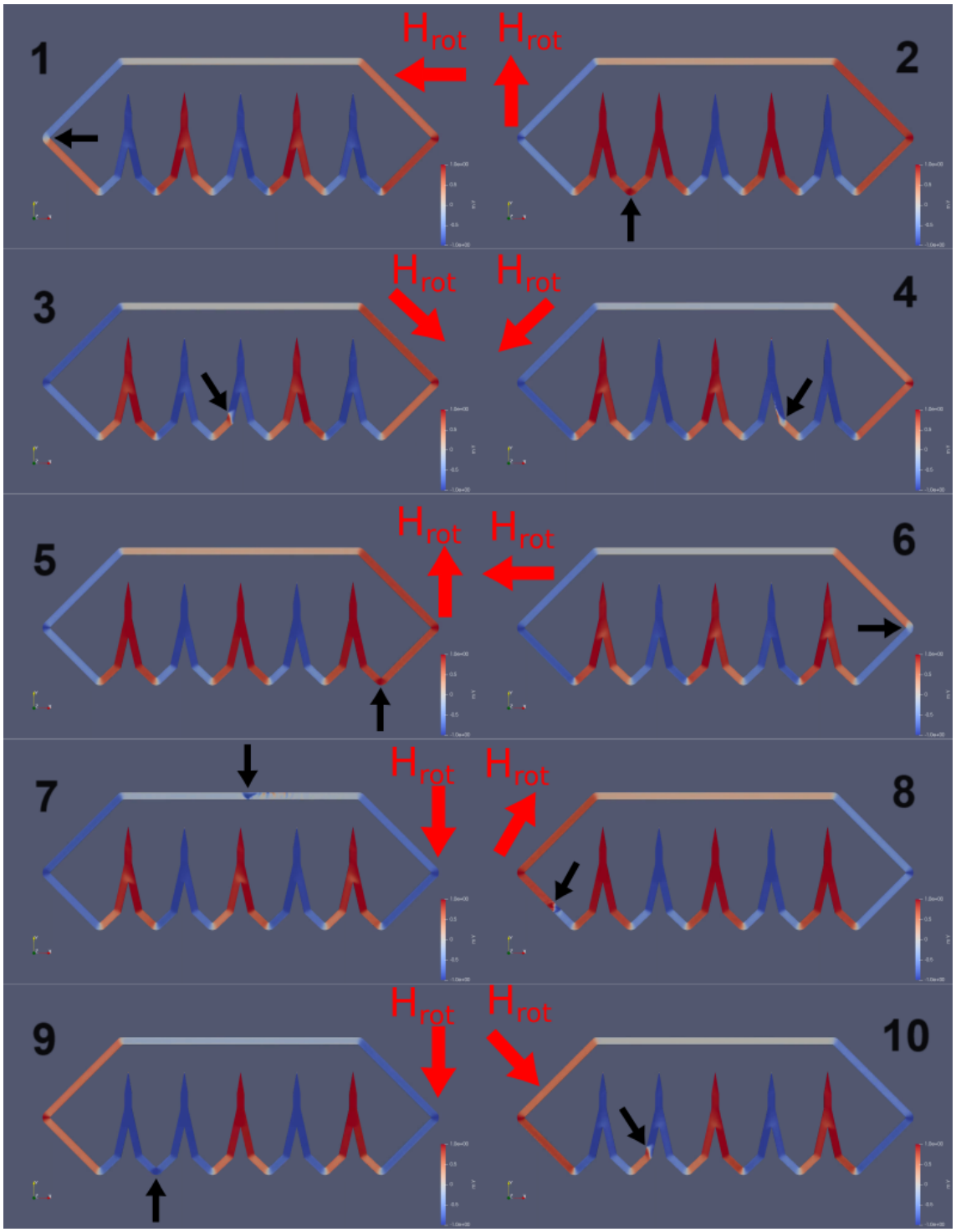

Figure B.1: DW propagation for several rotations in the cusp loop after the initializing steps proposed in the thesis. The subfigures ordered by numbers depict some consecutive field directions. The DW moves in the loop in a controlled and stable way. The red arrow indicates the current direction of the counterclockwise rotating magnetic field and the black arrow shows the corresponding position of the DW. The colour indicates the y-component of the magnetization. (The simulation movie, which shows the displayed DW propagation after the initializing steps, can be retrieved on https://ucloud.univie.ac.at/index.php/s/2CQ21jZ9d3lsS16/download?path=%2Fmovie_files&files=cusp_loop.mp4. The according simulation folder is located on GTO3 with the following directory: /home/gasser/data/master_thesis/cusp_sensor/loop.)